Politecnico di Torino

INGEGNERIA ENERGETICA E NUCLEARE

A.a. 2023/2024

Sessione di Laurea Ottobre 2024

Metodi di experimental design nel settore delle batterie

Relatori:

Prof. Federico Bella

Dott. Diego Pugliese

Candidato:

Staffieri Roberto

Summary

Chapter 1: Introduction

Problem Statement

The performance of lithium-ion batteries (LIBs) depends on their energy storage, power output, capacity, longevity, and charging speed, which are influenced by both chemical and physical properties like current flow, ion efficiency, resistance, and electrode characteristics. These properties are determined by the interaction of battery components (anode, cathode, binder, separator, and electrolyte) during manufacturing. Traditionally, understanding this relationship has involved trial-and-error or changing one variable at a time approaches. Combining experiments with modelling has proven effective, but it can be time-consuming. To streamline this process, statistical DoE is a useful method for gathering relevant data economically and efficiently. It is a statistical approach that focuses on carefully planning, gathering, and analyzing experimental data to ensure that engineering conclusions are valid and unbiased. It revolves around understanding how certain factors (independent variables) affect specific outcomes (dependent variables). In ***Figure 1*** a scheme of the methodology is represented.

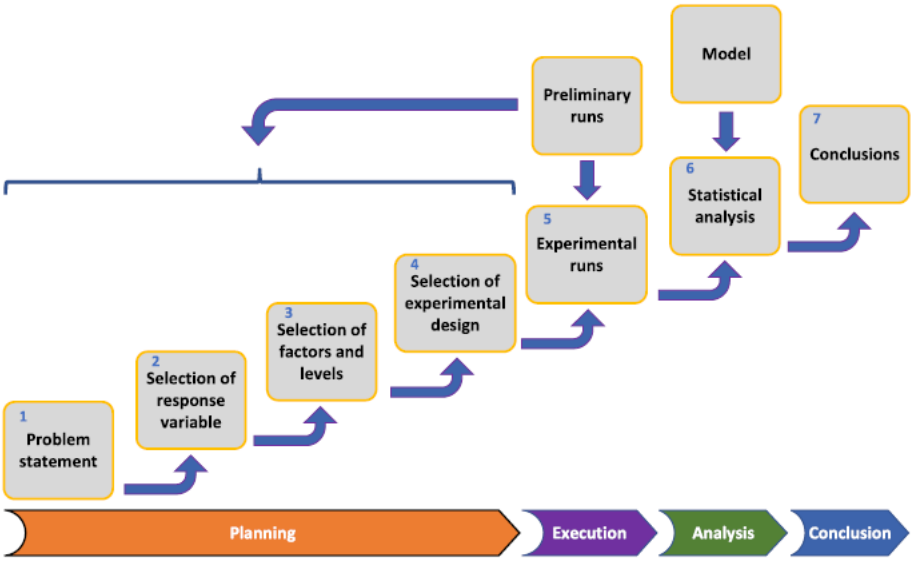

Figure 1 *DoE methodology. The process typically involves: i) Problem definition and goal setting: the problem and objectives of the experiment are clearly defined, and the relevant responses, factors, and their appropriate settings based on these objectives are chosen; ii) Experimental design selection: an appropriate experimental setup, which includes the number of factors, levels, repetitions, blocks, randomization, and the creation of a practical model, is selected; iii) Conducting experiments: experiments are carried out according to the chosen design. In some cases, especially in preliminary stages or screening, conducting a few initial experiments may help to determine suitable factor ranges; iv) Data analysis: statistical methods such as Analysis of Variance (ANOVA) and graphical tools to process the collected data are utilized; v) Objective conclusions: the results of the statistical analysis provide the basis for forming objective conclusions. Adapted and reprinted with permission from [1].*

Common factorial designs include the 2k and the 3k. The former is often used for screening, while the latter is preferred when there is a suspicion of a quadratic relationship between factors and responses. Response Surface Methodology (RSM) involves graphically representing the relationship between factors and responses, typically seen as 3D plots and contour plots for two variables. Noise factors, which can't be controlled in the actual process but can be simulated in experiments, are considered in Taguchi designs. The Signal-to-Noise ratio (S/N) quantifies the variability of the response in relation to the target value due to these noise factors. Three common S/N relationships can be specified based on the goals of the experiment: nominal-the-best, larger-the-better, and smaller-the-better. In the simplex centroid design, experimental

points are positioned at centroid points, vertices, and the overall centroid, with the total number of points determined by the number of factors (q). An example is reported in ***Figure 2***.

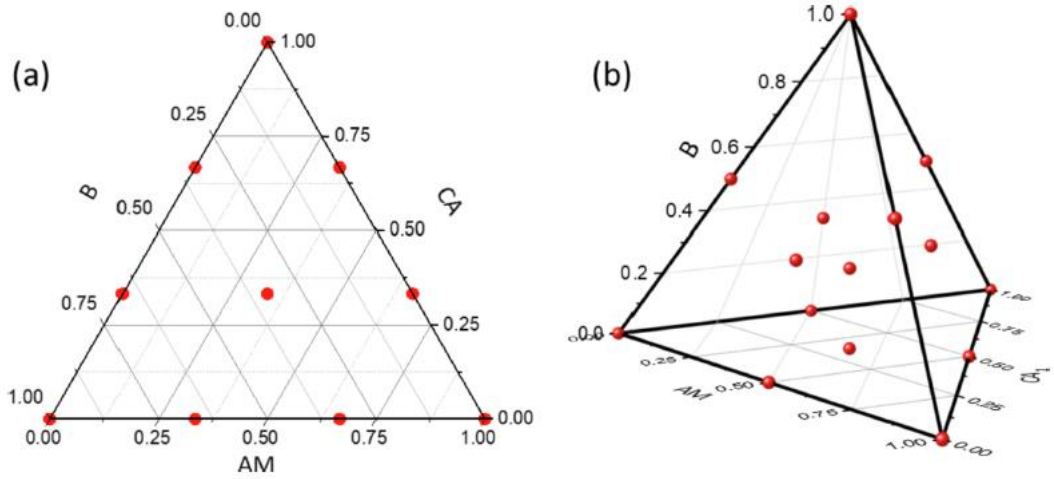

Figure 2 *Examples of mixture designs: (a) simplex lattice with 10 points, (b) simplex centroid q = 4 with 15 points. Adapted and reprinted with permission from [1].*

Optimal designs come into play when dealing with unique models, limited experiments, or restricted experimental conditions. In most DoE studies, typically, up to a second-order model is considered. To evaluate this model, the first step involves examining residual plots, such as residual vs. predictions, residual histogram, and normal probability plot of residuals. Additionally, numerical assessments for model testing mainly revolve around the use of ANOVA, which is an analysis that dissects the overall variability in the response. The ANOVA process begins with the calculation of the regression sum of squares (SSR) and the residual sum of squares (SSE), both of which contribute to the total sum of squares (SST). Subsequently, the mean squares for regression (MSR) and residuals (MSE) are computed, and these values are used to determine the F-value. In the study of battery aging, temperature (T) and state of charge (SoC) are commonly recognized as the primary factors affecting capacity decline. A critical performance indicator for lithium-ion batteries (LIBs) is their energy capacity. Electrode composition involves a mix of key components, including anode materials (AM), cathode materials (CA), and binders. The proportions of these components directly impact energy and power density and vary based on the intended application. Typical anode materials consist of carbon varieties like graphite, synthetic graphite, and hard carbon. Cathodes are often metal oxides, while conductive additives include carbon black, carbon nanofibers, and conductive graphite. Polymer binders like polyvinylidene difluoride (PVDF) for cathodes and carboxymethyl cellulose for anodes provide mechanical integrity. The electrolyte comprises an organic salt in a solution of at least two carbonate solvents. DoE proves valuable for quickly determining critical parameters and optimal conditions for synthesizing electrode materials. Battery quality and performance are not only reliant on electrode components but also on manufacturing processes at the electrode and cell levels. DoE plays a pivotal role in battery design, examining design parameters like materials, dimensions, coolant flow rates, and additional features to ensure even temperature distribution, minimize temperature rise, and enhance energy release. One exciting application of DoE in LIBs involves identifying the best charging patterns or settings for faster charging, increased capacity, or extended cycle life. Two alternative charging methods, pulse charging (PS) and multi-stage constant current (MS-CC), have been explored. PS employs intermittent voltage or current to reduce dendrite formation, leading to shorter charging times and larger currents. Key pulse charging parameters include frequency, peak charge current, and duty cycle. In MS-CC, the total charging time is divided into stages with predefined currents, advancing to a new stage when a specific voltage is reached. DoE helps determining optimal settings for these charging methods, reducing reliance on battery models and time-consuming tests. Orthogonal Arrays (OAs), particularly in the Taguchi method, are often employed

in such studies. Optimal pulse charging parameters are better obtained through RSM instead of OAs, as RSM allows for the exploration of two-way interactions and second-order terms. DoE also plays a significant role in process optimization, particularly when dealing with two or three critical factors identified in screening designs. When the relationship between factors and responses follows a second-order or higher polynomial, stationary points of the equation can be found, representing maximum, minimum, or saddle points. The contour plots for such response surfaces reveal concentric ellipses or circles for maxima and minima and hyperbolas for saddle points. Rising or falling ridges on the response surface suggest that the optimum lies beyond the explored experimental region, necessitating adjustments to the factor ranges. In the efficient management of LIBs, accurate models are essential to describe their behavior under varying conditions and chemistries. These models fall into three main categories: empirical models, electrochemical models (EMs), and equivalent circuit models (ECMs). Evidence of the advantages of using DoE in the field of LIBs can be found analyzing experimental data from Hamed et al., focusing on LiNi1/3Mn1/3Co1/3O2 (NMC) electrodes. Their research aimed to understand how the rate capability of these electrodes relates to their microstructure using a series of experiments and a mathematical model (P2D). They investigated three factors: dry thickness, NMC loading, and binder/carbon weight ratio, each with varying levels. The parameters they examined included tortuosity (τ), rate capability coefficient (γ), and fractional long-range energy loss (ω). In total, they conducted 36 experiments to cover all possible combinations of factors and levels. They employed a RSM I-optimal design to create a predictive model with statistically significant terms and visually represent how factors affect the responses. While a minimum of 10 experiments was needed to fit a quadratic model for this set of factors, they carried out 15 experiments to ensure a robust model. The I-optimal design they used reduced the experimental workload by more than 50%, showcasing the efficiency of the DoE approach. This methodology is valuable in investigating degradation at the pack level, where multiple batteries are connected in series and parallel, resembling real-world battery applications. The examples provided highlight promising areas for future research, where the full potential of DoE in LIB research has yet to be fully explored and quantified.

Chapter 2: Literature review

Section 2.1: DoE for Recycling and Recovery of battery materials

A corona-electrostatic technology for zinc and brass recovery from the coarse fraction of the recycling process of spent alkaline and zinc–carbon batteries

Among the efforts to reduce waste, prevent environmental degradation and provide beneficial secondary raw materials, it is worthwhile mentioning the recycling of used alkaline and zinc-carbon batteries. These batteries are no longer classified as hazardous waste, but the recycling of spent batteries is mandatory (in accordance with the European Union Directives, 2006/66/EC). The objective is the recovering of brass and Zn granules from the coarse fraction acquired during the recycling process. One of the techniques is based on corona-electrostatic separation. An extended needle-type corona electrode was fitted by Laur Calin *et al.* on the top of a free-fall electrostatic separator (***Figure 3***Errore. L'origine riferimento non è stata trovata.) in order to strongly charge by ion bombardment all the components of the granular mixture introduced by an inclined plane feeder [2, 3]. The density difference between metallic granules (zinc and brass) and other non-metallic components caused distinct trajectories and allowed them to be collected as segregated fractions.

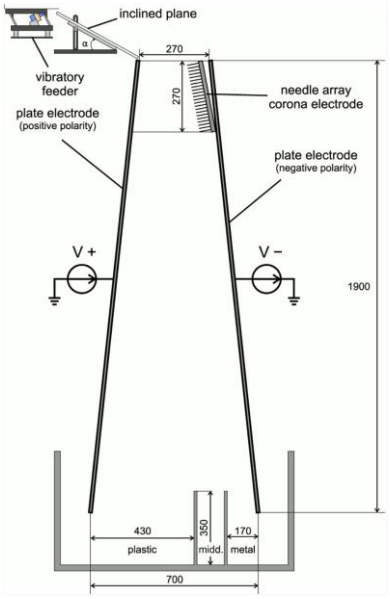

Figure 3 *Free fall corona-electrostatic separator equipped with an extended needle array corona electrode. Adapted and reprinted with permission from [2].*

The coarse fraction is the mixture of materials that feeds the separator. It is constituted by Zn, brass, graphite, plastic and paper materials and non-woven fabrics and it is realized with a pre-treatment process divided into three steps: i) sorting of the spent batteries' mixture (to divide alkaline and Zn-C batteries from other typologies like Ni-Cd and Ni-MH); ii) shredding of the selected mixture; iii) sieving. An inclined plane was used to bring the granular mixture into the separator, where it was then allowed to fall freely. All the granules became negative in the corona discharge zone after being exposed to a powerful ion bombardment. The granules were subjected to different forces when they entered the separator zone: the gravity force FG, the electrical force FE and the air drag force FA with the following formulas: $F_G = mg$, $F_E = QE$ and $F_A = \frac{1}{2} C_D \rho_A S v^2$, where m is the mass of the granule, g the acceleration due to gravity, Q the electric charge that the granule acquired after being bombarded by ions, E the strength of the electric field, CD the drag coefficient, ρ_A the air density, S the projected surface of the particle on motion direction, v the particle velocity. The charge that granules - especially plastic granules - accumulates in the corona discharge

zone significantly affects both their trajectories and the outcomes of the separation process. Gravity force has a stronger influence on metallic granules than on the plastic ones. The main parameters that influence the separation process are the angle (α) of the inclined plane and the voltage (V) of the electrodes. In this case, DoE was used implementing a polynomial model to describe the phenomenon that illustrates the relationship between the response output function, y, and its input variables, ui, that are the response and the factors, respectively, as shown in the equation:

$$y = f(x_i) = a_0 + \sum a_i x_i + \sum a_{i,j} x_i x_j + \sum a_{i,i} x_i^2$$

where a_i are the coefficients of a quadratic polynomial model and x_i is the normalized centered value for each factor u_i, defined as:

$$x_i = \frac{(u_i - u_{i0})}{\Delta u_i} = u_i^*$$

with

$$u_{i0} = \frac{u_{i\max} + u_{i\min}}{2}; \Delta u_i = \frac{u_{i\max} - u_{i\min}}{2}$$

With the support of the software MODDE (Umetrics, Sweden), it was possible to determine two statistical measures, *i.e.*, "goodness of fit" (R2) and "goodness of prediction" (Q2). In this way, it was possible to forecast what happens under novel experimental circumstances. A decent mathematical model possesses R2 and Q2 values that are close to unity and, ideally, are separated by no more than 0.2-0.3. A full factorial design (3 levels) was adopted with a total of 12 experiments (1 for each point of the matrix and 3 repetitions in the central point). The factors were the voltage *V* with V_{min} = 80 kV, V_{max} = 88 kV and the angle *α* with α_{min} = 27° and α_{max} = 31°. The responses were the recovery rate and purity. The quadratic model was defined as follows:

$$y(\%) = a_0 + a_1 V^* + a_2 \alpha^* + a_{12} V^* \alpha^* * + a_{11} V^{*2} + a_{22} \alpha^{*2}$$

The experiments were carried out using 800 g of coarse fraction for each of them and a constant feed rate of 130 g/min. The results (***Table 1***) were processed by the software to determine the values of the coefficients of the polynomial model excluding those whose uncertainties were greater than their value.

Table 1 *Results of 12 separation runs on the free-fall corona-electrostatic separator as part of a DoE quadratic model with the voltage V and input angle α as factors and metal purity, metal recovery rate and plastic recovery rate as responses. Adapted and reprinted with permission from [2].*

Run order	*V* (kV)	*α* (°)	Metal recovery rate (%)	Metal purity (%)	Plastic recovery rate (%)
1	80	27	9478	93.71	55.76
2	84	27	92.01	94.20	58.10
3	88	27	93.48	95.06	60.20
4	80	29	98.38	88.96	43.07
5	84	29	97.70	90.71	49.02
6	88	29	98.26	91.15	51.34
7	80	31	99.05	87.19	37.56
8	84	31	98.96	89.72	43.51
9	88	31	99.08	91.93	51.86
10	84	29	96.02	90.75	48.74

11	84	29	93.70	94.39	55.82
12	84	29	93.65	95.82	59.48

Results indicate that the most important factor is the angle α. By increasing the angle, a greater metal recovery rate was obtained, but also a smaller metal purity fraction. With the help of the software, it was possible to determine the optimal values of the angle α and the voltage V to maximize both the recovery and purity of metal and plastic fraction. The values are V = 88 kV and α = 31° corresponding to a metal recovery rate of 99.08% and a metal purity of 91.93% with 52% of non-metallic fraction recovery rate.

Bioleaching of heavy metals from spent household batteries using Acidithiobacillus ferrooxidans: statistical evaluation and optimization

In recent years, climate change has led the theme of recycling to assume ever greater importance [4]. Most battery models contain heavy metals that are toxic to both humans and environment. For this reason, recycling batteries is crucial to reduce the dispersion of these substances which can cause serious problems related to groundwater and atmospheric pollution [4]. The recovery of these materials constitutes an alternative to the traditional mining. Nowadays different recovery technologies are exploited, which include conventional (as pyrometallurgical and hydrometallurgical processes) or bio-processing methods [4]. Conventional methods are expensive and cause secondary pollution. The second ones, like bioleaching, are based on the ability of microorganisms to convert insoluble solid compounds into extractable forms. Bioleaching is applied for the recovery of materials from spent batteries with a strong interest to the Ni-Cd batteries which are the most toxic and are classified as hazardous waste. This process is applied for the bio-recovery of Ni, Ca and Co from spent Ni-Ca and NiMH batteries in order to investigate the possibility to let the process suitable to scaling it up to an industrial level because of the difficulty in separating solid waste according to the type of battery. To optimize the recovery percentage of the extracted heavy metals (Ni, Ca and Co), M. Ijadi Bajestani *et al.* implemented a design of experiments (DoE) approach [4]. Three effective factors were considered for experimental design: i) initial ferric ions (Fe^{3+}) concentration, since the mixture is composed by solid powder and the culture; ii) initial pH of the Acidithiobacillus ferrooxidans (it was proven as a potent leaching organism, for dissolution of metals from low-grade sulfide ores); iii) initial particle size of the battery powder. A statistical method with polynomial model (Box-Behnken design) was used to determine both the effects and the interactions of the three factors by varying each of them over three values, *i.e.*, Fe^{3+} (0, 5, 10 g/L), pH (1, 1.8, 2.6), particle size (37, 93, 149 µm). 17 test runs were conducted, as reported in ***Table 2***, and an atomic absorption spectroscopy (AAS) analysis was carried out to determine the quantity of recovered metals.

Table 2 *Box-Behnken design based on three significant parameters and the metals recovery as the responses. Adapted and reprinted with permission from [4].*

Run order	Experimental factors			Metal recovery (%)		
	Initial pH	Initial Fe^{3+} conc. (g/L)	Size (µm)	Ni	Cd	Co
1	1.80	0.00	37.00	70.0	41.3	58.3
2	1.00	5.00	149.00	45.4	72.3	48.0
3	1.00	10.00	93.00	64.4	73.7	70.3
4	1.00	0.00	93.00	78.2	85.0	43.1
5	1.00	5.00	37.00	100.0	46.9	100.0
6	1.80	5.00	93.00	50.6	71.4	58.6
7	2.60	0.00	93.00	74.2	100.0	48.5
8	2.60	5.00	149.00	41.0	92.3	41.0
9	1.80	10.00	37.00	79.3	42.3	84.9
10	1.80	5.00	93.00	73.6	99.7	74.1
11	1.80	5.00	93.00	57.6	81.2	57.4

12	1.80	5.00	93.00	61.1	80.4	60.8
13	1.80	10.00	149.00	42.4	75.1	50.5
14	2.60	5.00	37.00	77.8	43.8	70.0
15	1.80	0.00	149.00	51.9	78.7	38.4
16	2.60	10.00	93.00	44.8	63.7	39.9
17	1.80	5.00	93.00	49.6	66.3	48.7

Results indicated that minimizing initial powder size resulted in higher recovery efficiency for Ni and Co, while Cd reached its maximum recovery efficiency at the larger mesh size. Similar behavior for Ni and Co recovery was found considering the other factors, *i.e.*, the lower the pH value the higher the recovery efficiency. For Cd, increasing initial pH and decreasing ferric ions concentration led to the maximum recovery efficiency. The target was to optimize the synchronous extraction of the three metals, so the initial values of the factors were defined as follows: lowest initial pH (1), maximum initial ferric ions concentration (9.7 g/L) and a mean particle size (62 µm). This setting made possible to optimize the simultaneous extraction of the three metals (Ni, Cd, Co) from the bioleaching of solid waste made of metal compounds with the resulting percentage of 87% for the Ni recovery, 93.7% for Co and 67% for Cd.

Centrifugation based separation of lithium iron phosphate (LFP) and carbon black for lithium-ion battery recycling

Due to the increasingly widespread use of Li-ion batteries and, contextually, the difficulty in processing the raw materials, recycling of lithium, cobalt, manganese, copper and nickel from decommissioned batteries has become of great interest. Three main approaches are commonly adopted: i) pyrometallurgy; ii) hydrometallurgy; iii) direct recycling. Among these, pyrometallurgy is the simplest but also the least in terms of quantity and quality of the recycled metals. Hydrometallurgy, consisting of leaching, solution purification and metal recovery, is better in terms of final yield but demands prior physical separation and sorting phases of the battery components. Direct recycling is the most complex, with several techniques to be applied, but it has the advantage to recover fully functional active materials ready to be used in new battery production. A key step is the separation of cathode and anode components from the black mass which contains active materials. The cathode active material lithium iron phosphate (LFP) is processable in water, while nickel-based active materials suffer from contact with water. Centrifugation is one of the most studied and applicable methods to separate solid components from a liquid phase. In order to evaluate the applicability of this process to the separation of active materials, Wolf *et al*. investigated the efficiency of the mechanism applied to an aqueous dispersion made of LFP, carbon black (C65) and binders as carboxy methylcellulose (CMC) and polystyrene rubber (SBR). The scheme of the experimental centrifugation setup is represented in ***Figure 4***. The separation efficiency was defined as the ratio of the material separated within the centrifuge to the material that entered the centrifuge. The use of centrifugation was based on the different density and particle diameters of the LFP and C65: C65 were 10-50 nm in diameter, while LFP particles were few hundred nanometers in diameter.

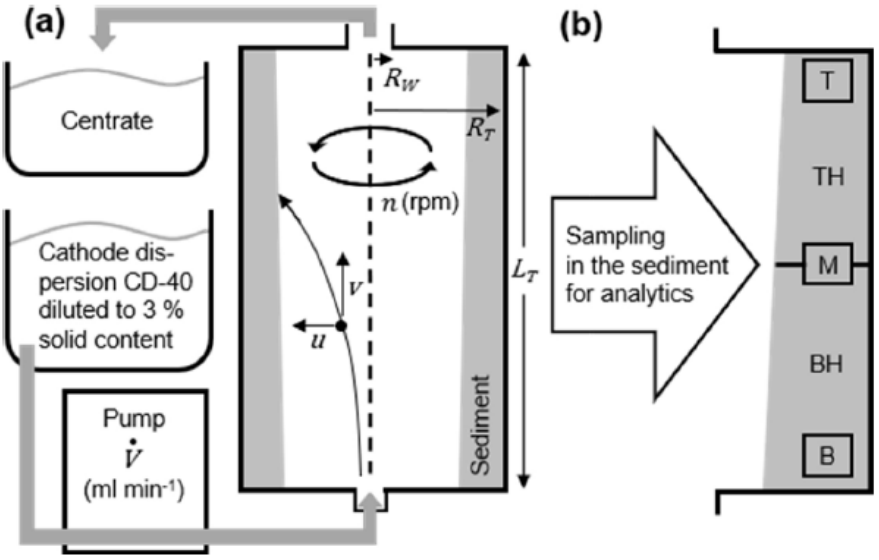

Figure 4 *(a) Scheme of the experimental setup. The volumetric flow rate was imposed through the pump and the centrifuge was set at a certain rotational speed. Dimensions of the centrifuge were defined. (b) Sampling in the sediments: T = top; TH = top half; M = middle; BH = bottom half; B = bottom. Adapted and reprinted with permission from [5].*

DoE was applied to investigate the dependencies on the working parameters of the three output values: T_{carbon}, T_{LFP}*(Leco)*, T_{LFP}*(XRF)*, which represented the separation efficiency of carbon and LFP analyzed by Leco and X-ray fluorescence, respectively. ***Figure 5*** represents the parameter space investigated via DoE.

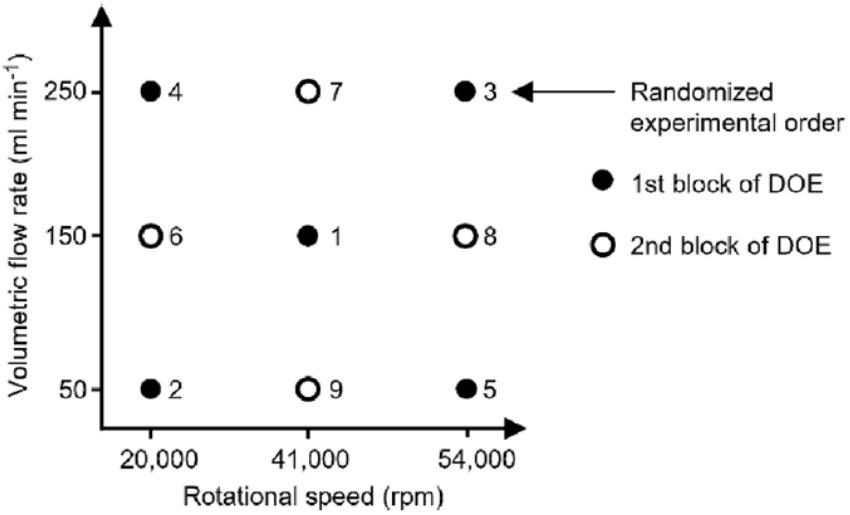

Figure 5 *DoE-investigated parameter space. Three rotational speed and volumetric flow rates were chosen and a total of nine experiments were conducted in randomized order. Adapted and reprinted with permission from [5].*

The strongest separation condition was achieved at 54000 rpm and 50 ml/min due to the indirect proportionality between the volumetric flow rate and the percolation time. The optimum working conditions were identified where most LFP was separated and as much carbon as possible was pushed into the centrate. In ***Figure 6*** the optimum was represented on overlapped response surface model (RSM).

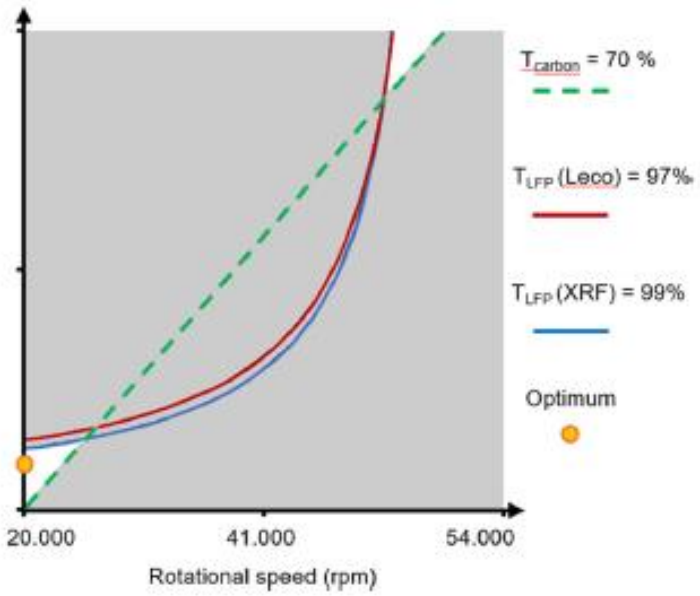

Figure 6 *Overlapped RSM for Tcarbon, TLFP(Leco) and TLFP(XRF). The optimum was individuated at 20000 rpm and 65 ml/min prioritizing the separation of LFP over the carbon. Adapted and reprinted with permission from [5].*

No evident difference was found comparing the centrifuged LFP's XRD patterns at DoE optimum with those of commercial LFP. Moreover, the specific average discharge capacity of centrifuged LFP was measured and was 98% of a commercial one, thus indicating a high quality of the centrifugation process focused on direct recycling of active materials from dismissed batteries.

Design optimization of selective lithium leaching of cathodic active materials from spent lithium-ion batteries based on the Taguchi method

The recycling of cobalt (Co), nickel (Ni) and manganese (Mn) constituting LIBs is actively performed while Li, which is present with a percentage of 4-7% in battery content, is not recovered for economic reasons. This because Li is recovered only after the recovery process of the other metals. Selective Li leaching process can avoid this drawback. Roasting is carried out to allow Li leaching in water. During the roasting phase, a chemical reaction occurs changing the active material ($LiCoO_2$ or LCO) into Li_2CO_3. After that Li_2CO_3 is leached in deionized (DI) water. Jung *et al.* focused on the study of the optimal roasting conditions and on the selection of the liquid-to-solid (L/S) ratio with the use of an experimental design based on Taguchi method [6]. The following steps were performed: i) selection of targets and design parameters to be evaluated; ii) determination of the number of parameters and interactions between the parameters; iii) identification of the orthogonal array (OA); iv) performing of the experiments based on OA; v) analysis of results with signal-to-noise (S/N) analysis and ANOVA; vi) identification of the optimal design parameter level and validation through experiments. The factors considered were the heat treatment atmosphere (air or N_2), powder size (0-25, 25-125, >125 µm), roasting temperature (550, 700, 850 °C), roasting time (1, 2, 3 h), L/S ratio (1:20, 1:25, 1:30 g:ml). The effects of heat treatment atmosphere, time and temperature were studied through X-ray diffraction (XRD) analysis. In ***Figure 7*** thermogravimetric analysis is shown depleting the difference in terms of temperature and decrease in weight associated to air and N_2 heat treatment atmosphere.

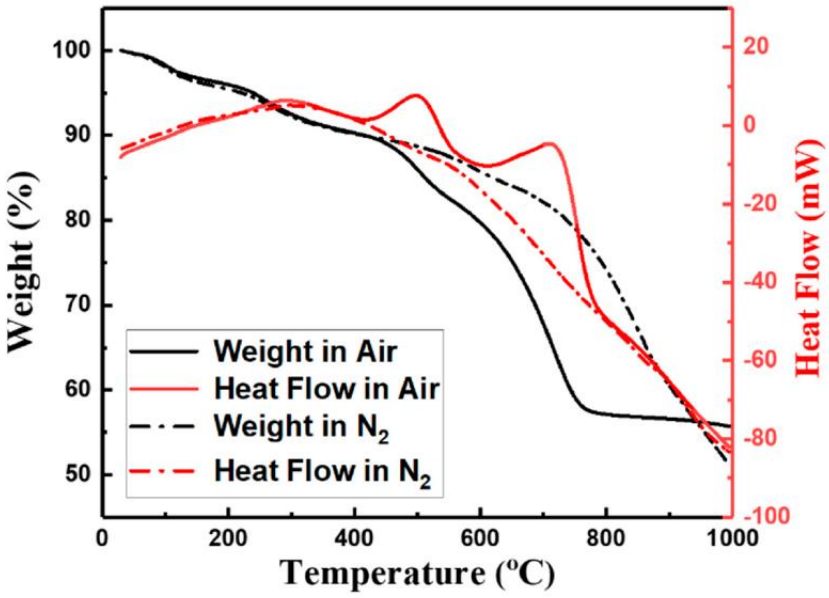

Figure 7 *Thermogravimetric analysis. In air the organic material containing carbon reacts at 437 °C with a marked decrease in weight up to 750 °C. In nitrogen atmosphere significant decrease in weight starts at 723 °C. Adapted and reprinted with permission from [6].*

The OA table L_{18} (2 x 3^4) was used and then S/N ratio, ANOVA and interaction analysis were performed. 18 experiments were carried out. About the S/N ratio, the term "signal" was associated to the desired value (mean) for the output characteristic, while "noise" denoted the value that interferes with the output object. The larger-the-better characteristic was used for this study, with *h* the Li leaching characteristic.

$$h = -10\log\left(\frac{1}{n}\sum_{i=1}^{n}\frac{1}{y_i^2}\right)$$

with y_i the i_{th} Li leaching.
ANOVA was carried out to verify whether the design parameters have a significant impact on the experimental results following the formula:

$$SS_T = \sum_{i=1}^{n}(\eta_i - \eta_m)^2$$

with *n* the number of experiments of OA, and η_i the mean S/N ratio of the i_{th} experiment. Moreover, the impact of the design parameter was investigated by using F test: the ratio of the mean of squared deviations (SS_m calculated as the sum of squared deviations divided by the number of degrees of freedom) to the mean squared error. The larger the F-value the greater the impact. The heat treatment was identified as the parameter with the greatest impact on Li leaching (see ***Figure 8***). Finally, the confirmation test was used as follows:

$$\hat{\eta} = \eta_m + \sum_{i=1}^{n}(\overline{\eta_i} - \eta_m)$$

with η_m the total mean S/N ratio, η_i the mean S/N ratio of the optimal level and *n* the number of major design parameters. Calculated and predicted values were identical, thus showing the accuracy of the model.

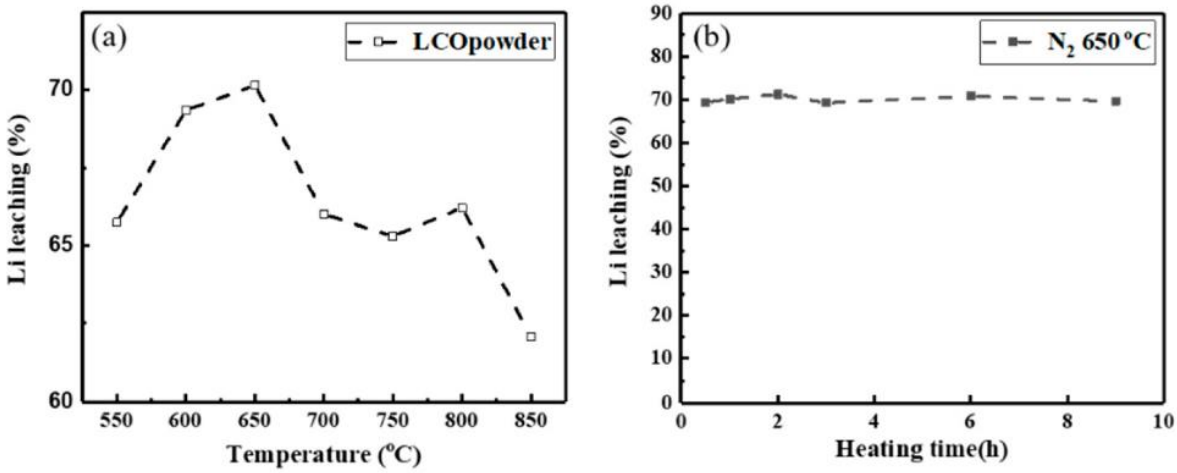

Figure 8 *Leaching result after heat treatment according to (a) temperature and (b) time in nitrogen atmosphere. The best result was obtained in nitrogen atmosphere with a roasting temperature of 650 °C and 2 h of treatment. Adapted and reprinted with permission from [6].*

The S/N ratio is showed in ***Figure 9*** attesting that the heat treatment had the major impact on Li leaching.

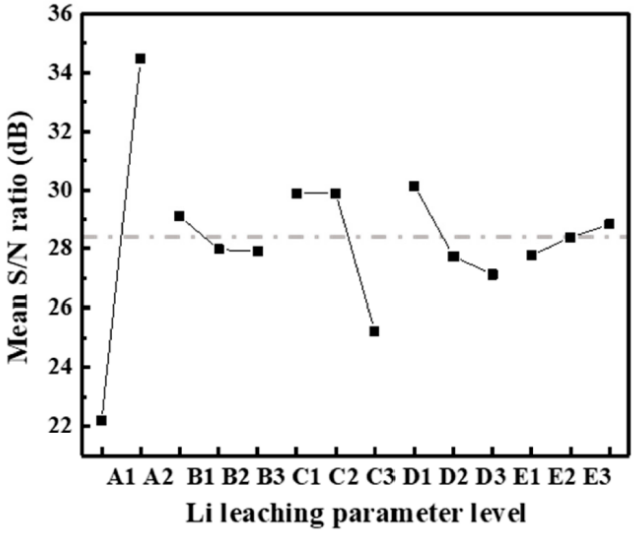

Figure 9 *S/N graph for lithium leaching ratio. Adapted and reprinted with permission from [6].*

With Taguchi method the optimal condition was found with 1 h of treatment at 700 °C in nitrogen atmosphere and 1:30 L/S ratio. The predicted Li leaching ratio using the parameter levels was 65.73%, which was quite similar to the actual value of 67.13%.

Lithium ion battery active material dissolution kinetics in Fe(II)/Fe(III) catalyzed Cu-H_2SO_4 leaching system

According to the hydrometallurgical recycling of LIBs, a wide range of lixiviants are used but only few of them are interesting in terms of price and technology. Sulfuric acid (H_2SO_4) remains one the most viable because of its low cost and chemical stability. To obtain excellent Co extractions, the active cathode materials in LIBs require a reductant due to the stability of the present higher-valence oxides. Different reductants in sulfuric acid were investigated. Hydrogen peroxide (H_2O_2) is one of them. It was widely considered because no impurities are added into the process. On the other hand, it acts as an oxidant to most of other elements and compounds in the battery waste and it is readily decomposed catalytically through reactions involving radical formation by Fe^{2+}. It is common that the LIB waste can contain traces of

metallic Al, Cu and Fe. Even if good mechanical separation of these materials from the active material rich fraction can be achieved, significant quantities of them can remain. It is essential to understand the behavior of these materials in the leaching system. It was reported that a H_2O_2 free leaching system could potentially use dissolved Fe and elemental Cu for the reduction of $LiCoO_2$. Porvali *et al.* investigated the kinetics of the leaching system based on the following catalytic reaction including Fe, Cu and $LiCoO_2$ [7]:

$$2LiCoO_2 + Cu + 8H^+ \xrightarrow{Fe(II)/Fe(III)} 2Li^+ + 2Co^{2+} + 4H_2O + Cu^{2+}$$

The experiments were performed in a 500 cm^3 reactor heated to a target temperature. 400 cm^3 of lixiviant were used. Ferrous sulfate ($FeSO_4 \cdot 7H_2O$) was added and included in the total volume; a constant N_2 (g) purging was applied to avoid undesirable reactions. Cu powder (< 425 µm) was added after 10 min of purging and after further 10 min, 6.68 g of $LiCoO_2$ was added. Sampling intervals were 5, 10, 15, 30, 60, 120 min. The collected residues were filtered, dried and analyzed with X-ray diffraction (XRD). Central composite design (CCD) was used according to the principles of DoE. Ferrous sulfate and copper metal were the investigated factors and the responses recorded were reaction rate constant by cubic rate law at 0-30 min and 30-120 min. It was reported that Fe(II) strongly influenced the dissolution of $LiCoO_2$ in sulfuric acid and the presence of $LiCoO_2$ influenced the dissolution of Cu. In ***Figure 10*** the effects of ferrous ions on CO extraction are represented.

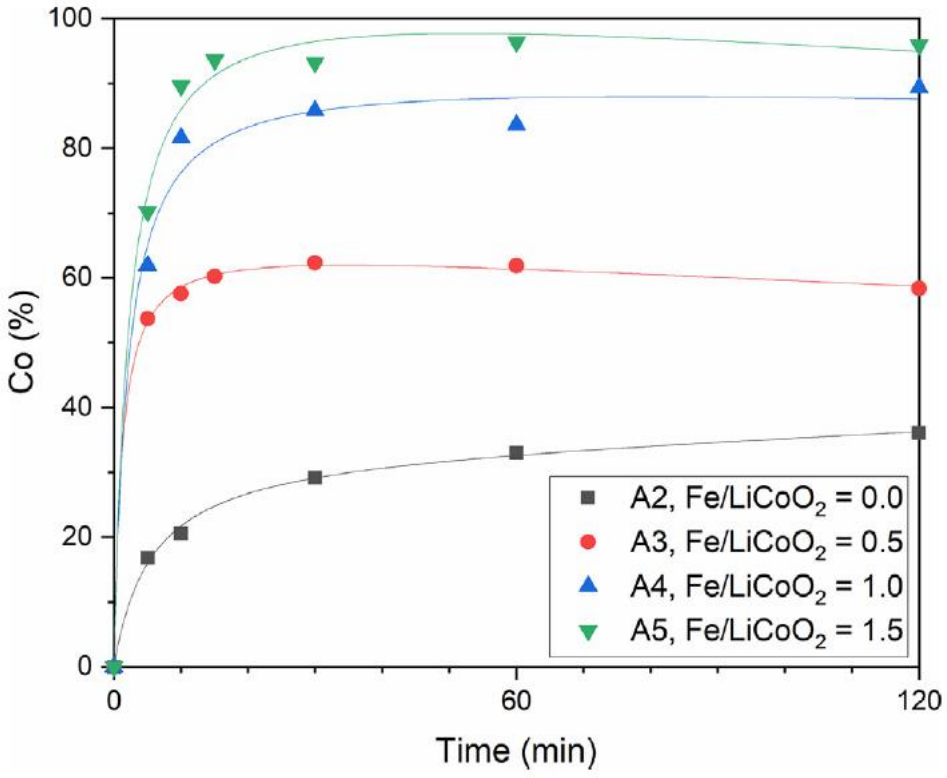

Figure 10 *Effect of ferrous ions on CO extraction from $LiCoO_2$. Ferrous sulfate enhanced $LiCoO_2$ leaching substantially. In stoichiometric condition the CO extraction reached 90%. With 1.5 times the stoichiometric excess an almost complete CO dissolution of 96% was assessed. Also, the presence of Fe accelerated the reactions: within 5 min CO extraction of minimum 53% was achieved. Adapted and reprinted with permission from [7].*

The presence of Cu did not enhance CO extraction. Cu dissolved faster when added immediately with $LiCoO_2$.

DoE was also performed in order to investigate the reaction rates and the relation of their change as a function of Cu/$LiCoO_2$ (mol/mol) and Fe/$LiCoO_2$ (mol/mol) content. Two regression models were created

from reaction rate constants: i) model 1 for < 30 min; ii) model 2 for > 30 min. Based on experimental data, reaction rates were fitted applying the cubic rate law as follows:

$$1 - (1 - x)^{\frac{1}{3}} = k_c \cdot t$$

Backward elimination was used to remove statistically insignificant terms: $[Fe]^2$ was removed ($p < 0.1$). $[Cu]^2$ was included to interpret the results in terms of uncertainty. Analysis of variance (ANOVA) was thus performed. [Fe] and the combination of iron and copper had the strongest influence on the $LiCoO_2$ dissolution reaction rate. Both [Fe] and [Cu] alone had a negative effect on the reaction. Contour plots are shown in ***Figure 11***.

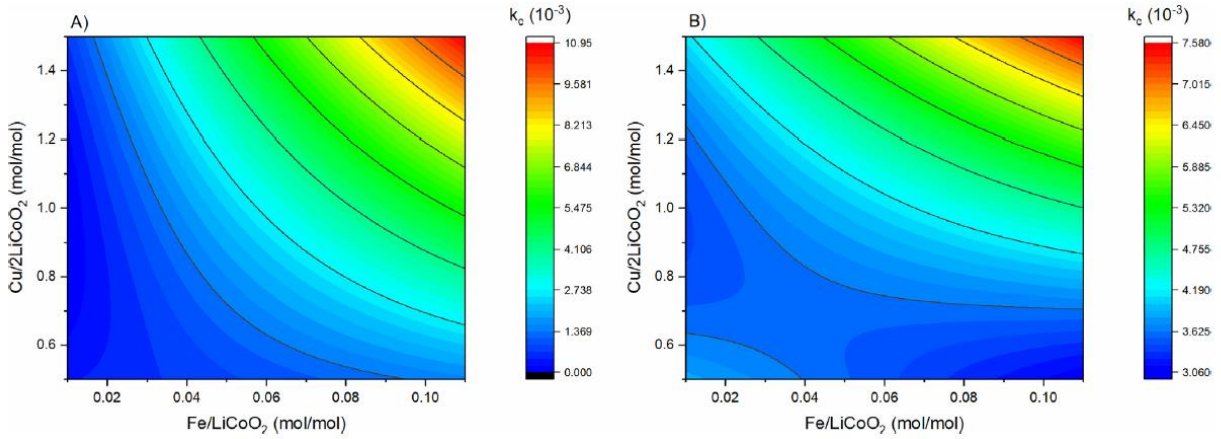

Figure 11 *A) Contour plot of the model 2 representing the prediction of the reaction rate constant past the 30 min point: it demonstrates the interaction of [Fe·Cu] as non-vertical and non-horizontal lines and the curvature in lines as effect of the $[Cu]^2$. B) Prediction of model 1 for time < 30 min: the effect of noise for $k_c < 3.625$ is evident. Adapted and reprinted with permission from [7].*

Moreover, Fe levels were inspected during leaching. Experiments with low amount of Fe and center quantity of Fe were compared in terms of Co extraction. For both experiments the decrease of Fe was constants (6%) from 5 to 120 min. After that, molar quantities of dissolved copper and cobalt were compared. It was seen that the ratio initially increased meaning that the dissolution kinetics of Cu was slower than that of Co. Comparing other experiments with low level of Fe it was confirmed that Co was dissolved by sulfuric acid alone. The reason of the poor dissolution kinetics of $LiCoO_2$ could be related to an insufficient mass transfer and reaction site opportunity.

Recycling of Primary Lithium Batteries Production Residues

Nowadays Li anode production residues are treated as waste but lithium recycling from EOL products and production residues have become crucial due to the increase of the batteries market. M. Kahl *et al.* proposed a method to recover lithium from production waste as a lithium salt [8]. The method consisted in thermal oxidation of pure Li to Li_2O at T = 300 – 400 °C. The entire process is represented in ***Figure 12***. After the oxidation the product was dissolved in deionized water, filtrated and eventually crystallized as $LiOH \cdot H_2O$. The purity was > 99.5%.

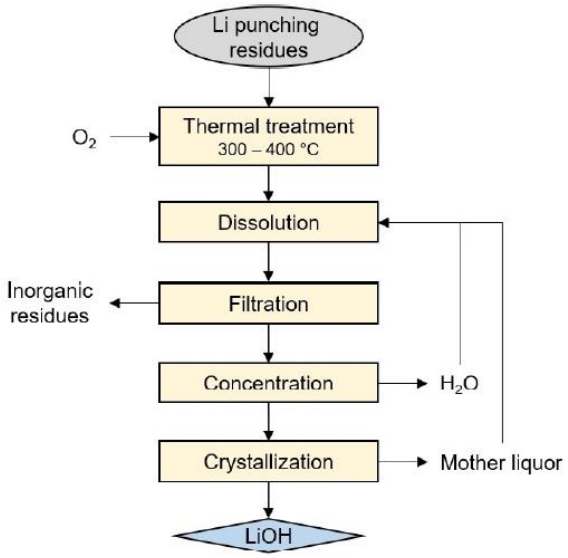

Figure 12 *Recycling process scheme of Li battery production residues. Adapted and reprinted with permission from [8].*

The dissolution of $Li_{(s)}$ in water is characterized by a high energy release and hydrogen generation. To avoid this, $Li_{(s)}$ was converted into $Li_2O_{(s)}$ and then dissolved with a reduction of energy release of 70% and the final product $LiOH_{(aq)}$. Among three different compositions of Li batteries production residues, crumpled metallic residues group, which had the highest Li-content and the highest purity, was chosen to perform the investigation. Oxidation is affected by several parameters. Ambient temperature, Li-sheet thickness and residence time were investigated. Results from experiments showed that a higher temperature increased the efficiency and reduced time residence of the oxidation. In particular, the temperature of 400 °C reduced the time from 15 to 1 h. From these considerations the next step was to optimize reaction parameters to make the approach suitable for industrial application. To do this a DoE was adopted. A 3^3 Box-Behnken approach, showed in ***Figure 13***, was used with 3 factors: i) temperature *T*; ii) residence time *t*; iii) Li-sheet thickness *d*. The target was the conversion of Li to Li_2O. According to the ANOVA analysis, among the nine effects (single, quadratic and binary correlations) only 5 were significant.

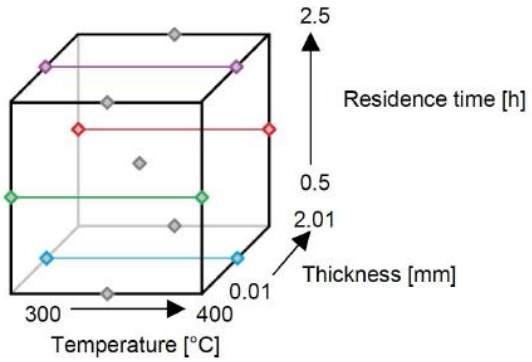

Figure 13 *3^3 Box-Behnken experimental design. Adapted and reprinted with permission from [8].*

T and its squared correlation had the highest impact on Li conversion; with a *T* equal or above 400 °C (which was defined as ignition temperature) oxidation was complete. Thickness was the second most effective linear factor with its quadratic effect and correlation with temperature. These 3 factors had a small influence compared to the temperature. Residence time had a small impact. After oxidation, dissolution was conducted for 15 min with pure water. A closed loop between dissolution and precipitation was then realized to reach a complete recovery of Li. Model equation was defined using a multi-linear regression as follows:

$$Li - conversion\ (\%) = 932.894 - 5.417 \cdot A - 104.905 \cdot B + 6.869 \cdot C + 0.008 \cdot A^2 + 0.211 \cdot A \cdot B + 11.546 \cdot B^2$$

with A the temperature, B the thickness and C the residence time. The optimal conditions were: A = 400 °C, B = 2 mm and C = 2.5 h. Two experiments were performed to validate the model with a Li conversion of 96.9 ± 2.6%.

The COOL-Process—A Selective Approach for Recycling Lithium Batteries

The COOL-process (CO_2-leaching) is a selective direct carbonization process to recover Li from LIBs by the use of selective leaching properties of supercritical CO_2/water. According to the fact that all LIBs have the same basic structure, it is really promising because it is applicable to all kinds of LIBs and constitutes an alternative to conventional pyrometallurgical and hydrometallurgical methods. Moreover, supercritical fluids are interesting alternatives to traditional solvents used for metal extraction. In general, LIBs are constituted as follows: a cathode made of aluminum foil with intercalated Li compound, an anode made of a copper foil with graphite coating; a porous polyolefin separating anode and cathode; the electrolyte consisting in a mixture of an organic solvent and a lithium salt all enclosed by a sealed capsule made of steel, aluminum and various plastics. Originally, this process was applied for the production of Li_2CO_3 from lithium containing ores. Then it was investigated for the recovery of Li from black mass. The process scheme is depicted in ***Figure 14***.

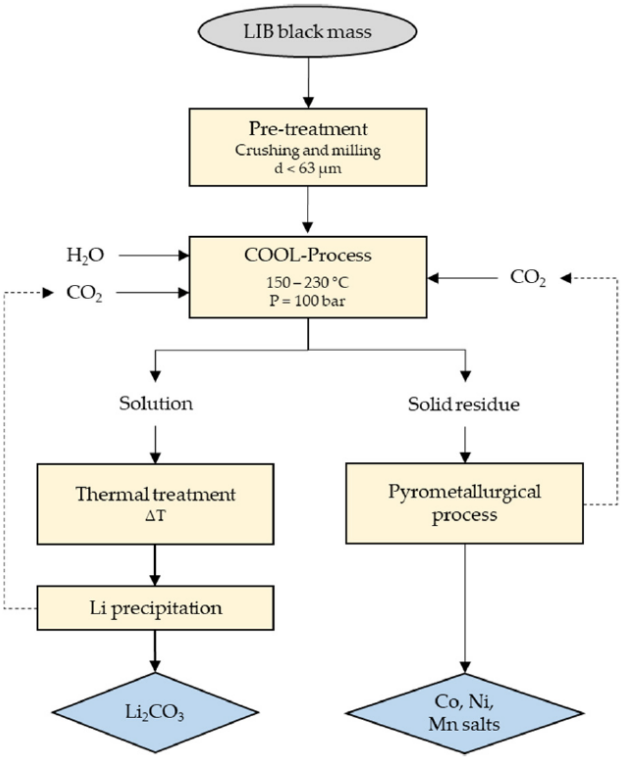

Figure 14 *Scheme of COOL-process. Adapted and reprinted with permission from [9].*

The method consists of a pre-treatment in which the black mass is crushed and milled to obtain grinded samples of size < 0.63 µm. After that, an atomic emission spectrometry and an atomic absorption spectrometry are used to determine the composition of the black mass. The next step consists in digestion of the mass at high pressure (100 bar) and other reaction conditions, which were object of investigation by Sandra Pavòn *et al.* through the application of DoE to optimize the Li recovery yield [9]. The adopted method was a 3^3 Box-Bhenken design. The 3 factors considered were: i) temperature *T* [°C] (A); ii) residence time *t* [h] (B); iii) water:black mass *L:S* ratio [mL/g] (C). 3^3 Box-Bhenken levels for the 3 factors were:

T: 150, 190, 230 [°C];

t: 2, 3, 4 [h];

L:S ratio: 30, 60, 90 mL/g.

The statistical evaluation was carried out with Statgraphics v.18. The model equation describing Li_{yeld} and taking into account contributions of linear, squared and correlated 3 factors was:

$$y = b_0 + \sum_{i=1}^{N} b_i x_i + \sum_{1 \le i \le j}^{N} b_{ij} x_i x_j + \sum_{i=1}^{N} b_{ii} x_i^2$$

with y the Li_{yield} [wt.%], N number of factors, b_0 ordinate section, x_i factors, b_i ,b_{ij}, b_{ii} regression parameters of linear, squared and cross effects. According to the 3^3 Box-Bhenken method, 15 tests were performed: one on every half of the edges and 3 in the center to determine the experimental error. Results are shown in ***Figure 15***. Temperature linear effect had the most pronounced effect on Li_{yeld} followed by *L:S* ratio also in terms of linear effect. Thirdly, the correlated *T* and *L:S* ratio effect also impacted on the Li_{yield}. Residence time influence was instead really poor. According to these results, the model equation which took into account only the effects with a consistent influence on Li_{yield} was defined as follows:

$$Li_{yield}(wt.\%) = 19.6125 + 0.178 * A + 1.9275 * B - 0.43977 * C + 0.00339 * A * C$$

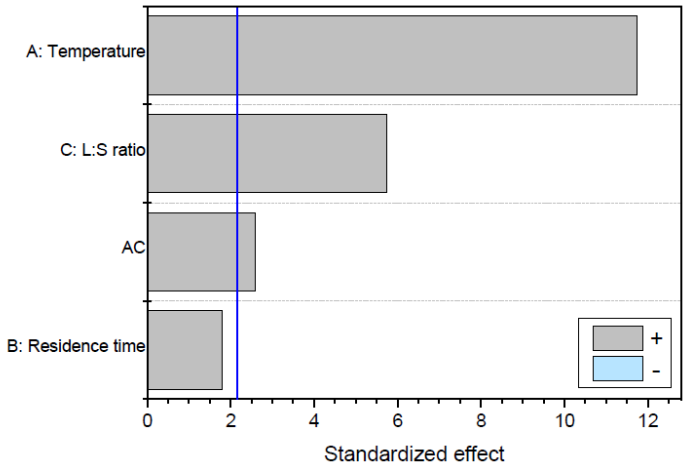

Figure 15 *Pareto diagram with significant effects on Liyield. Adapted and reprinted with permission from [9].*

The model equation predicted an absolute maximum with 98.8 wt.% with the following conditions: *T* = 230 °C, *t* = 4 h, *L:S* ratio = 90 mL/g. The mathematical model was verified carrying out two experiments with the conditions mentioned above. Both experiments had a Li_{yield} value of 94.50 ± 0.33 wt.%. ***Figure 16*** represents the Li_{yield} in terms of surface response with residence time of 4 h.

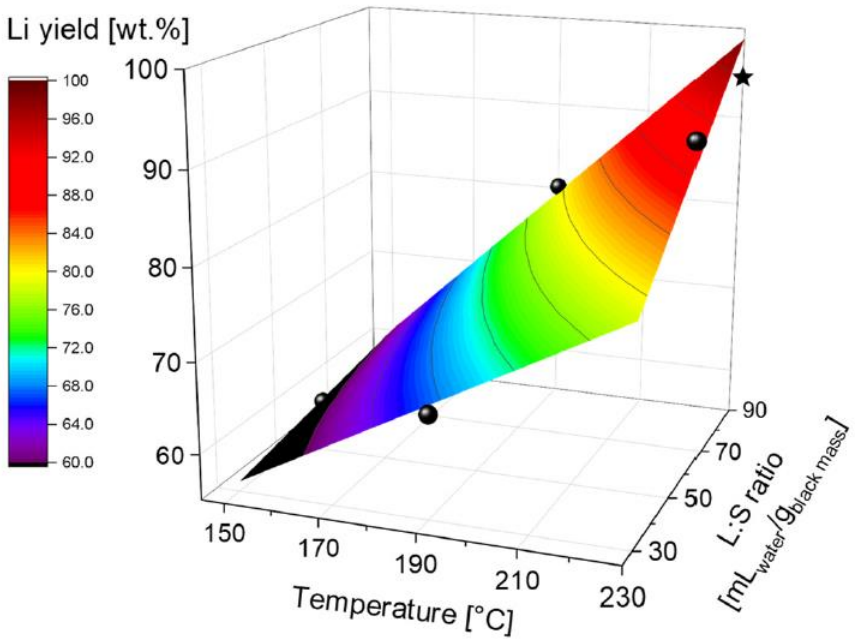

Figure 16 *Li yield determined by the mathematical model equation varying the temperature and L:S ratio, at a constant residence time of 4 h. Bold points correspond to the experimental data and the star point to the optimum obtained experimentally. Adapted and reprinted with permission from [9].*

In this case the optimum was placed in a corner of the Box-Bhenken DoE raising the question of whether another factor (e.g. pressure) needs to be investigated [9]. A more complex DoE, for example based on a full-factorial design, can be carried out.

Two-step leaching process and kinetics for an eco-friendly recycling of critical metals from spent Li-ion batteries

Disposing of spent lithium-ion batteries (SLIBs) in landfills can cause environmental and ecological problems, so effective management of SLIBs is crucial. The metal values in SLIBs can be recovered as a secondary resource. Both mineral and organic acids were used for metal dissolution of SLIBs; in this contest, Karan Chabhadiya *et al.* investigated a new hybrid approach consisting in sequential leaching with both organic ($H_2C_2O_4$) and mineral (H_2SO_4) acids [10]. The study used a Taguchi's orthogonal array design of experiments to optimize the following parameters: i) acid concentration (OA and SA for organic and sulfuric mineral, respectively); ii) pulp density (PD); iii) hydrogen peroxide dosage (HPD); iv) temperature (*T*); v) time (*t*). It focused on the leaching of second-generation lithium nickel cobalt manganese (LNCM) cathodes, which have a complex nature and make the leaching process difficult. ***Figure 17*** shows the steps of the recycling process. Spent Li-ion batteries were discharged by soaking in a 10% NaCl solution for 72 h. Then each battery was dismantled to separate plastics, aluminium and copper foils and collect the cathode powder which was sieved to select dimensionally homogenized particles. A sample was picked up to be analysed and define metal contents. Then the powder was ready for the 2-steps leaching process. Taguchi's orthogonal array design of experiment (OA-DoE) technique was used to optimize the conditions for leaching. The five parameters that influence the leaching efficiency, such as reaction time, temperature, pulp density, reductant dose, and lixiviant concentration, were chosen based on literature. These parameters and their ranges were then used in a L25 OA-DoE to conduct 25 sets of experiments.

The Taguchi method includes an objective function η called the signal-to-noise ratio (S/N), which measures the mean and the standard deviation of the output from the desired value and helps to ensure the process is not affected by undesirable conditions. The S/N is expressed in a logarithmic form to reduce the effect of noise factors during experimentation.

$$\frac{S}{N} = -10 \cdot \log_{10}\left(\frac{1}{n_R}\right) \cdot \left[\sum \frac{1}{y^2}\right]$$

with *y* the output data obtained from the experiments (leaching efficiency of metals) and n_R the number of replicates.

An additive model, which includes analysis of mean (ANOM) and analysis of variance (ANOVA), was used to predict the influence of the input parameters on the response/output parameters. The deviation of each parameter from the overall mean was determined using the ANOM, and the leaching efficacy was predicted using the S/N. The objective function obtained from the S/N that yields the maximum leaching efficiency of metals is referred to as *η* best.

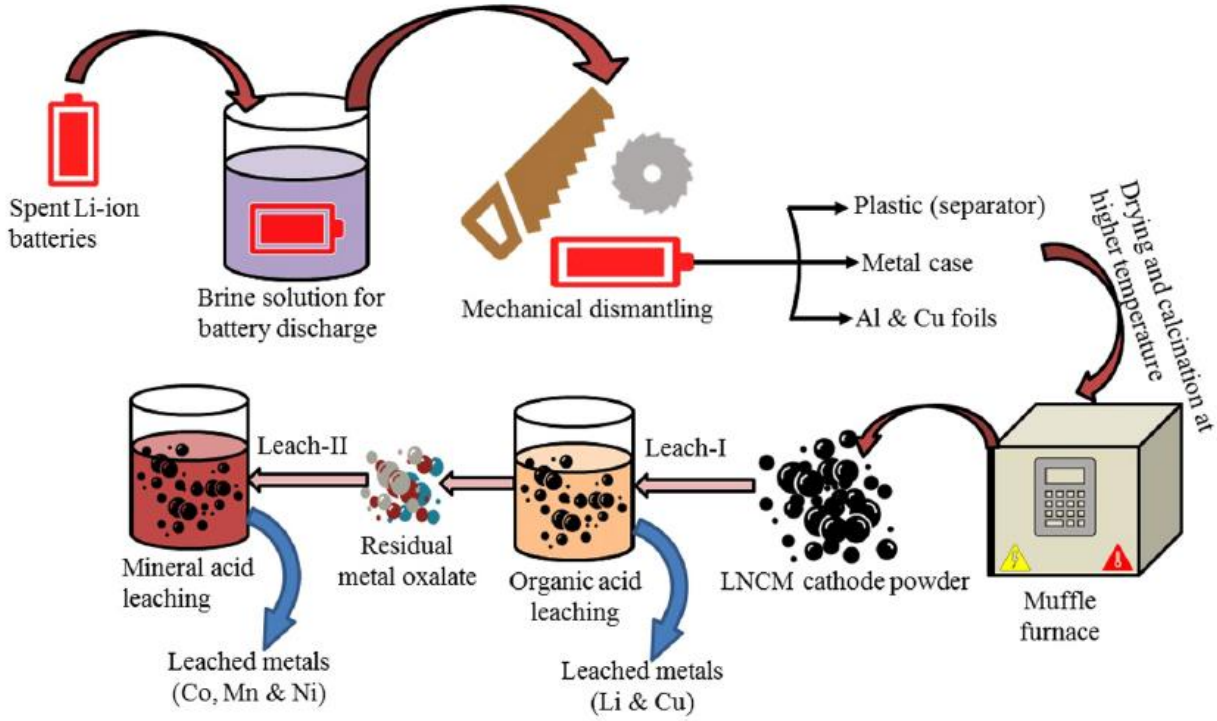

Figure 17 *Schematic of the process performed for recycling of LIBs cathode powder. Adapted and reprinted with permission from [10].*

After the 1-step of leaching using organic acid, leach residue was fed to the 2-step in sulfuric acid. After that, the solution was filtered and analyzed to determine the leaching efficiency of metals as follows:

$$\%\ Leaching = \left(\frac{M_{LL}}{M_{IS}}\right) \text{x } 100$$

with M_{LL} the output volume of leach liquor and M_{IS} the metal contents in the input mass of sample.

S/N ratio computed with larger the better equation was shown in ***Figure 18***. According to the results for the 1st-step leaching in which copper and lithium were the object of the dissolution (cobalt, nickel and manganese had negligible dissolution during the organic leaching), the order from the most to the least influent was: t_1 > HPD_1 > OA > PD_1 > T_1 for lithium and t_1 > T_1 > OA > HPD_1 > PD for copper. Moreover, the leaching was tested using the optimal conditions: OA = 0.25 M, PD_1 = 10%, HPD_1 = 0.5%, T_1 = 80 °C and t_1 = 90 min with a quantitative dissolution > 99% both for lithium and copper. These results validated the Taguchi OA-DoE. As for the 1st-step leaching, the results with optimal parameters for 2nd-step, which were:

SA = 3 M, PD_2 = 6 %, HPD_2 = 2 %, T_2 = 60 °C and t_2 = 120 min, validated the Taguchi OA-DoE with a leaching efficiency of cobalt, nickel and manganese of ~ 99%.

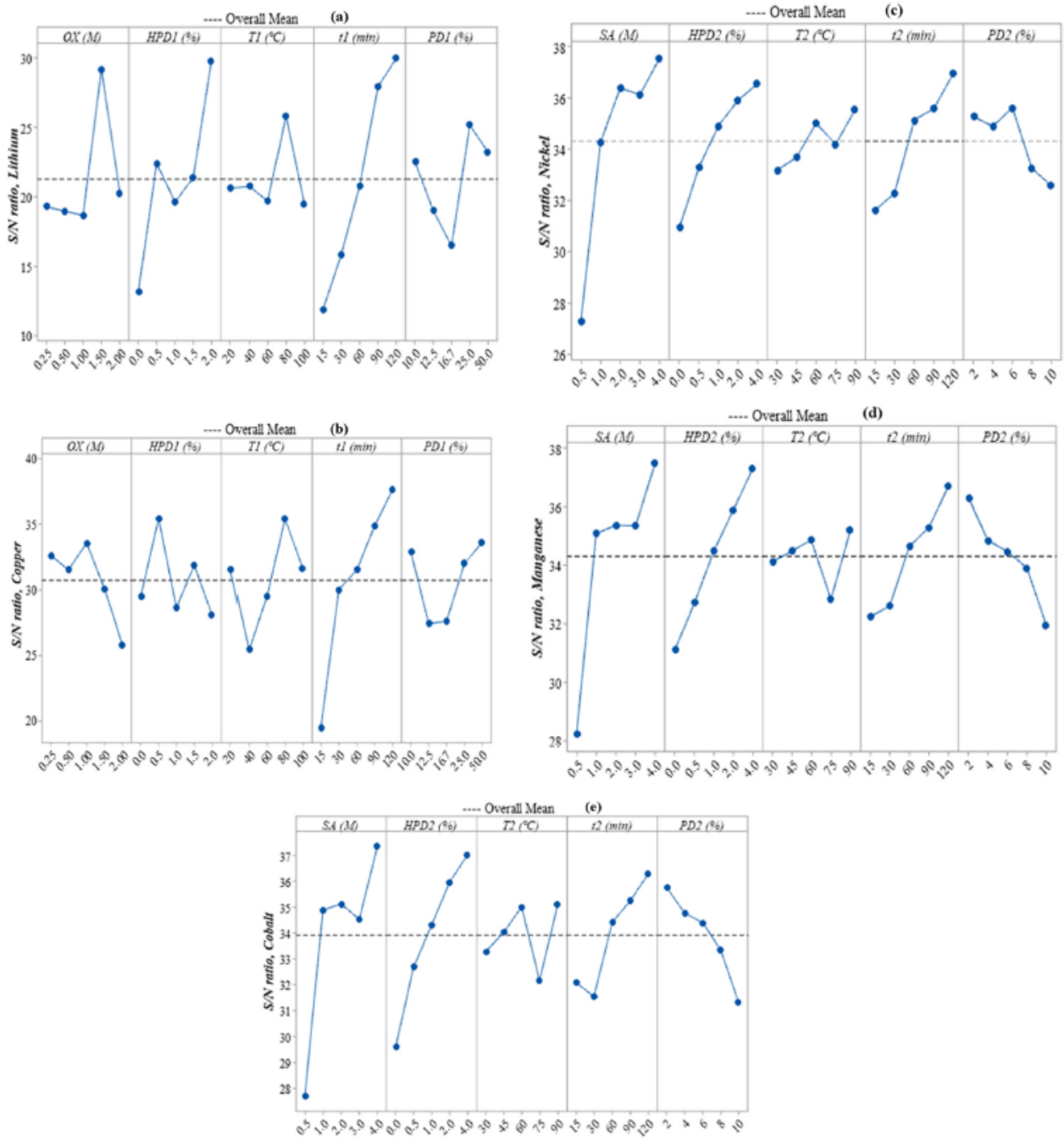

Figure 18 *Parametric effects on leaching of LNCM at larger the better S/N ratio. Adapted and reprinted with permission from [10].*

The results of the study will contribute to a better understanding of the behavior of acids and the selectivity of metals during leaching, leading to improved recycling processes and environmental sustainability.

Section 2.2: DoE for Battery Performance and Aging

A dynamic state-of-charge estimation method for electric vehicle lithium-ion batteries

Accurate estimation of SOC is fundamental to automotive market. Model-based methods are widely chosen over non model-based ones due to their robustness. Associated to these methods, non-linear system estimation algorithms as extended Kalman filter (EKF) are used; this algorithm needs to linearize the non-linear system in the actual estimation process, and it shows the disadvantage of performance degradation when solving nonlinear problems. Liu *et al.* proposed an unscented Kalman filter (UKF): a mathematical function used to estimate the result of applying a given nonlinear transformation to a probability distribution that is characterized only in terms of a finite set of statistics [11]. Particle filter algorithm was also applied as an effective algorithm to solve non-linear problems. In this way, an unscented Kalman particle filter (UPF) was adopted. A Thevenin model with parameters affected by SOC and temperature was defined: a representation of the model is shown in ***Figure 19***.

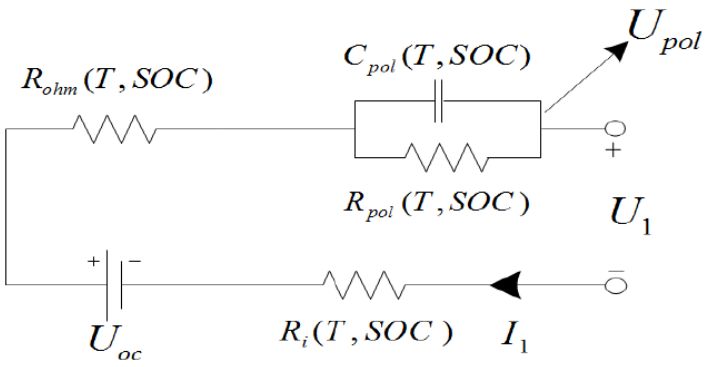

Figure 19 *Variable parameter Thevenin model. Open circuit voltage U_{OC} is calculated as the sum of the terminal voltage U_1, the polarization voltage C_{pol} and the product of the internal ohmic resistance R_{ohm} and other internal resistance R_i per I_1 which is the battery charge/discharge current. Adapted and reprinted with permission from [11].*

Identification of battery model parameters was realized with a discrete data fitting method. SOC and temperature were used as input for the fitting of the equivalent internal resistance model. Then, DoE based on Central Composite Design (CCD) was applied as shown in ***Figure 20***.

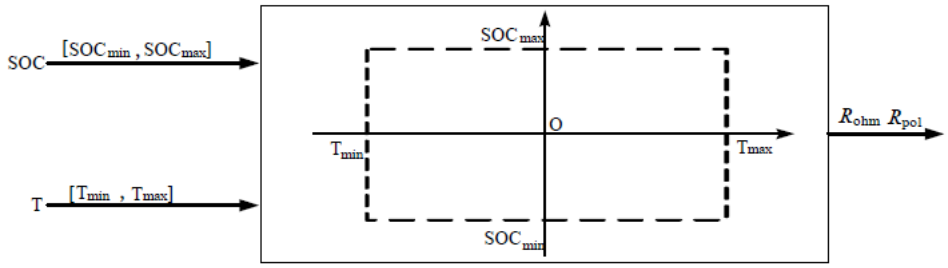

Figure 20 *Internal resistance DoE model based on CCD. R_{ohm} and R_{pol} were identified, R_i was ignored since it was much smaller than the other two. Adapted and reprinted with permission from [11].*

The fitted equation for C_{pol} was identified and, consequently, SOC state equation depending on temperature was expressed. For verification, 20 cycles of dynamic stress test (DST) were selected. Mean absolute error (MAE) was used to evaluate the fit of the battery model. In ***Figure 21*** SOC estimation at -10 °C is shown to demonstrate the high accuracy of the UPF-based SOC estimation model over other algorithms.

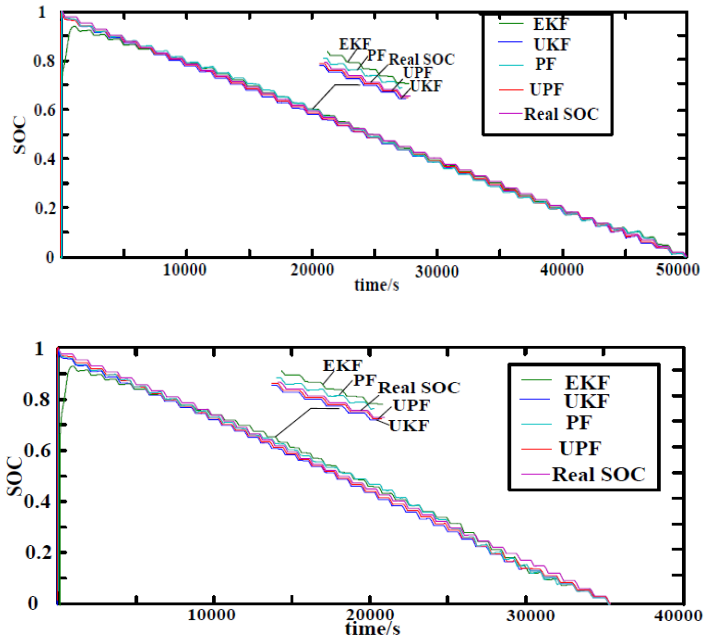

Figure 21 *Estimation of different algorithms at 25 °C and -10 °C, respectively. UPF-based SOC algorithm reached the best accuracy at 25 °C and low temperature. Adapted and reprinted with permission from [11].*

Verification of the effectiveness of the method in the dynamic process was finally realized using the federal urban driving schedule. Also in this case, the model reached better accuracy than other methods for both 25 °C and -10 °C.

A novel methodology for non-linear system identification of battery cells used in non-road hybrid electric vehicles

Since the state of charge is not measurable online, its estimation can be made in the battery management system (BMS), where a SoC estimator based on a non-linear battery model is implemented. Non-road hybrid electric vehicles and machinery need high power densities and loads dynamics, which makes the modelling of the batteries more complex. Three battery model approaches are commonly reported in the literature: i) equivalent circuit models; ii) electrochemical battery models; iii) data-based battery models. All these models require measurements, which are obtained by applying a current excitation to the battery cell and recording the voltage response. In this context, model-based design of experiment can be applied to create optimal excitation signals. To reach this goal, starting from a reference model, the information obtained is maximized and parameters can be estimated with minimum variance. Unger *et al.* used a local model network (LMN) which consists in a series of local linear models (LLMs) interpolated each other to give a non-linear output. This model is constructed by an iterative algorithm which begins with a global linear model to reach a threshold after a number of iterations. Unger *et al.* used a local linear model tree (LOLIMOT) algorithm [12], which is shown in ***Figure 22***.

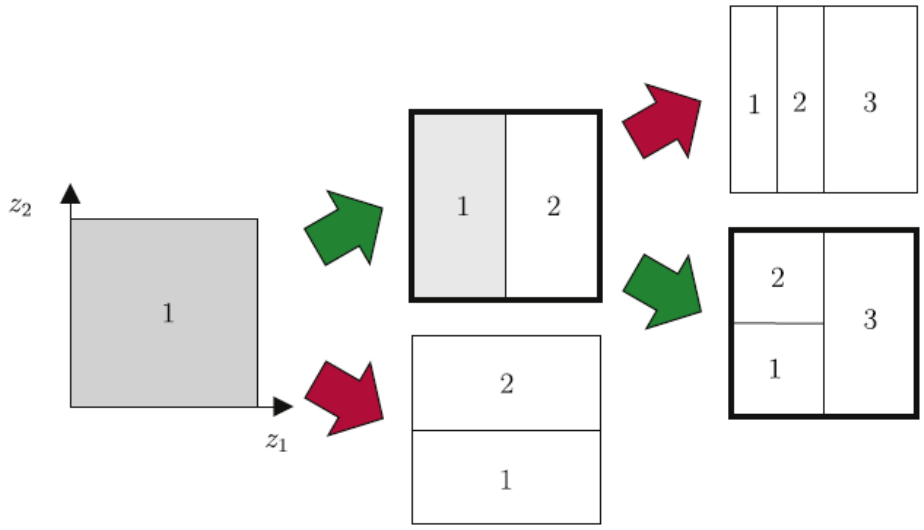

Figure 22 *LOLIMOT algorithm scheme for two-dimensional partition space. It consisted in dividing the partition space by axis-orthogonal splits and, iteration by iteration, the worst LLM was found by the quadratic error criterion and is split into two new LLM until a certain threshold is reached. Adapted and reprinted with permission from [12].*

It was fundamental that the system dynamics were sufficiently excited and that all SoC range was covered during the measurements, even more in non-road applications. A load current excitation signal *U* was defined and applied to a battery cell and cell voltage was recorded. Optimized high dynamic excitation sequences were created by optimal model-based design of experiments. Fisher information matrix (FIM), a way to measure the information content of a signal, was applied for optimization purpose. The optimal excitation signal *U* was then applied respecting the battery constraints in terms of current values, battery voltage limits and SoC. The current constraints were defined taking into account a real road cycle. ***Figure 23*** shows the construction of the constraints for the optimization.

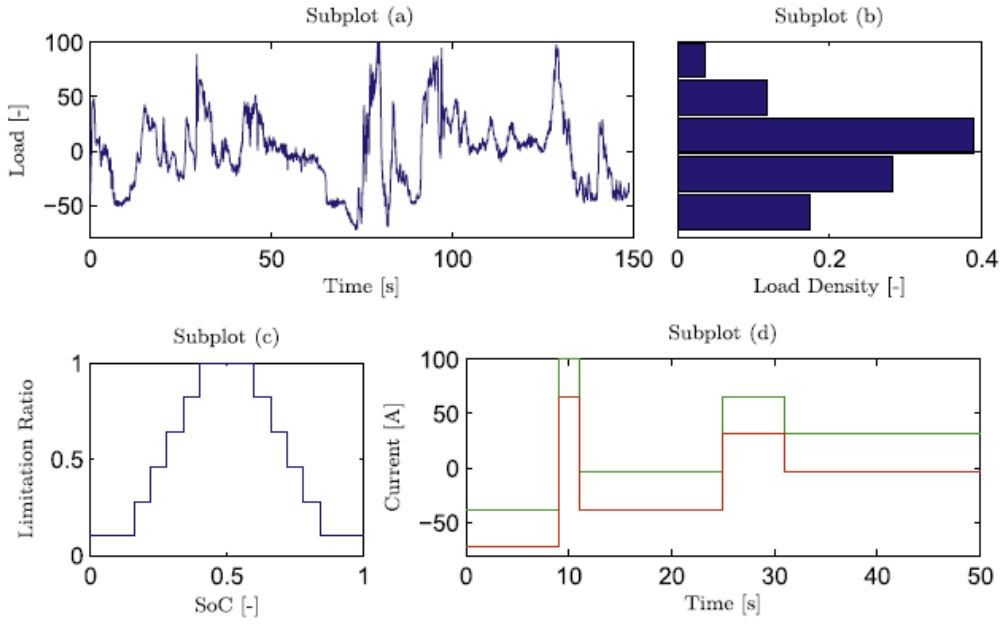

Figure 23 *Selection of constraints for optimization. Scaled real road cycle was used to construct the histogram subplot (b). Subplot (c) shows the limitation ratio of the applied min and max current depending on the SoC. Subplot (d) shows current constraints. Adapted and reprinted with permission from [12].*

Measurement procedure was also defined in order to avoid different initial battery conditions and so excluding unexpected and undefined effects during measurements. The procedure is reported as follows:

1. Initial capacity check at 25 °C
2. Set temperature of climate chamber
3. Fully charge the battery cell
4. Discharge until initial SoC is reached
5. Apply excitation signal
6. Repeat 3 to 5 until all excitation signals are recorded
7. Repeat 2 to 6 until all temperatures are recorded

The results showed that DoE approach resulted in an increase in accuracy of the model starting from a linear reference model used for the optimization of the excitation signal.

Capacity and power fade cycle-life model for plug-in hybrid electric vehicle lithium-ion battery cells containing blended spinel and layered-oxide positive electrodes

Referring to the spread of plug-in hybrid electric vehicles (PHEVs), great interest was dedicated to the development of reliable models to describe capacity and power fade of Li-ion batteries in order to predict the long-term evolution of capacity and resistance. These activities are referred to battery prognosis and are really important for the life-cycle management of EVs. Battery aging models are developed to make this possible. Battery aging models can be classified as physics-based or semi-empirical. The second one is simpler even maintaining a good accuracy, so it is used even more. Andrea Cordoba-Arenas *et al.* approached the investigation of battery aging under PHEV operation by developing a semi-empirical model applied to Li-ion batteries constituted by blended cathodes [13]. This kind of cathodes is composed of layered-oxide positive electrodes as $LiNi_{1/3}Nm_{1/3}Co_{1/3}O_2$ (NMC) and spinel oxide positive electrodes as $LiMn_2O_4$ (LMO); they were considered the most promising for PHEV applications. The reason stays in the combination of their single characteristics: NMC is characterized by high specific capacity and good thermal stability. LMO has high-rate capability and low cost. The factors which were studied to investigate their influence on capacity and power fade of LIBs were: i) charge sustaining/depleting operation; ii) minimum SOC; iii) charging rate (CR); iv) temperature. Charge depleting (CD) operational mode was defined as the operation of the vehicle on electric and hybrid mode: this consists in a net decrease of SOC. Charge sustaining (CS) mode was defined as the pure hybrid mode with a relatively constant battery SOC. During CD the battery was depleted starting from a SOC_{max} to a defined SOC_{min}. During CS the SOC is kept to an average value of SOC_{min}. To take into account the two different operational modes, a ratio was defined as:

$$Ratio = \frac{t_{CD}}{t_{CD} + t_{CS}}$$

assuming the value of 1 if all the operating time is spent in CD; 0 if all the operating time is spent in CS and a value between 0 and 1 for mixed operation. Four factors were chosen for DoE as follows:

- Charging rate (CR)
- Battery skin temperature (T)
- Ratio
- Minimum state-of-charge (SOC_{min})

with three sets of experiments:

1. CD operation, Ratio = 1
2. CS operation, Ratio = 0
3. Mixed operation, 0 < Ratio < 1

In the CD operation experiment, the power duty cycle consisted of 5, 6, or 7 times a CD micro-cycle to reach an SOC_{min} of approximately 45, 35, or 25%, respectively. The cell was then charged using a CR of C/3, 3C/2, or 5 C to a voltage of 4.15 V, with a CV portion completing the charge to 95% SOC. The cycle was repeated for a total of 9 experiments, all conducted at 30 °C. For the CS experiment, the SOC was set by using the cell open circuit voltage (OCV) vs. SOC curve and a CS micro-cycle was repeated while keeping the voltage within a 10 mV window. A total of 3 experiments were conducted at 30 °C. For the mixed operation experiment, the power duty cycle consisted of 7 CD micro-cycles followed by CS micro-cycles in ratios of 1/2 and 1/4, with the cell charged using a CR of 3C/2. Four experiments were conducted, three at 10 °C, 30 °C, or 45 °C corresponding to a ratio of 1/2, and one at 30 °C corresponding to a ratio of 1/4. At the end of each experiment the charge throughput (Ah) was measured. Each cell was characterized before and after aging campaign by a capacity test and a hybrid power pulse characterization (HPPC) to assess discharge and regen power capability. Taking into account that the number of cycles is expressed as the total ampere-hour throughput [Ah] in both charge and discharge, the capacity fade was then expressed as:

$$S_{loss}(Ah) = 100 * \frac{S_0 - S\,(Ah)}{S_0}$$

with S_0 the cell nominal capacity and *S (Ah)* the cell capacity after Ah > 0 charge throughput. Therefore, the functional form adopted was:

$$S_{loss}\,(Ah) = f_C(SOC_{min}, Ratio, CR, T) * Ah^z$$

with f_C nonlinear function of the aging factors investigated and z > 0. Using the nonlinear optimization toolbox in Matlab, fitting parameters for each i-th experiment were defined. The expression following the characterization points obtained from tests resulted as:

$$S_{loss,i}\,(Ah) = f_{C,i} * Ah^{Z_i}$$

Results showed there was no significant dependence of capacity fade on CR. For this reason, CR was excluded from the model.

Regarding temperature, at high *T* capacity fade followed an Arrhenius relation so the following expression was adopted:

$$f_C(\bullet) = a_C(SOC_{min}, Ratio) * exp\left(\frac{-E_{a_c}}{R_g T}\right)$$

with cell activation energy for the capacity fade process E_{a_c} = 22406 [J mol^{-1}], R_g universal gas constant and *T* cell absolute temperature. An increase of temperature led to an increase of the capacity fade. Data from the temperature experiments are shown in ***Figure 24***.

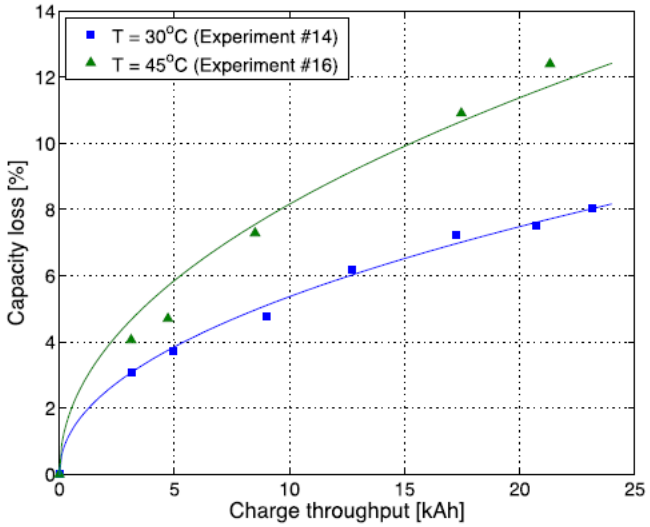

Figure 24 *Capacity loss for temperature experiments. Adapted and reprinted with permission from [13].*

Referring to the Ratio, the experimental severity factor values were fitted to the following equation:

$$a_C(SOC_{min} = 35\ \%, T = 30°C, Ratio) * \alpha_1 + \beta * (Ratio)^b$$

with identified constants α_1, β and *b* equal to 145, 420 and 0.34, respectively. ***Figure 25*** shows the function with the experimental data. Results show that the higher was the Ratio the higher was the capacity fade.

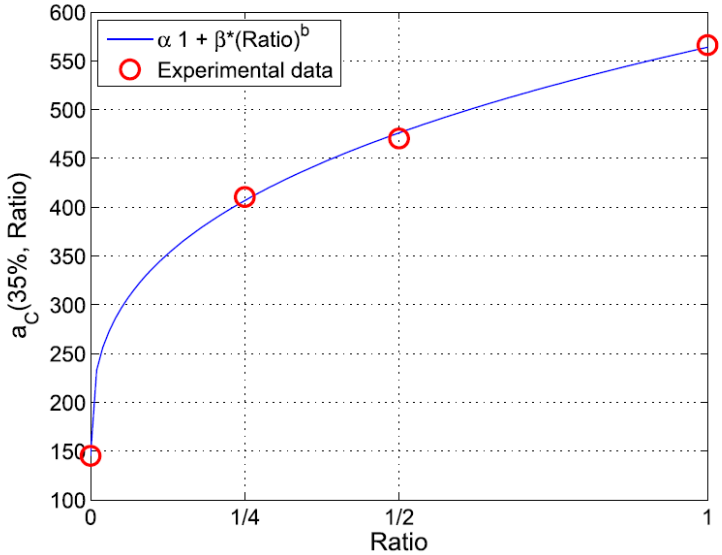

Figure 25 *Capacity severity function from Ratio experiments. Adapted and reprinted with permission from [13].*

For SOC_{min} the experimental severity factor values were fitted to the following equation:

$$a_C(Ratio = 0, T = 30°C, SOC_{min}) * \alpha_2 + \gamma * (SOC_{min} - SOC_0)^c$$

with identified constants α_2 and γ equal to 137 and 9610, respectively, for SOC_0 = 0.25 and *c* = 3. ***Figure 26*** shows the function with the experimental data.

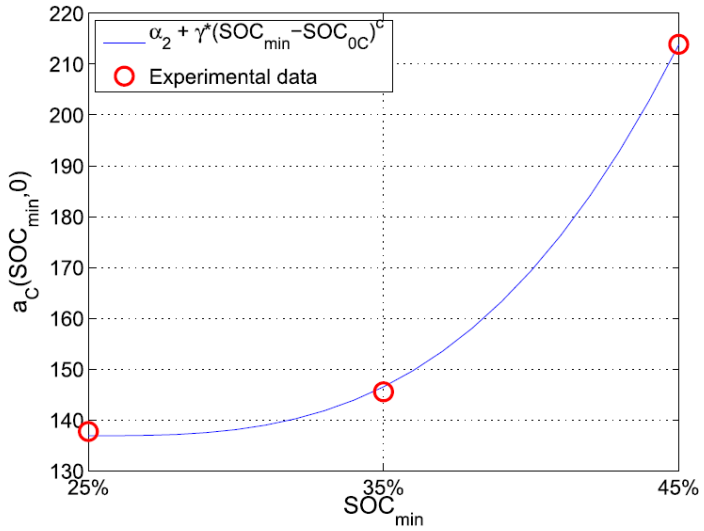

Figure 26 *Capacity severity function from SOC_{min}experiments. Adapted and reprinted with permission from [13].*

Results showed an increase in capacity fade with an increase of SOC_{min}.
Capacity fade was finally described by:

$$S_{loss}\,(Ah) = a_C(SOC_{min}, Ratio, T) * \; exp\left(\frac{-E_{a_c}}{R_g T}\right) * Ah^z$$

with $a_C(\bullet)$ given by:

$$a_C(\bullet) = \alpha_C + \beta_C * (Ratio)^b + \gamma_C * (SOC_{min} - SOC_0)^c$$

Results from the experiments validated the model. Moreover, the goodness of the model was evaluated through the root mean square (RMS) error with a result of 0.0047%.

Design-of-experiment and statistical modeling of a large scale aging experiment for two popular lithium ion cell chemistries

About large-scale aging experiment which involves tens of cells subjected to aging conditioning, Pouch cells of two different chemistries were analyzed with the aim of DoE approach. More specifically: 99 constituted by iron-phosphate cathodes and graphite anodes (LFP cells) with initial capacity of 50 mAh and 78 made of nickel-aluminium-cobalt-oxide cathodes and graphite anodes (NCA cells) with initial capacity of 60 mAh. Prochazka *et al.* conducted a 5-steps DoE which consisted in: i) statement of experimental target; ii) screening and test plan conception; iii) test plan reduction; iv) conduction of the experiment; v) analysis of the results [14]. For the first step, cell capacity decrease and impedance increase were selected as target values. The aim was to prolong as much as possible the time until the end-of-life criterion for one of the target values is reached. Capacity decrease limit was set to 60% of remaining capacity and 300% was the limit for impedance increase. The second step consisted in defining the range of external influence factors. Design factors were extrapolated from literature. As shown in ***Figure 27***, controllable factors and a full-factorial test plan were defined.

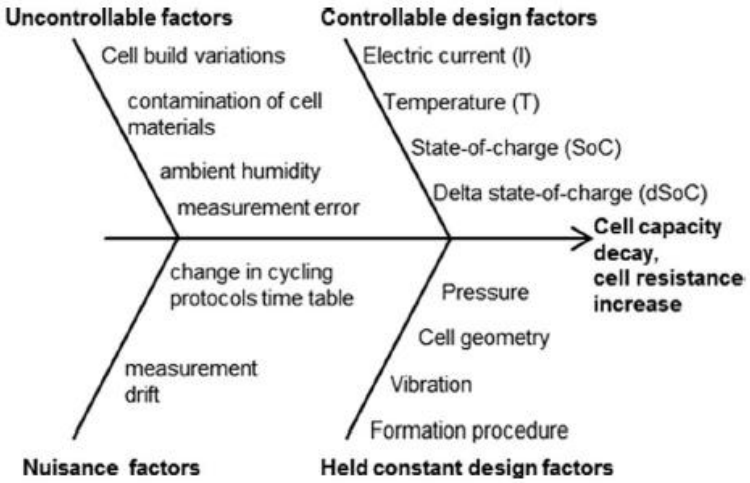

Figure 27 *Fishbone-diagram of the identified causes effecting aging and its measurement in lithium-ion cells. Electric current, temperature, state-of-charge and delta stage of charge were selected as design factors. The uncontrollable factors were taken into account to define the repetitions of each test to obtain statistically valid results. Assuming five setting levels, 4^5 possible sample points were defined. According to cell physics, some interactions among design factors were eliminated and the final sample points became $3*(4^5-230)$. Adapted and reprinted with permission from [14].*

Third step consisted in reduction of the test plan by using a modular algorithm for the design of large scale D-optimal experiments. The algorithm selected a set of points in the corners and others randomly distributed in the test space. Then in each optimization step another random point out of the full factorial test plan was exchanged with one of the initially selected points and, if the calculated change in D-optimality increased, the change was kept. The process was carried forward until no more increase in D-optimality was found. In this way the test plan was reduced to 46 sample points. The fourth step was the conduction of the experiment itself according to a reference test procedure (RTP). Results showed that for both chemistries (LFP and NCA cells) there was a strong dependency of the capacity decrease on the temperature. About the impedance increase, for new cells when applied temperature was below 10 °C the effect was more evident with respect to temperature above 30 °C. With aged LFP and NCA cells this effect was less significant. The last step in DoE process was modeling and analysis. Each of the two target values (capacity decrease and impedance increase) were treated in separate models as for the considered chemistries. The deduced characteristics of the aging paths for the two chemistries are shown in ***Figure 28***.

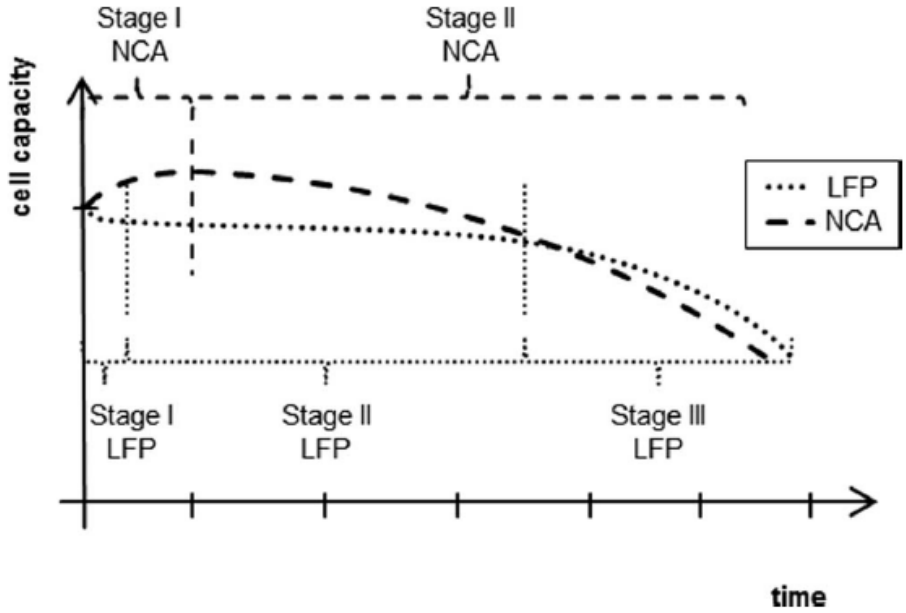

Figure 28 *LFP and NCA deduced aging paths of the target parameter cell capacity. The two paths can be divided into different stages according to different behaviors. Adapted and reprinted with permission from [14].*

About the design factors, dSoC was found to enhance NCA aging when high. SoC showed very different results: for NCA cells low average SoCs were favorable for a low capacity decrease and impedance increase, while for LFP it was found that a high SoC was preferable. The interaction of dSoC and SoC was more notable for NCA cells where high values of SoC and large dSoC caused particle destruction and accelerated aging process. For LFP this interaction was not relevant. The interaction of current and dSoC was remarkable in LFP impedance increase. This was not relevant for NCA cells. About current and SoC interactions, for both chemistries large value of current applied to empty cells led to low aging, while large current applied to full charged cells emphasized aging effect. Interaction between current and temperature had shown that local heating due to high current had less impact when temperatures were already high and impedance low. For LFP cells this interaction was not relevant.

D-optimal design of experiments applied to lithium battery for ageing model calibration

Battery ageing models act a really important role in applications where management strategies are critical to limit degradation. Lithium batteries suffer of solid-electrolyte-interphase (SEI) and lithium plating at the negative electrode but also the intercalation of lithium ions can cause volume changes in both electrodes generating particle cracking and loss of electrical contact. Battery ageing models can be divided into two groups: i) physico-chemical approach; ii) semi-empirical approach. The first one uses chemical reaction kinetics and physical equations, while the second is based on ageing tests and mathematical fitting. Mathieu *et al.* applied a D-optimal design of experiment in order to further optimize the initial design of a battery capacity ageing model. Calendar and cycling tests were used to calibrate the model, and the dependence of the degradation rate on temperature, SoC and current was thoroughly modelled [15]. From literature, Dakin showed that the dependence of the degradation rate of insulating material tensile strength on temperature was well described by Arrhenius law. Then Baghdadi demonstrated the theory was extendable to SoC and current in accordance with the following equation:

$$k_c(T, SoC, I) = A\left[\exp\left(\frac{-b}{T}\right)\exp(cSoC)\exp\big(a(T)\big)\,I\right]$$

Applying the principles of DoE and considering the exponential expression above, the studied response became ln(k_c). For cycling experiments, three levels of temperature (0, 25 and 45 °C), four levels of SoC (30, 65, 80 and 90%) and two levels of charge/discharge current magnitude (C/3 and 1C) were considered. Current values were chosen with the aim of including economical and aggressive vehicle drive style. The pre-specified model adopted included linear effects of the three factors and two interaction effects: i) temperature and SoC to consider SEI growth; ii) temperature and charging current for lithium plating effect. Standardized values obtained by the software after estimation are represented in ***Figure 29***.

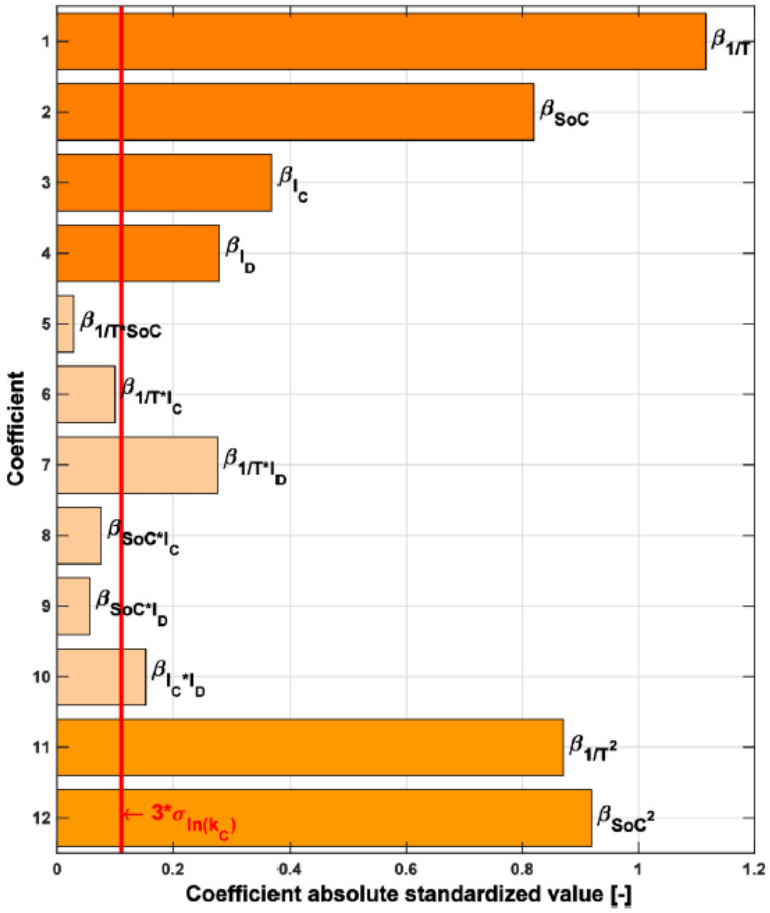

Figure 29 *Estimation of $l_n(k_C)$ model coefficients for 1/T and SoC initial quadratic model, with all linear and first order interaction effects. An arbitrary cutoff, indicated with red line, was considered as 3 times the mean standard deviation of the response $l_n(k_C)$. The model was then reduced in terms of considered effects taking into account all quadratic and linear effects and $1/T*I_C$ and $1/T*I_D$ interactions. Adapted and reprinted with permission from [15].*

The final model consisted in 9 parameters, including intercept β_0. The capacity fade computed with Matlab function *regstats* showed an absolute relative error of 0.85% with respect to experimental data. The fit was evaluated as satisfactory for both calendar and cycling data.

Experimental assessment of battery cycle life within the SIMSTOCK research program

SIMSTOCK program was set up within the French context among cars manufacturers, suppliers and research labs to share costs and efforts to go forward in the studying of the energy storage system (ESS) ageing.

The first step was to create a battery model. Open circuit voltage (OCV), which represents the voltage of the battery at its thermodynamical equilibrium, the voltage drop η_{CT} (named also overpotential or overvoltage) caused by the charge transfer, diffusion η_{diff} and ohmic losses η_{Ω} were the parameters used to determine the model:

$$U = OCV - \eta_{tot} = OCV - \eta_{CT} - \eta_{diff} - \eta_{\Omega}$$

An equivalent electrical circuit, schematized in ***Figure 30***, was defined to describe the mentioned phenomena.

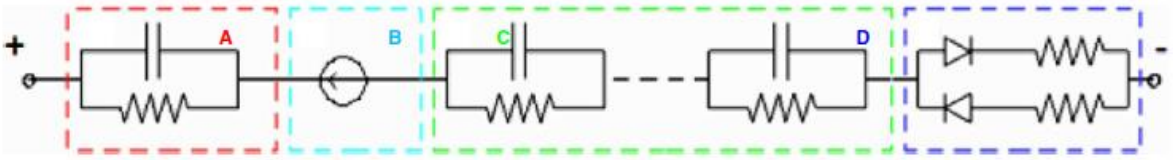

Figure 30 *Battery equivalent electrical circuit: charge transfer is represented by a parallel RC circuit (A); OCV is represented by the voltage source (B); diffusion by n serial RC parallel circuits (C); ohmic losses by the parallel resistances (D). Adapted and reprinted with permission from [16].*

A parameter identification assistant tool was developed to compute each model parameter under various conditions of SOC and current at different temperatures. Then a protocol was used at the beginning of life and at a regular period of time to estimate the battery capacity decrease and impedance increase. In particular, this consisted in the measure of each cell's capacity, electrochemical impedance spectroscopy and the voltage response to current pulses at different SOC. Finally, a database for all parameters was completed. At this point DoE became necessary to determine the ageing laws for each parameter. Ageing was express as the useful capacity representative of the SOC range where performances are met. Current, temperature, Ah throughput and SOC variations were the selected parameters for each of them, a min and a max were selected. At least 11 tests were necessary to derive the coefficient of the simplified polynomial expression of the ageing. ***Figure 31*** shows the capacity evolution *vs.* time: a sharp drop is highlighted, with a greater fade for the testing condition with the highest current and Ah throughput. A differential approach was adopted since the ageing conditions were subjected to change in a usage vehicles scenario.

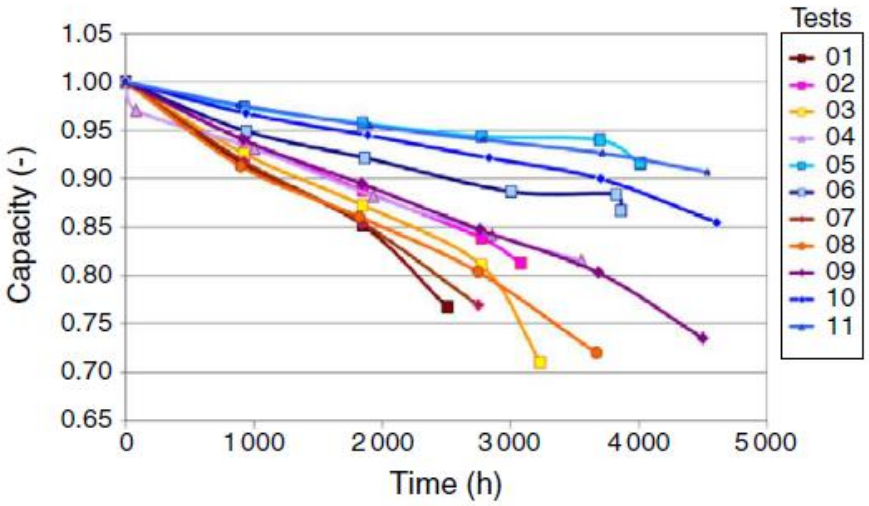

Figure 31 *Measured capacity fade vs. time. Adapted and reprinted with permission from [16].*

The analysis of the coefficients stabilized that temperature had the strongest effect, followed by the Ah throughput and then current. The final step was to implement the results of the measurements into a model to forecast the capacity fade and resistance increase during the vehicle life. Once the simulation scheme of the hybrid vehicle had been defined, the results were compared as shown in ***Figure 32***.

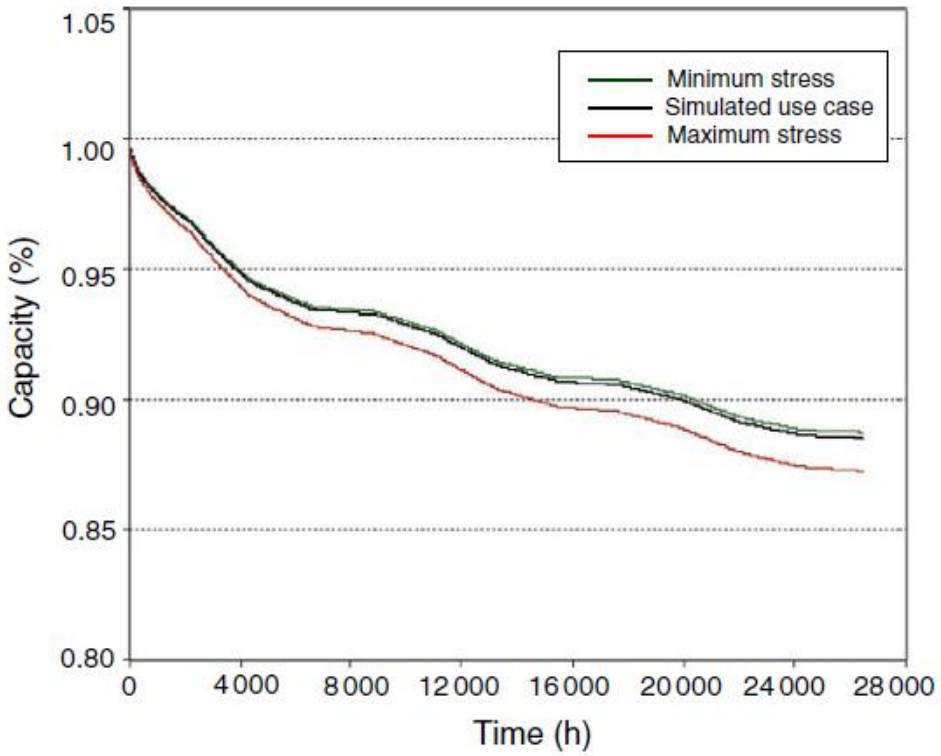

Figure 32 *Evaluation of a battery capacity fade on a HEV. The actual case is very close to the minimum stress. Adapted and reprinted with permission from [16].*

Experimental investigation of the effect of C-rate, electrode gaps, and electrode surface roughness on the performance characterization of lead-acid batteries

Lead-acid batteries (LABs) are appreciated for their capability to work at high voltages, acceptable specific energy and for working at a wide range of temperatures but also for their predisposition to be recycled. Within this typology, flooded lead-acid batteries (FLABs) are the most widely used. During the process of charge and discharge the electrochemical reactions cause a sharp increase of the temperature rise (TR) rate and consequently of the C-rate. This is always followed by a decrease in their capacity, which may cause damages to the battery. For this reason, a DoE was adopted by Saeed Nahidi *et al.* to investigate the effect of three parameters on the capacity and the TR rate [17]. These parameters are: i) electrode gaps; ii) roughness quality of electrode surfaces; iii) C-rate. Two methods were applied: the central composite design (CCD) and the response surface method (RSM). 20 tests (20 charging and 20 discharging tests) were designed by the software, each one composed of a combination of different values related to independent variables. The FLAB cells were prepared for the tests with different electrode gaps from 2 to 10 mm and different roughness of the electrode surfaces. After the preparation of the cells, each of them was fully discharged to the lower voltage limit and rested. Results are shown in ***Figure 33***.

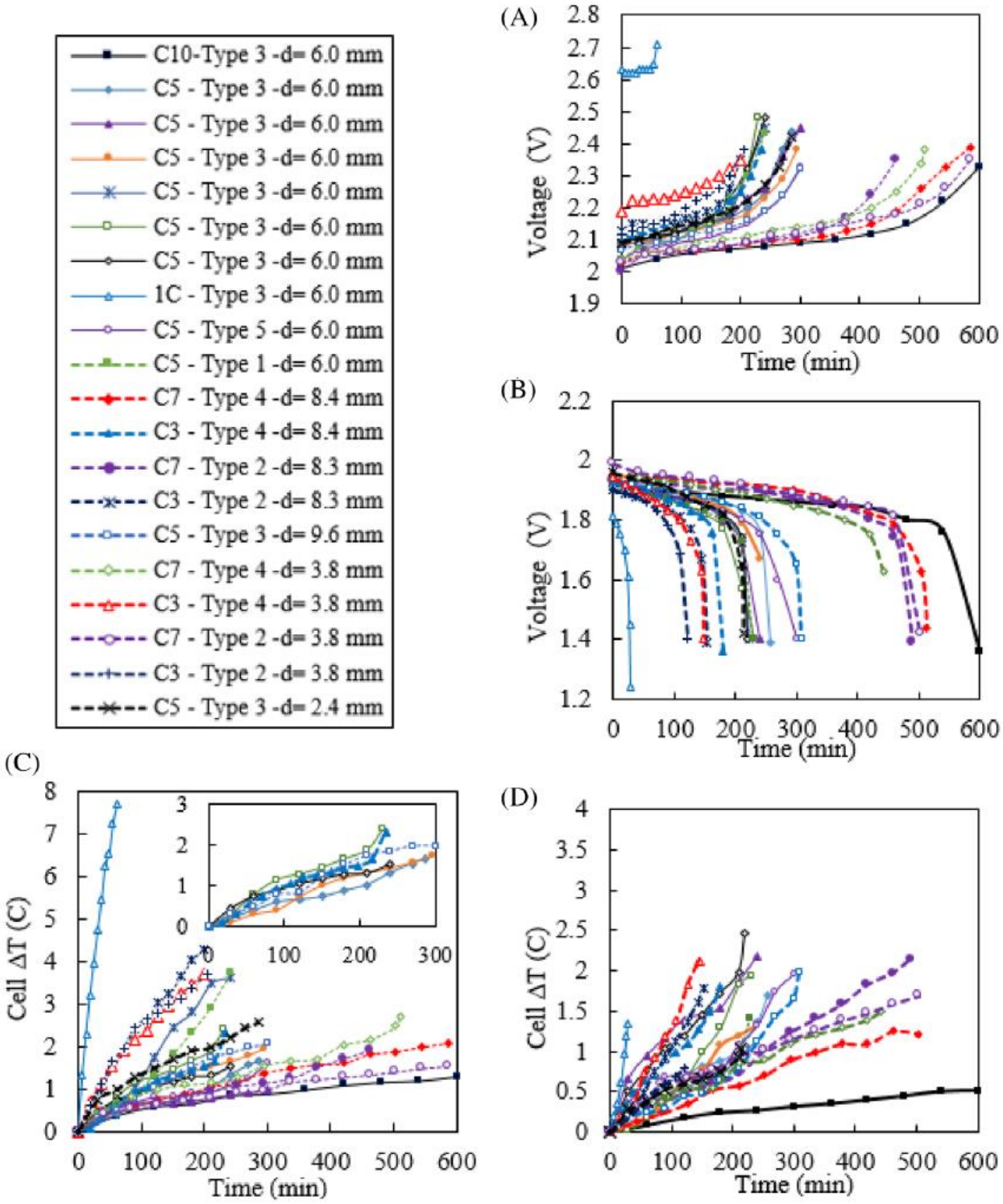

Figure 33 *The voltage of FLAB cells during (A) charging and (B) discharging processes and average ΔT of flooded lead-acid battery (FLAB) cells during (C) charging and (D) discharging processes at different modes. Adapted and reprinted with permission from [17].*

For the RSM a quadratic relation was defined to describe the relationship between the response and the variables. Capacity and TR rate of the FLABS were calculated by measuring the voltage and temperature of the cells during the tests. The data were defined by a power function as follows:

$\sigma = f(\mu^{\alpha})$;

with σ the standard deviation (SD), μ the mean and α the power.

For the evaluation of the adequacy of the proposed model, adjusted and predicted R^2, adequate precision and predicted residual sum of squares (PRESS) were calculated. The PRESS number indicates how much a model can fit with any design point. In both the models the difference between adequate and predicted R^2 was less than 0.2. In order to achieve the highest capacity with the lowest TR rate the optimization processes were performed according to the models generated by Design-Expert software. The maximum capacity achieved was 15.72 Ah and the minimum TR rate was 0.003. These results were obtained with a gap between electrodes of 8 mm and electrode surface roughness of λ = 2.5 mm.

Investigation and modeling of cyclic aging using a design of experiment with automotive grade lithium-ion cells

In the automotive context it is important to understand the effect of different operating conditions on degradation of batteries. More in detail, cyclic aging is more complex in comparison with calendar aging. Moreover, experiments for lifetime modelling of the batteries are very expensive and have a duration of years. In this regard, DoE becomes fundamental. Stadler *et al.* carried out a test matrix based on 62 automotive grade Li-ion cells with a planned real-world operating cycling [18]. A 63 Ah nominal capacity cells were used, all with a starting state of charge of 75%. 5 main aging factors were defined according to the literature: i) temperature; ii) SoC_{min}; iii) SoC_{max}; iv) charging power P_{CH}; v) the ratio of energy throughput between micro and macro-cycles (EV_{ratio}). A central composite design (CCD) was used with 5 factors and 2 levels. The cells were tested among 27 different variations according to the CCD for a time longer than 2 years. The cycling sequences were divided in 3 phases as follows: i) Phase I consisted in a charge at constant-power-constant-voltage protocol (CPCV); ii) Phase II consisted in a discharge to SoC_{min} with a charge depleting EV driving profile; iii) Phase III involved a charge from SoC_{min} to SoC_{max} with a HEV performance profile. HEV and EV profiles were derived from real usage. The three phases were repeated for 14 days. A regression model with second-order terms was defined because of its accuracy in approximating measurement data. By the use of a stepwise backwards selection, the terms with a p-value bigger than 0.1 were automatically removed because statistically insignificant. Firstly, a single regression model was created to describe capacity loss at 175 kAh. About the influence of temperature, as showed in ***Figure 34***, the lowest aging was observed at 31 °C and both an increase (to 50 °C) and a decrease (to 11 °C) in temperature led to an acceleration in aging. Referring to the charging power, a slight increase in aging was observed moving from a charging power value of 136 W to 264 W but it was a small effect. The upper SoC limit had a strong effect on aging. It was observed a strong acceleration in aging with SoC values over 90%. Even a greater value of lower SoC exacerbated the capacity degradation of the batteries. Lastly, the EV ratio had the greatest impact on cycling aging. The explanation was that with higher ratio of EV-cycles the cell is charged more frequently and so more charge throughput is accumulated. The active materials were solicited more and particle cracking, SEI cracking and contact loss of particles occurred more frequently. About the interactions, six of them were defined as relevant as showed in ***Figure 35***. In particular, the term related to SoC_{max} : SoC_{min} had the strongest effect on capacity loss.

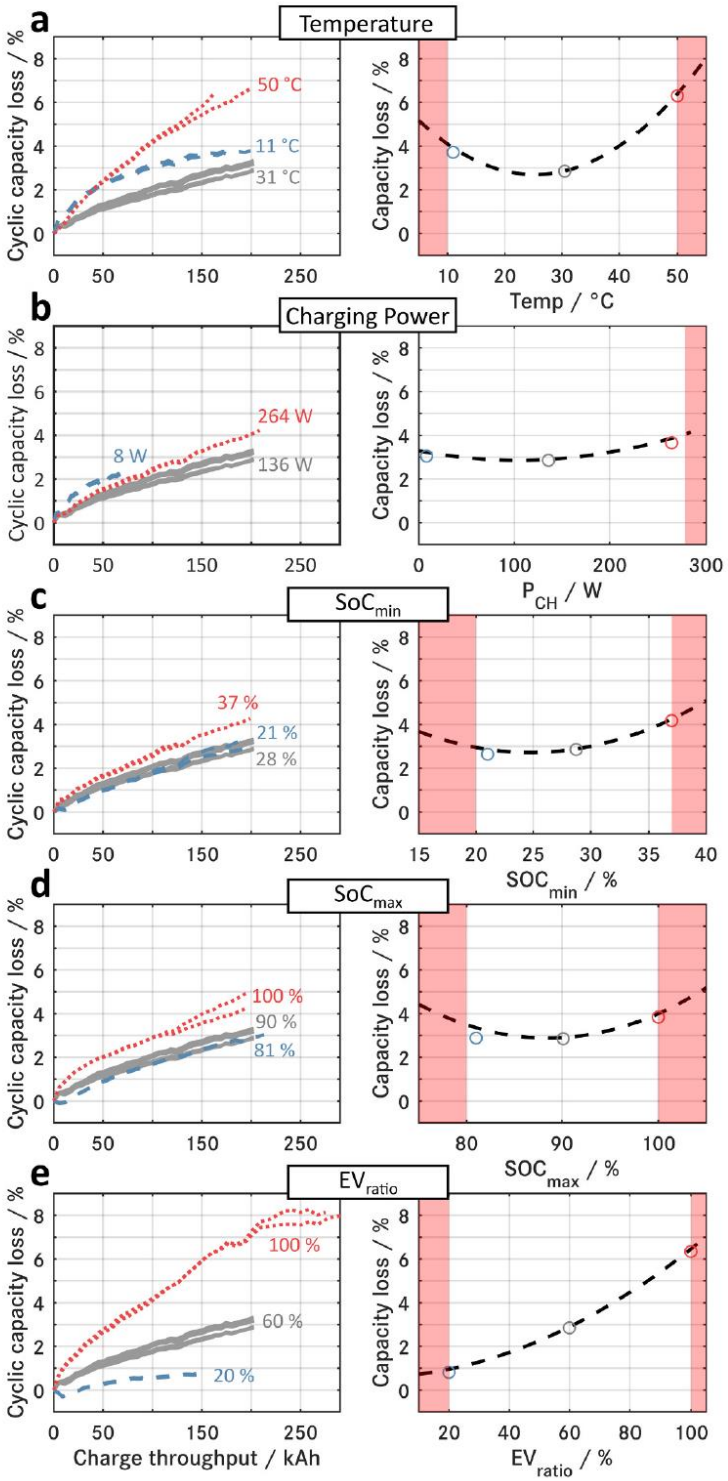

Figure 34 *Relative capacity loss due to cyclic aging related to the five factors (on left). Modelled aging behavior (dashed line) and measured relative cyclic capacity loss (on right). Adapted and reprinted with permission from [18].*

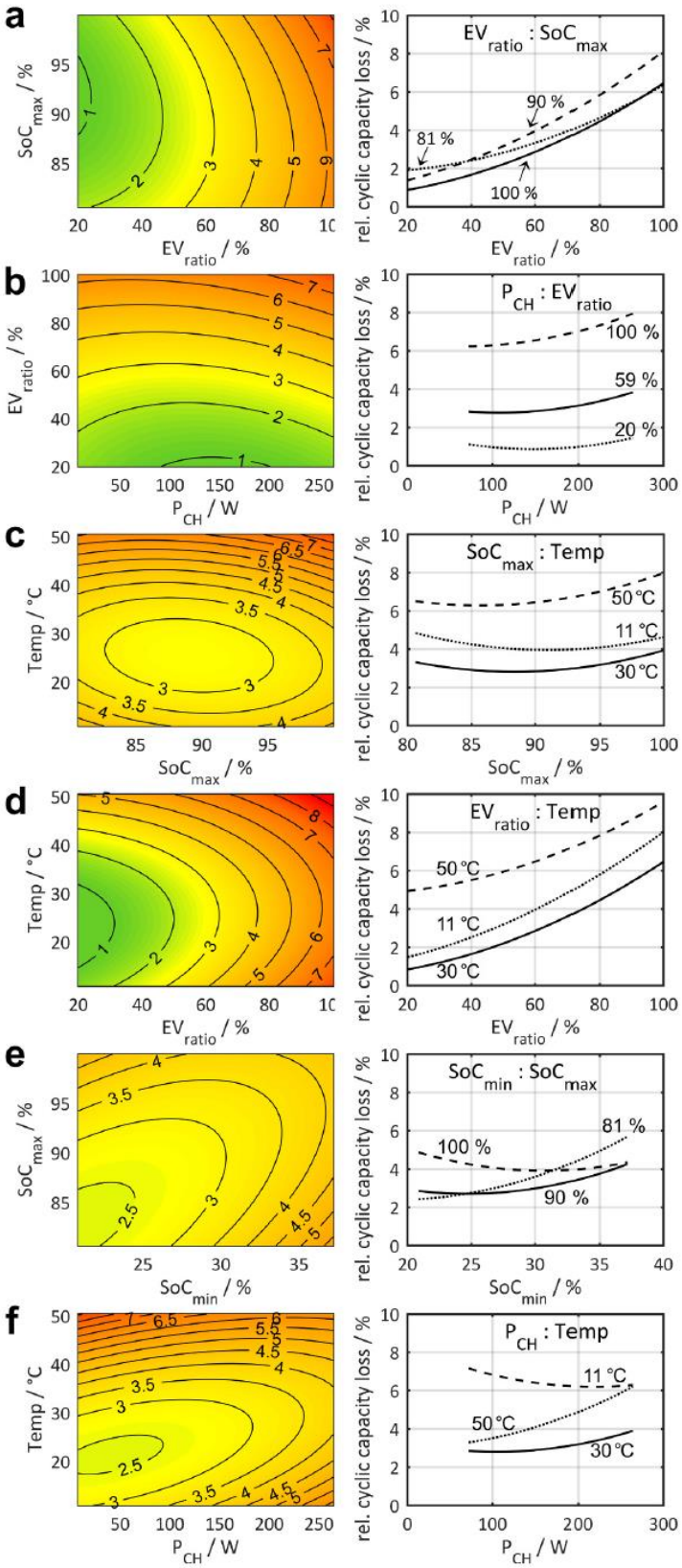

Figure 35 *Cycle capacity loss in % after 175 kAh related to two factors (on left). Projection of cyclic capacity loss after 175 kAh related to one factor at three different levels of the second factor: where the curves differ from a parallel course it means more interactions between factors. Adapted and reprinted with permission from [18].*

Investigation of the influence of superimposed AC current on lithium-ion battery aging using statistical design of experiments

The experimental design and analysis can also be used to study factors that impact battery aging. The aging process of lithium-ion batteries (LIBs) is a significant research topic due to the impact on battery cycling life and associated vehicle warranty issues [3]. A quantitative analysis is provided to determine the aging effect of the root mean square (RMS) current factor, which can be useful for designing battery pack filters using direct current (DC) bus capacitors. The growth of a solid-electrolyte interface layer can increase resistance and lead to capacity loss and power fade. Many studies have been conducted to determine the aging performance of LIBs under various conditions [3], including calendar life models and cycling conditions. Factors that may influence battery aging are temperature, end-of-discharge voltage, charging voltage and the superimposed alternating current (AC) component of the battery. The AC component of the battery has been proposed as a factor in battery aging [3], but more research is needed to determine its significance. To reduce the AC component of the discharge current, passive filtering or other methods may be necessary. The design of the DC bus filter in electric vehicle power electronics, which filters the AC component from the battery pack, could be impacted by the role of the AC component in battery aging. A first experiment was conducted by Larry W. Juang *et al.* using 16 ICR14500NM cells, which were operated at 760 mAh, 4.2 V constant voltage charging limit, 2.8 V fully discharged cut-off voltage and 300 charge/discharge cycles [3]. The cells were charged at a constant current rate of 800 mA to 4.2 V and were discharged using a feedback circuit that synthesized various AC discharge current waveforms and implemented electrochemical impedance spectroscopy (EIS) in the presence of a DC current offset. The cells were placed in a heat chamber throughout the experiments to maintain a constant temperature of 30 °C. The goal of the first experiment was to determine the impact of a superimposed AC component on the cell aging characteristics. Among a total of 16 cells, for 8 of them the AC component was added to the DC discharge current, so the RMS value of the total discharge current waveform was 905 mA (AC-905), while for treatments DC-800 and DC-905 4 cells were used, as detailed in ***Table 3***.

Table 3 *Treatments summary for the first experiment.*

Treatment designation	Waveform (mA)	RMS (mA)	DC (mA)	AC (mA)
AC-905	I = 600 sin (2π20 t) + 800	905	800	600 sin (2π20 t)
DC-800	I = 800	800	800	0
DC-905	I = 905	905	905	0

The focus of the study was on the battery aging as determined by changes in its series resistance value, which was interpolated from the EIS results. The battery was cycled 300 times, with the reference performance tests (RPTs) performed at the beginning and every 30 cycles.

The statistical method consists in the definition of a normalized cycle number $Z = \frac{\mathrm{C}-\overline{\mathrm{C}}}{\Delta \mathrm{C}}$, where *C* is the cycle number, $\bar{C}$ the average value of all the cycle numbers and ΔC = 30 cycles. The equation of the model is the following:

$$R_{ij} = \hat{\beta}_0 + \hat{\beta}_1 R_{i0} + \hat{\beta}_2 X_{1j} + \ldots + \hat{\beta}_{17} X_{16j} + \varepsilon_{ij} ,$$

with

$$X_{kj} = Z_j \delta(i-k)$$

$$Z_j = \frac{C_j - \overline{\mathrm{C}}}{\Delta \mathrm{C}}$$

R_{ij} is the resistance of the i^{th} battery cell for the j^{th} EIS measurement, R_{i0} is the initial resistance measurement of the i^{th} battery cell, X_{kj} the resistance predictor value for the k^{th} and j^{th} measurements, δ the Kronecker delta function and ε_{ij} the error unaccounted. For each battery cell, an estimated slope was determined. Moreover, for each group an average estimated slope and its variance were defined as follows:

$$\hat{\beta}_{avg} = \sum \frac{\hat{\beta}_i}{\mathrm{n}}$$

$$Var(\hat{\beta}_{avg}) = \frac{Var(\hat{\beta}_i)}{n}$$

The null hypothesis, or the statement being tested, was that the groups cell ages at the same rate. The t-statistic, with its degrees of freedom, was used to calculate the p-value, which is a measure of the strength of evidence against the null hypothesis.

t-statistic formula (following Student's distribution) was defined as follows:

$$t = \frac{\hat{\beta}_{avg1} \qquad 1 - \hat{\beta}_{avg2}}{\sqrt{Var(\hat{\beta}_{avg1}) + Var(\hat{\beta}_{avg2})}}$$

If the p-value is small, typically 5% or less, the null hypothesis is rejected. This means that the mean estimated resistance slope (a measure of aging rate) for the two test treatments being compared is statistically different. If the p-value is larger, it means there is not enough evidence to reject the null hypothesis and the two test treatments are assumed to have statistically similar mean estimated resistance slopes and therefore similar rates of aging. The t-statistic and p-values for the group comparisons were listed in ***Table 4*** and ***Table 5*** for 0% and 100% state of charge (SOC) conditions, respectively.

Table 4 *t-statistics and p-values for the O% SOC condition in the first experiment.*

Treatment comparisons	t-statistic	p-value (%)	Rate of aging for two treatments
AC-905 vs. DC-800	1.91	5.81	Different
DC-905 vs. DC-800	2.01	4.63	Different
AC-905 vs. DC-905	0.41	68.24	Similar

Table 5 *t-statistics and p-values for the 100% SOC condition in the first experiment.*

Treatment comparisons	t -statistic	p- value (%)	Rate of aging for two treatments
AC-905 vs. DC-800	1.84	6.79	Different
DC-905 vs. DC-800	1.44	15.21	Different
AC-905 vs. DC-905	0.17	86.53	Similar

The results showed that the AC-905 and DC-905 groups (same RMS current) had approximately the same aging rate, while the DC-800 group (different RMS current) had a noticeably different aging rate. It was also found that the difference in depth of discharge (DOD) between treatments was not significant, supporting the conclusion that RMS current affects aging, but DC offset current alone does not.

A second experiment was performed to confirm the influence of RMS value on battery aging, to investigate the possible influence of AC current waveform shape and frequency on aging. The experiment was conducted using the same schedule of the first one but using 4 treatments as shown in ***Table 6.***

Table 6 *Treatment summaries for the second experiment.*

Treatment designation	Waveform (mA)	RMS(mA)	DC (mA)	AC (mA)
S-807-20Hz	800+ 105*sqrt (20 Hz)	807	800	105*sqrt (20 Hz)
S-807-1000 Hz	800+ 105*sqrt (1000 Hz)	807	800	105*sqrt (1000 Hz)
S-703-20Hz	695 + 105*sqrt (20 Hz)	703	695	105*sqrt (20 Hz)
S-70.3-1000 Hz	695 + 105*sqrt (1000 Hz)	703	695	105*sqrt (1000 Hz)

The model is defined as follows:

$$R_{ij} = \hat{\beta}_0 + \hat{\beta}_1 R_{i0} + \hat{\beta}_2 X_{1j} + \ldots + \hat{\beta}_{32} X_{31j} + \varepsilon_{ij}$$

because of the use of the data collected in the first experiment.

Results showed that there is no correlation influence of frequency or the shape of the current waveform on battery aging and that RMS current influences aging while DC current alone does not. It is also showed that the resistance of the batteries increased faster for higher RMS cases.

Overall, the results of these experiments suggest that the RMS value of the discharge current waveform is the most important factor contributing to battery aging.

Lithium-ion battery ageing assessment based on a reduced design of experiments

On-board energy and power capability of lithium batteries decreases over time due to various mechanisms such as cracking or dissolution of the active material and growth of the solid electrolyte interphase. The rate of these mechanisms is dependent on operating conditions like temperature, state of charge, voltage, depth of discharge, and current magnitude. Developing a global battery aging model that considers all these factors and unifies calendar and power cycling operation is difficult and time-consuming. Issam Baghdadi *et al.* investigated the sensitivity of battery capacity to aging rate at different temperatures, currents, and states of charge [19]. A reduced DoE was proposed to determine the 27 degradation rates resulting from 27 different conditions which were: i) 3 ambient temperatures of 0, 25 and 60 °C; ii) 3 SOCs of 30, 60 and 90%; iii) 3 current levels of 0, 1 and 3 C. Thanks to DoE only 9 different battery cells were used in less than 100 days of tests. The simplifying hypotheses were based on the cumulative damage theory developed by Palmgren-Miner, which defines that damages occurring under several aging events are additive and the degradation associated to one event is not influenced by other previous events. The validity of this hypothesis was assumed in this study. The Dakin's degradation equation was used to determine battery aging rates for each condition:

$$\frac{d\xi}{dt^{\alpha\xi}} = \pm k_\xi \, \xi^{n\xi}$$

with t aging time, $\alpha\xi$ time dependent factor, k_ξ degradation rate of ξ, $n\xi$ the reaction order of the aging reaction. $\alpha\xi$ and $n\xi$ were assumed equal to 1 according to previous studies [19]. By the integration and then the derivative over aging it was possible to determine the degradation rate k_ξ as follows:

$$\pm \frac{d(\ln(\frac{\xi(t)}{\xi_0})}{dt} = k_\xi$$

with ξ_0 the parameter at beginning of life (BOL).

The battery model which was used for the experiments was a commercial lithium polymer battery with a capacity of 12 Ah and cutoff voltages of 4.2 and 2.7 V. 9 aging tests were performed and each battery was aged under one temperature and one current level among the defined values around 3 different average SOCs. The experimental protocol consisted in 3 parts: i) checkup; ii) setting cell SOC; iii) power cycling. Initial checkups were performed for each cell at the BOL to determine their starting aging point. Then, two checkups were performed for each SOC spaced 15 days apart, with the period being shortened or extended for extreme aging conditions. The experiment consisted of 7 checkups. The aging rates were calculated for each aging condition (temperature, current, SOC) using 3 checkups out of the 7 performed. After each checkup, the test temperature was stabilized for 3 h, and the aging SOC was set at the ambient test temperature. The cells underwent power cycling, which involves charging and discharging pulses spaced by 10 s of rest. The cycling was performed around the average SOC with a ±5% ΔSOC range. The evolution of battery capacity (Q) overtime was defined as follows:

$$Q(t) = Q(t_0)\, x \exp(-k_Q t)$$

with $Q(t_0)$ the battery capacity at BOL and k_Q the battery capacity degradation rate as function of T_{amb}, SOC and current and identified by linear fitting.

Fitting results using Dakin's degradation equation are represented in ***Figure 36***. The highest degradation occurred at 0 °C and max current magnitude (36 A).

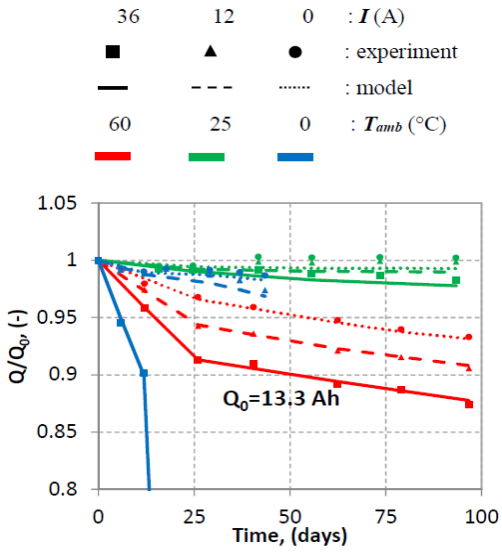

Figure 36 *Fitting results using Dakin's degradation equation with variable aging conditions and the determined aging rates. Adapted and reprinted with permission from [19].*

A polynomial function of $\ln(k_Q)$ depending on the aging factors was defined considering linear effects, first order interactions and quadratic effects as follows:

$$\ln(k_Q) = a_0 + \sum_{i=1}^{3} a_i X_i + \sum_{i,j=1\, i\neq j}^{3} a_{ij} X_i X_j + \sum_{i=1}^{3} a_{ii} X_i^2$$

Figure 37 represents battery capacity aging rate surfaces as a function of $1/T$ and SOC.

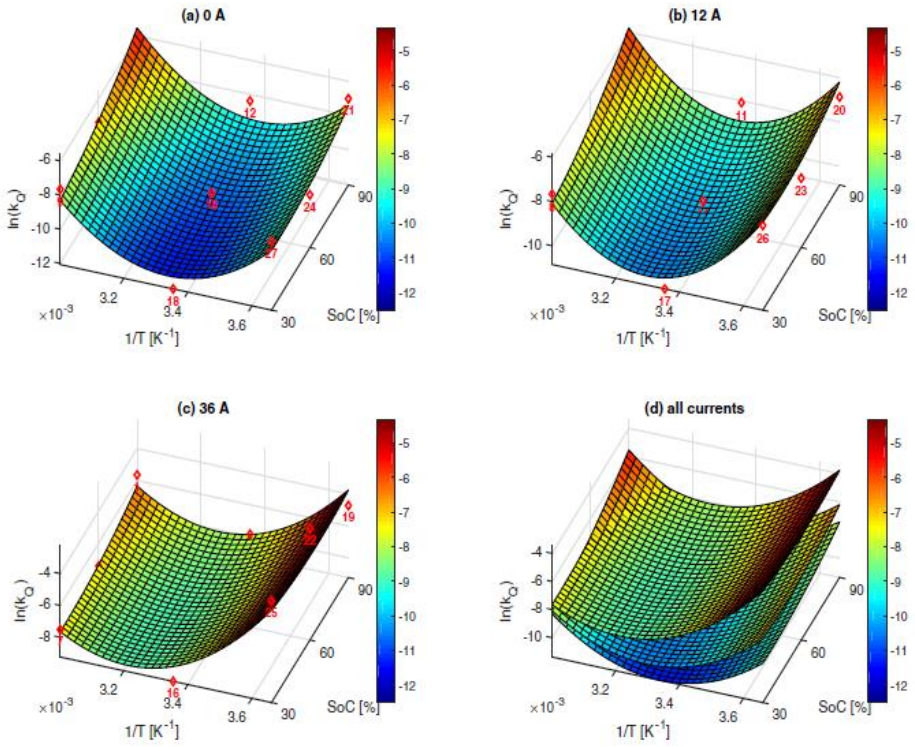

Figure 37 *Battery capacity aging surfaces as a function of 1/T and SOC. Adapted and reprinted with permission from [19].*

The results of the study show that the battery capacity degradation rate is a function of the operating test conditions and that the degradation rates are linear in the logarithmic scale. The results also show that the average of the available regression factors R^2 for degradation rate identification is 0.937, indicating a fair approximation of the linearity of the aging rates. The results show that the proposed model is a valid tool for predicting battery aging rates and for optimizing the battery usage strategies to extend the system lifetime.

Model based condition monitoring in lithium-ion batteries

There are several factors causing faults in the Li-ion batteries that can be linked to structural or thermal failures but also to a combination of manufacturing defects, over charge/discharge and short circuits. A way to study the behavior of Li-ion batteries is to create a model of them. The equivalent circuit model is very appreciated because it allows a good representation of cell dynamics with low computational resource usage. The equivalent circuit is shown in ***Figure 38***.

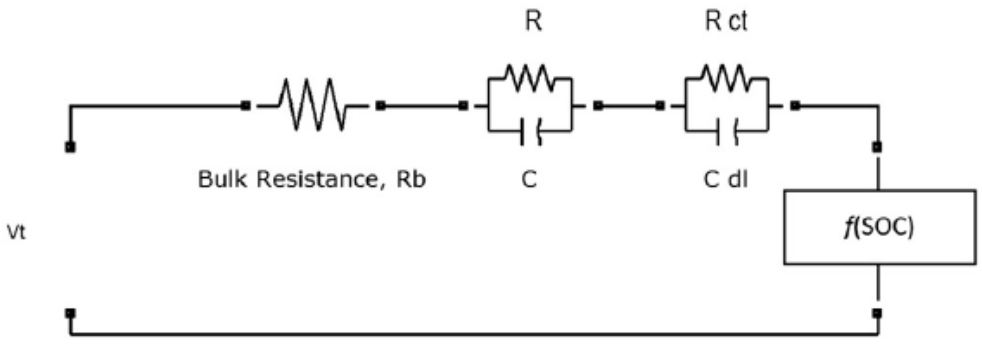

Figure 38 *Li-ion battery equivalent circuit model. R_b is the ohmic resistance representing the limited conductance of metallic contacts, inter cell connections, electrode material and the bulk electrolytic resistance to electron and ion migration. Constant phase*

element C and resistance R represent the distribution of reactivity associated to the property of the electrode. Finally, charge transfer resistance R_{ct} and double layer capacitance C_{dl} represent the interfacial impedance of the cell and V_{OCV} the battery cell OCV. Adapted and reprinted with permission from [20].

The *f(SOC)* was defined as the non-linear function that relates the OCV with the SOC of the battery. The experimental OCV-SOC curve is shown in ***Figure 39*** and it was modelled with a ninth degree polynomial. Considering the complexity of the process, the cost and the range of operation, Singh *et al.* applied a model-based fault diagnosis with Kalman filter as observer filter which worked in parallel with the battery and by measuring the load/charge current and the terminal voltage estimated the states of the battery model. For non-linear process models the Kalman filter was substituted with the extended Kalman filter. Furthermore, the single observer was extended to a series of observers. In this way each observer represented a particular fault/operational condition allowing for a robust Li-ion battery monitoring.

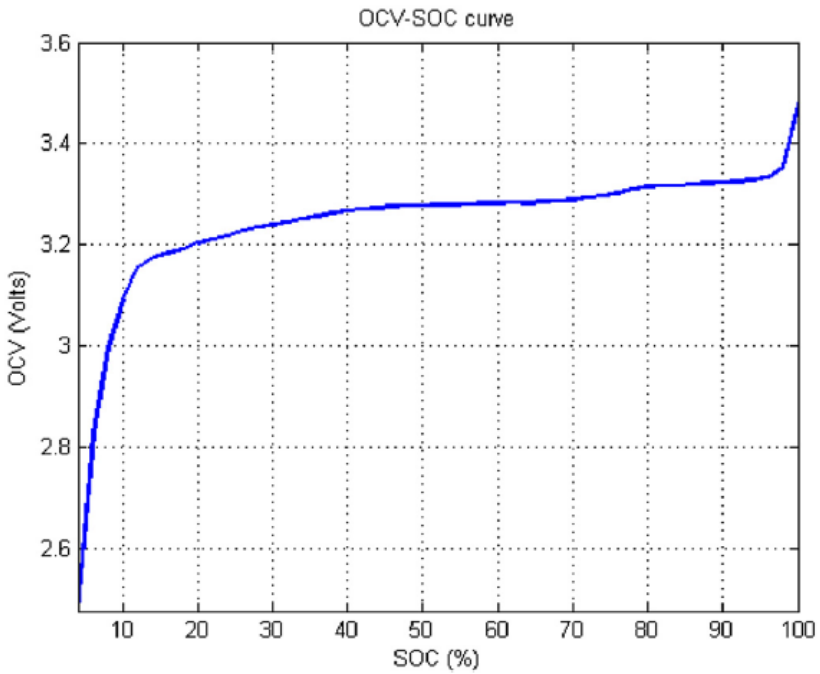

Figure 39 *OCV-SOC curve for $LiFePO_4$ battery cell. Adapted and reprinted with permission from [20].*

A multiple model adaptive estimation (MMAE), which is one of the observer-based fault diagnosis techniques, was applied employing a Kalman filter bank (KFB) of *n* filters. One observer represents the healthy condition of the process while the *n*-1 observers represent the fault conditions. The general layout of MMAE applied to non-linear battery model is shown in ***Figure 40***.

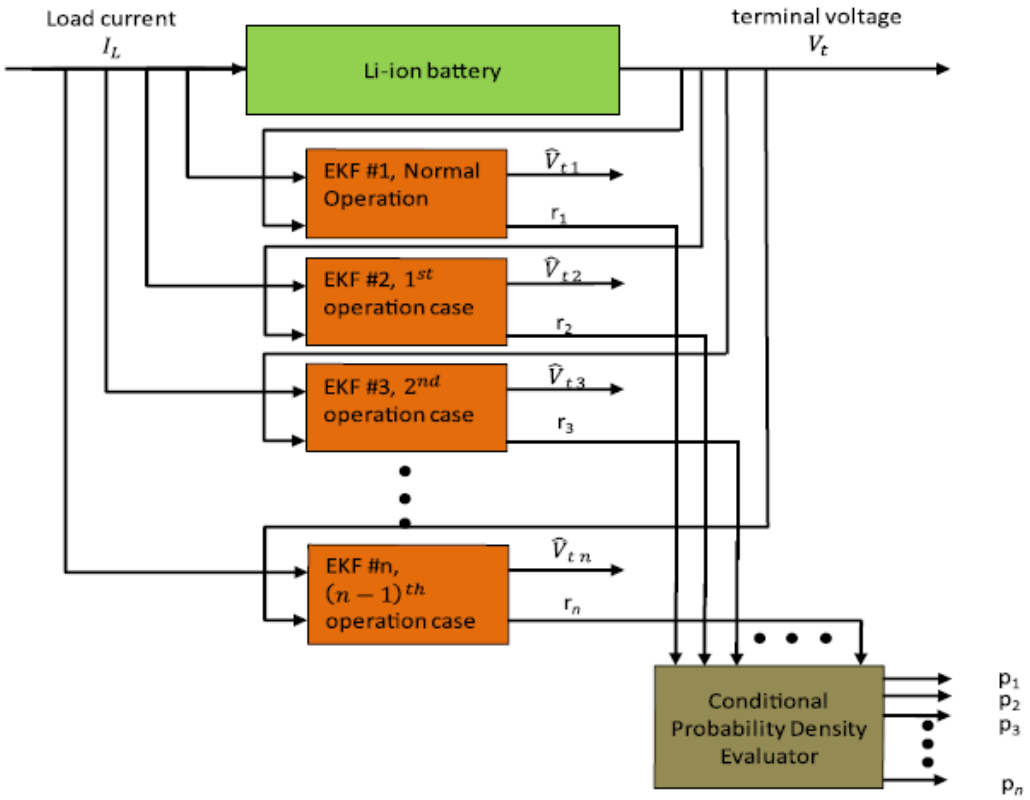

Figure 40 *MMAE residual generation and probability evaluation. The residual generation process consists in non-linear observers running parallel to the battery with all the n filters receiving the same input of load/charge current I_L and the terminal voltage V_t. The post processing part is depicted by the conditional probability density evaluator block where each of the n fault/operational hypothesis is assigned a probability of being true between the values 0 to and 1. The sum of all probabilities is equal to 1. Adapted and reprinted with permission from [20].*

The parameter values were extracted with the use of recursive least square (RLS) technique which consisted in fitting battery mathematical model to a sequence of observed battery current and voltage data by maximizing the sum of the squares of the difference between observed and computed data recursively. The battery was subjected to a nominal cycle of charge/overdischarge. The overdischarge followed the Navy overdischarge cycle and a 24 h overdischarge cycle which consisted in discharging the battery at maximum suitable discharge rate for 25% over discharge. Then the charging was carried out through a standard charging regime. The battery was cycled 25 times. After that the 24 h over discharge test regime was applied twice at a suitable discharge rate until SOC was equal to 0. The battery parameters were continuously monitored and collected. Signals were filtered for noise with low pass filters. From the recorded current and voltage data, the parameter values were estimated and multiple battery condition representing models were formulated. To test the performance of the condition monitoring setup, a scenario was created with consecutive change in the battery condition in a total simulation time of 213 s. The scenario was divided into four equal parts representative of the healthy and deteriorated performance of the battery due to overdischarge. The four parts were as follows: i) 0 - 53.25 s: healthy battery operation; ii) 53.26 - 106.5 s: battery operation after two 24 h overdischarge cycles; iii) 106.51 - 159.75 s: battery operation after twenty-five Navy overdischarge cycles; iv) 159.76 - 213 s: healthy battery operation. As depicted in ***Figure 41***, the y_m that represents the healthy battery operation in terms of terminal voltage measurement was compared to the estimated terminal voltage y_{new} (for the 1st and 4th phase), $y_{24\ hrOD}$ (for the 2nd phase) and y_{NavyOD} (referred to the 3rd phase). Each of them showed good match with the measured voltage within the associated range and marked deviation in the other time intervals.

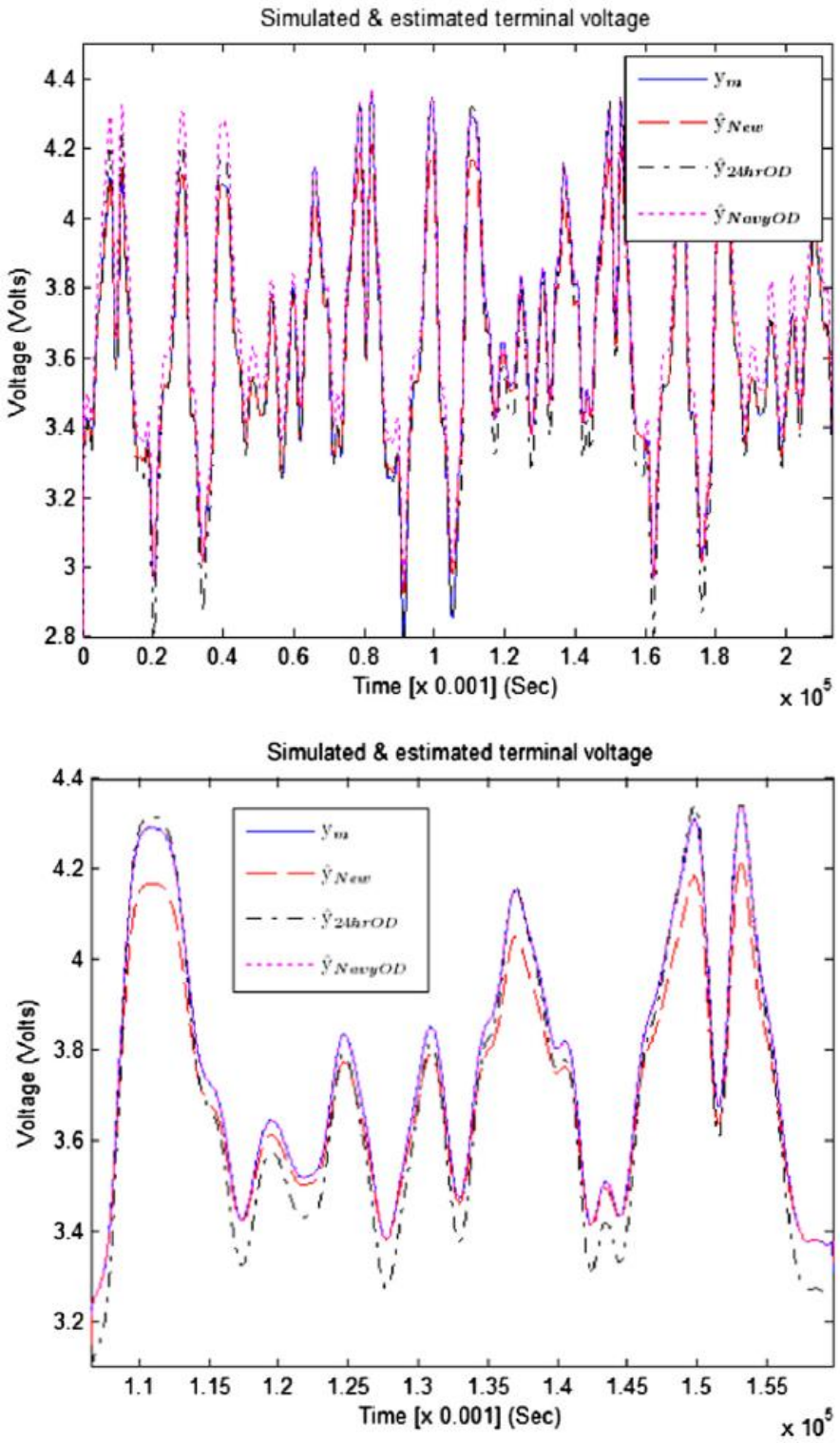

Figure 41 *Simulated and estimated terminal voltages from 0 to 213 s in the first graph and from 0 to 53.25 in the second one. Continuous blue line depicts the terminal voltage measurement. For each phase the good matching of the estimated terminal voltage associated to the corresponding phase with respect to the measured voltage is observed. Adapted and reprinted with permission from [20].*

Finally, the residuals were evaluated with a probability density function that confirmed the accurate behavior of the process by detecting the correct battery condition associated to the correct time.

To maintain high safety and reliability, battery management systems play a critical role in monitoring and evaluating battery health status, charge control, and cell balancing. In battery management systems, three critical parameters are monitored: state of charge, state of health, and state of life. Battery management systems need to predict the remaining capacity and battery health condition. Thus, the ability to accurately predict the state of charge and state of health of the battery system is crucial for advancing Li-ion battery applications. The literature reports both physics-based and empirical models for predicting the life cycle of lithium-ion batteries. Physics-based models usually focus on the internal electrochemical reactions of battery cells, such as the formation of the solid electrolyte interphase (SEI), which is considered the dominant factor leading to capacity fade. Empirical models, on the other hand, use data-based methods and model-based methods to describe the remaining useful life. Jian Guo *et al.* investigated how the battery performance metric of capacity fade is affected by different operating factors, usage profiles, and battery design factors [21]. Four samples for two types of batteries (CS2 with a rating capacity of 1100 mAh and CX2 with a rating capacity of 1350 mAh) were investigated with different discharge rates. Each battery was cycled at a constant discharge rate (1 C or 0.5 C) until the cutoff values of 4.2 V (for charging) and 2.7 V (for discharging). Typical trends for each discharge rate are illustrated in ***Figure 42***.

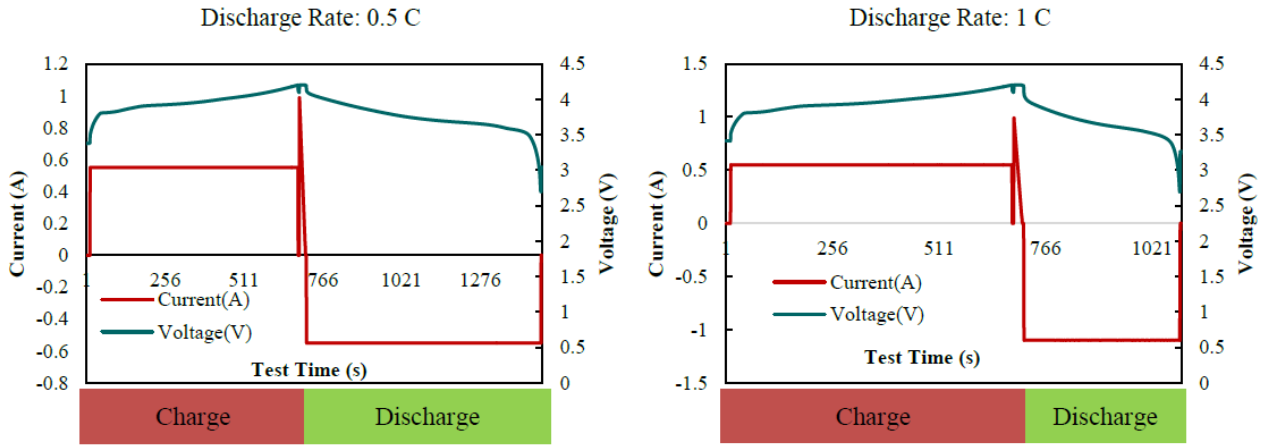

Figure 42 *Typical current and voltage change in one cycle under different discharge rates. Adapted and reprinted with permission from [21].*

A full factorial design was used considering the following design factors: i) number of cycles (0 - 300; 300 - 600; 600 - 900; > 900); ii) discharge rate (0.5 C; 1 C); iii) battery type (CS; CX) to investigate the capacity fade of the batteries. Two battery samples were used at each of the 16 treatment combinations and battery capacity was recorded at the end of each charge/discharge cycle. The main effects and the interaction plot are represented in ***Figure 43***. The results pointed out that the capacity of batteries decreases as the number of cycles increases but the rate of this decrease is not so marked within the first 200 cycles.

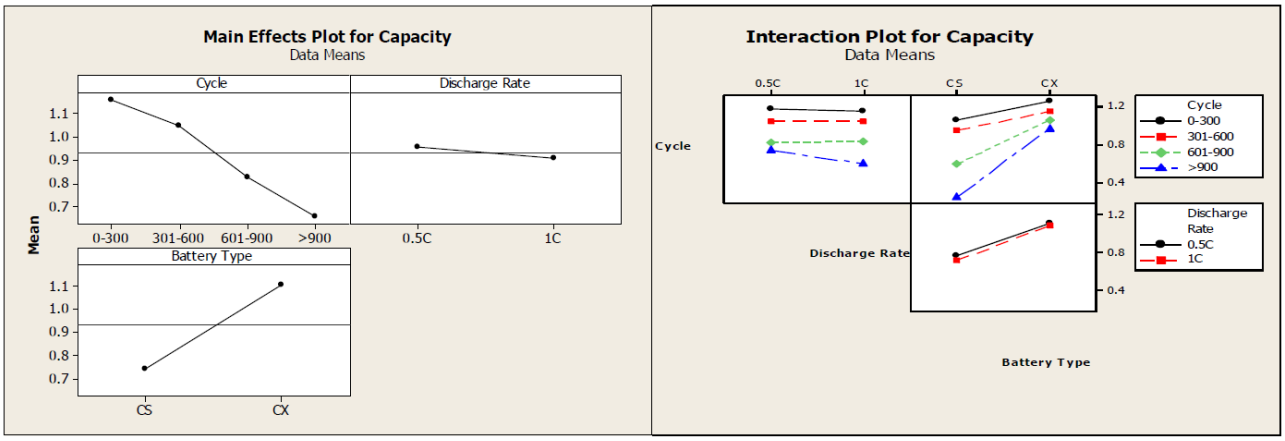

Figure 43 *Main effects plot and interaction plot for capacity. Adapted and reprinted with permission from [21].*

Moreover, the decline in capacity is more severe when the discharge rate is 1 C than when it is 0.5 C, regardless of the number of cycles or type of battery. The CX battery has a relatively higher capacity due to its higher rating and unique design. Finally, the number of cycles can be a strong indicator for monitoring the battery health status.

New charging strategy for lithium-ion batteries based on the integration of Taguchi method and state of charge estimation

Constant current constant voltage (CCCV) is the most used method for charging lithium-ion batteries. A new charging strategy for lithium-polymer batteries (LiPBs) has been investigated by Vo *et al.* based on the utilization of Taguchi method and state of charge estimation [22]. The goal was to improve the charging process by investigating an optimal charging current pattern in order to reduce charging time and temperature variation and maximize energy efficiency. The starting model was the multi-stage constant current (MCC). DoE was applied to search the optimal charging current pattern (Taguchi method) and to control and terminate the charging process (state of charge estimation). CCCV charging method was adopted to determine the influence of different levels of current on temperature variation, charging efficiency and charging time. Based on the obtained experimental results, a new charging strategy was defined taking into account that: the higher the charging current is, the shorter the charging time, the higher the temperature variation and so the lower the energy efficiency are. 4-stage constant current (FSCC) charging pattern was defined as shown in ***Figure 44***. Each stage consisted in a different pre-set charging current for 25% of SOC. For this, SOC estimation was necessary during the charging process. An online adaptive switching gain sliding mode observer (ASGSMO) based on battery equivalent circuit model was used.

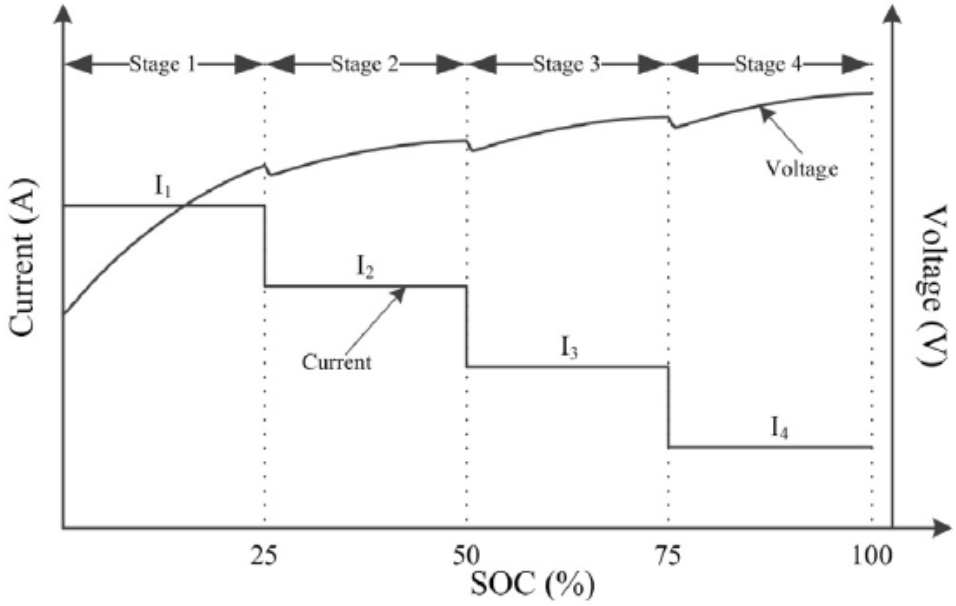

Figure 44 *Proposed charging current pattern. Adapted and reprinted with permission from [22].*

Taguchi method was applied to minimize the number of experiments to be conducted. Thanks to this optimization 9 experiments were performed from an initial number of 81. The experimental results were collected and divided into two categories: the-larger-the-better for energy efficiency and the-smaller-the-better for charging time and temperature variation. The new charging strategy was applied to 5.8 Ah LiPBs with different initial SOC and also to 5.8 Ah and 5.0 Ah LiPBs at the same initial SOC to demonstrate the efficacy of the new charging model to different capacities and life cycles. Results demonstrated that the charging time was reduced by 22.5% (about 15 min) and also the temperature variation during the charge was almost half with respect to CCCV method.

State-of-health monitoring of lithium-ion batteries in electric vehicles by on-board internal resistance estimation

The internal resistance of a battery cell is the characteristic most affected by degradation. Monitoring it is very important but at the same time complex. Traditionally, this kind of control is performed in laboratory. For EVs, having an on-board system to monitor the state of health (SOH) of the battery is desirable. Therefore Remmlinger *et al.* developed a model deduced from an equivalent circuit which used specific signal intervals with a defined timespan occurring regularly during the normal operation of the battery in EVs [23]. Recorded data from inner-city driving of an EV were selected and analyzed in a laboratory. Tests were carried out at different temperatures of -20, -8, 12, 30 and 50 °C. The start of the combustion engine of the hybrid vehicle was selected as promising timespan for the determination of internal resistance because generated a signal of 2.5 s as a strong excitation of the battery. To compare the results two batteries were used: a new and a degraded 6.5 Ah Li-ion batteries. Internal resistance and capacity were determined. The identification of the internal resistance was done through the special identification signals of terminal voltage and current at the start of the combustion engine with an adapted model. This model was the result of a simplification from the continuous-time frequency domain to the discrete-time frequency domain (z-domain):

$$G(z) = \frac{U(z) - U_{OCV}}{I(z)} = \frac{b_1 z^{-1}}{1 + a_1 z^{-1}}$$

with a_1 and b_1 linear parameters. The internal resistance was then calculated as:

$$R_i(\theta) = \frac{b_1(\theta)}{1 + a_1(\theta)}$$

Figure 45 shows the internal resistance calculated at several temperatures.

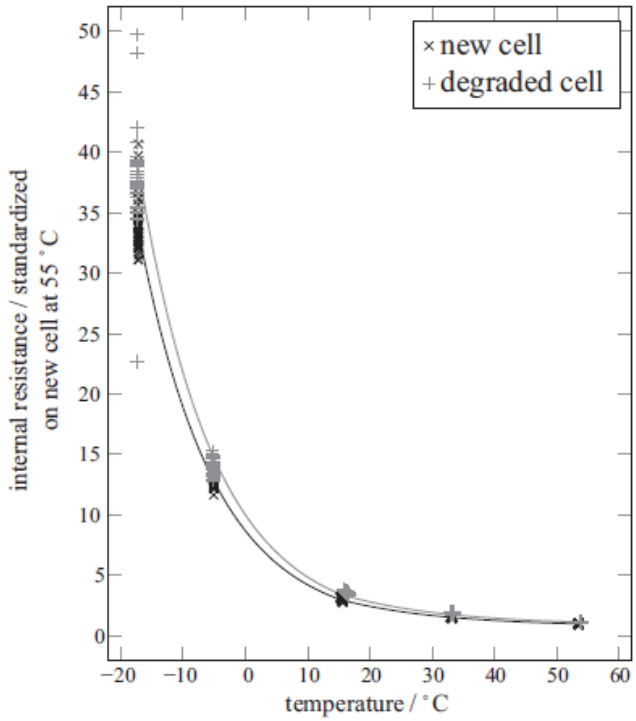

Figure 45 *Internal resistance at different temperatures at start of combustion engine. Adapted and reprinted with permission from [23].*

The next step was to express a degradation index k_d with respect to the internal resistance independent of the actual cell temperature of the measurement.

$$R_{i,new}(\theta) = a\, e^{-b\theta} + c$$

and k_d was calculated by solving the equation:

$$R_{i,act} = k_d R_{i,new}(\theta_{act})$$

The monitoring method is represented in ***Figure 46***.

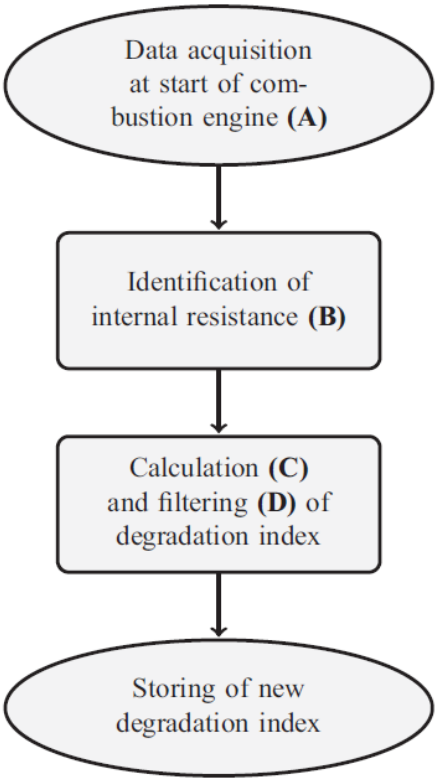

Figure 46 *Operation chart of monitoring algorithm. Adapted and reprinted with permission from [23].*

The application of the method on testing data from laboratory is shown in ***Figure 47***.

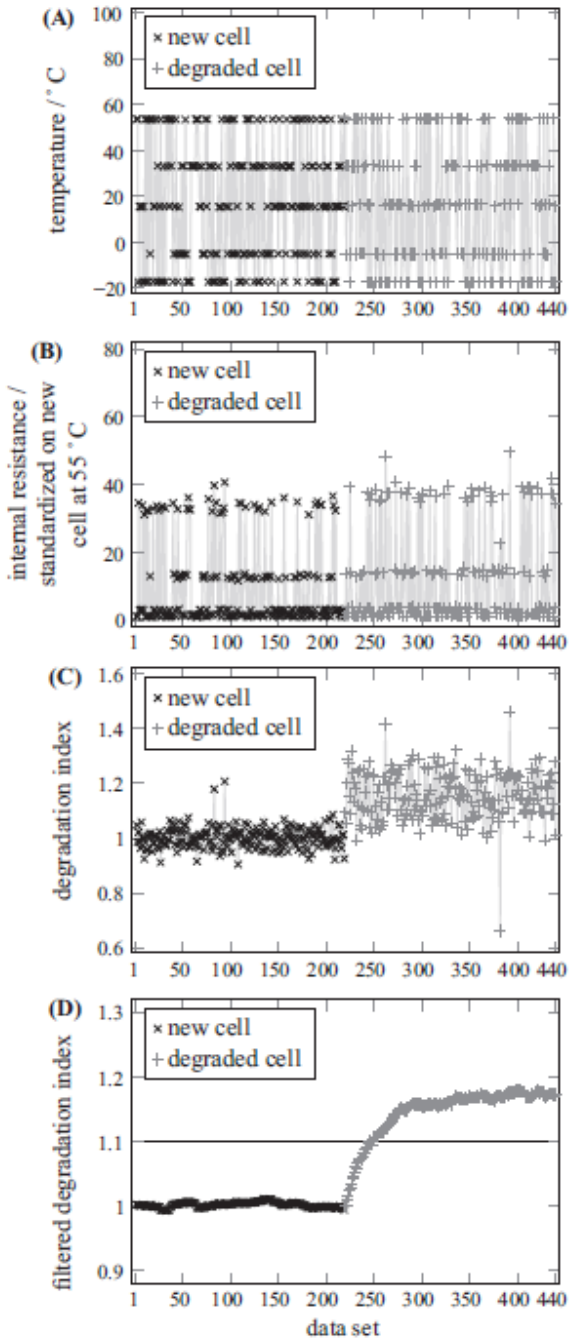

Figure 47 *On-board application of the monitoring algorithm. Adapted and reprinted with permission from [23].*

For each cell more than 200 data sets of the identification signal were recorded. For the pairs of values consisting of temperature (plot A) and internal resistance (plot B), the degradation index (plot C) is calculated. The degradation index for each of the two cells is almost constant with only some outliers. A low-pass filter was applied to remove the effects of the outliers and to give the degradation index a smooth appearance.

Battery Pack Temperature Estimation Model for EVs and Its Semi-transient Case Study

Use of Li-ion batteries is very popular due to their high energy density, but they also exhibit the rare but severe failure mode of fire/explosion for electric vehicles (EVs). Therefore, for the further growth of the Li-ion battery business, the safety problem should be addressed. Most failure modes of Li-ion batteries are related to temperature increase. It is important to keep the temperature below a certain limit value for

prevention of the battery failure due to thermal runaway. Even if not related to battery failure directly, temperature increase may degrade battery performance significantly. The current method of thermal monitoring for EVs uses multiple thermostats. However, as the size of the battery system increases, the number of thermostats also increases, which can lead to sensor malfunction and increased maintenance costs. To address these issues, Tae Jin Kim *et al.* investigated an alternative method of monitoring to minimize the number of sensors [24]. Three phases were defined to reach the objective: i) devising battery thermal characterization tests under various operating conditions; ii) developing an online-applicable temperature prediction model using artificial neural networks (ANNs); iii) validating the temperature prediction model. The proposed temperature prediction model was demonstrated using an EV battery pack that consists of twelve battery modules. For the first phase, Li-ion battery cells with 50 Ah capacity and 3.7 V nominal voltage were employed. The governing equation which described the test conditions was:

$$\dot{Q}_{gen} = \dot{Q}_{stor} + \dot{Q}_{conv} = \rho * V * C * + h * A * (T - T_a)$$

with ρ the density, V the volume, C the heat capacity, h the heat transfer coefficient, A the surface area, T and T_a the temperature of the specimen and ambient temperature, respectively.

The value of h and C were calculated by applying the previous equation to 2 test conditions as shown in ***Figure 48 (a)*** and ***Figure 48 (b)***. The method involves heating up an aluminium specimen to a stable temperature of 40 °C and then removing the heat source. When the heat source is removed, the heat is only dissipated and not stored, which allows for the estimation of h. Twenty experiments were conducted to ensure the value of h, resulting in a mean h of 1.1153 (W/m^{2}K) with a standard deviation of 0.0085 (W/m^{2}K). Similarly, 20 experiments were conducted to ensure the value of C by heating up the battery up to 40 °C and relaxing to ambient temperature: in this way C was the only unknow. Result was a mean C of 1.7150 (J/gK) with a standard deviation of 0.0113 (J/gK).

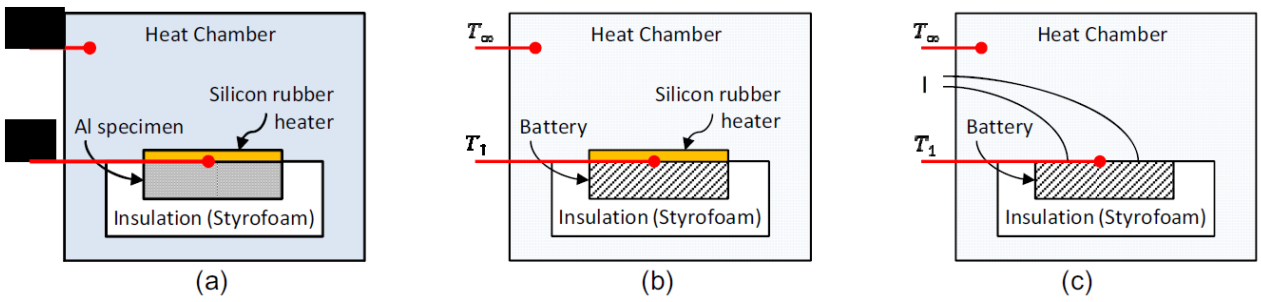

Figure 48 *Test conditions for the definition of h (a), C (b) and heat generation rate (c). Adapted and reprinted with permission from [24].*

With the values of h and C determined, the heat generation rate of the battery during charging or discharging can be evaluated by tracking the temperature change as shown in **Figure 48 (c)**. The heat generation rate is dependent on various factors, including charging/discharging rate, state of charge (SOC), and ambient temperature. To reflect the fluctuation of the charging/discharging rate, a dynamic current profile from an EV driving test was used to determine the test conditions. The histogram from this profile is fitted to a beta distribution, and Gauss-type quadrature formula is used to determine the test conditions as 6, 46, and 103 A. Additionally, the average air coolant temperature was assumed to follow a Gaussian distribution with a mean of 22.5 °C according to auto company. Using the Gaussian-type quadrature formula, test conditions were chosen as 14, 22.5, and 31 °C.

A computer model, based on computational fluid dynamics (CFD) simulation, was used to predict the temperature of a battery pack for EVs. The battery pack contains 12 modules, but only 6 of them are modelled by the simulation software, ANSYS FLUENT, because the other 6 modules are placed in a

symmetric configuration. ANNs were used to create a more computationally efficient model with essential information. The ANN model used 3 inputs: coolant fan velocity, heat generation rate, and only one sensed temperature located at one of the 6 modules, and estimates the remaining 5 temperatures of the modules.

The ANN model was trained using simulation results and validated using different conditions. It was able to estimate temperature in a semi-transient case, which simulated temperature changes over time under constant charging/discharging conditions. The maximum error of the temperature estimation was 0.2722 °C, and the average error is 0.1951 °C. The results are shown in ***Figure 49***.

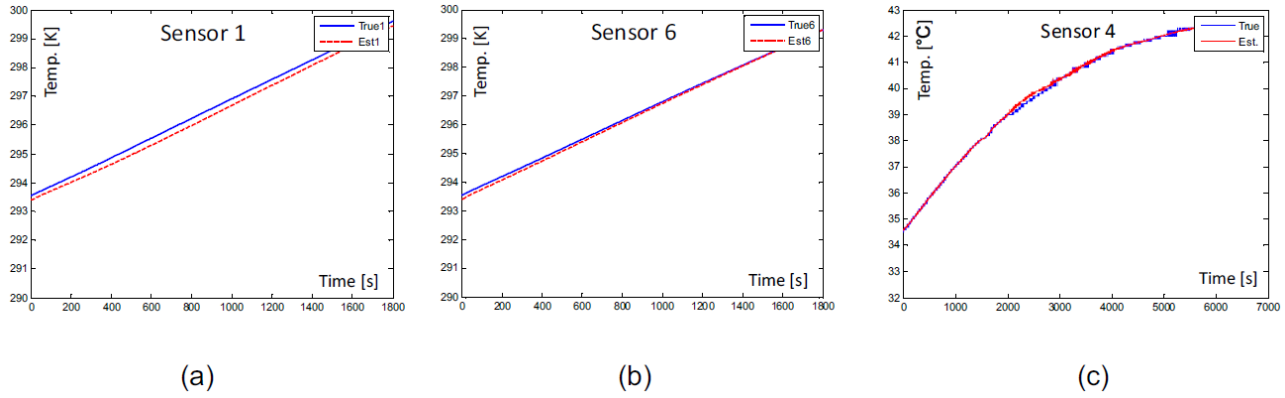

Figure 49 *Estimated temperature of sensor 1 (a), sensor 6 (b) in simulation and sensor 4 in test (c). Adapted and reprinted with permission from [24].*

Section 2.3: DoE for Synthesis and Material Optimization

Application of the methodology of Design of experiments to the development of Li-Ion battery active materials

Another positive example of the use of DoE in the search for high energy cathode materials for Li-ion batteries was reported by Sebastien Martinet *et al.*, who determined the optimal mixture to produce lithium rich lamellar oxides as iron-substituted lithiated phosphate materials [25]. More in detail, starting from the general formula $LiFe_xM_{1-x}PO_4$ (with $0 \leq x < 1$ and M = Mn, Co, Ni, or a mixture of them), the challenge was to investigate which was the best composition among several possibilities. The objective was to maximize the capacity of the compound (expressed in mAh/g). A surface response design including 6 input parameters allowed to determine the influence of the input parameter on each output. Subsequently, a multiparameter optimization was applied to obtain the best compromise with the result of increasing the discharge capacity from 200 to 250 mAh/g with a significant saving in the number of experiments performed (***Figure 50***).

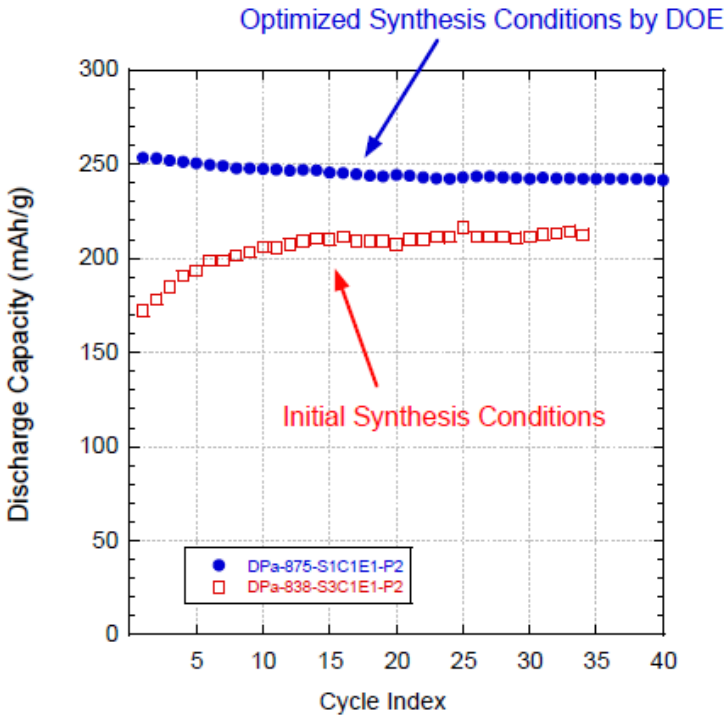

Figure 50 *Li-rich lamellar oxide LNMO discharge capacity at C/10 rate as a function of cycle number. Red points: non optimized synthesis. Blue points: optimized synthesis by DoE. The result of the applied DoE is evident. Adapted and reprinted with permission from [25].*

Combined structural, chemometric, and electrochemical investigation of vertically aligned TiO_2 nanotubes for Na-ion batteries

Secondary batteries are very suitable for the implementation of the renewable energy into the grid. An alternative to the most common LIBs is represented by the sodium-ion batteries (NIBs). While Li offers the highest energy density among present battery technology but also high price, Na is very abundant and so cheaper. The challenge for this type of battery is related to the choice of the anode materials: graphite cannot be used because of its low performance if combined with sodium ions. One of the solutions which are under study is the titanium dioxide (TiO_2), which has a comparable behavior to graphite as anode in LIBs. This is not sufficient because of its intrinsic low electronic conductivity. The use of one-dimensional TiO_2 nanostructures like nanowires, nanorods or nanotubes provides a suitable solution providing shorter electron diffusion paths. Nanotubular arrays (TiO_2 NTs) made by anodic oxidation represents a very effective

strategy. Within this framework, researchers are investigating about what is the best polymorph (e.g. amorphous or crystalline anatase/rutile) referring to the overall capacity output and long-term performance considering the potential modification to the nanostructure during the cell operation. Bella *et al.* proposed a DoE approach to identify the best TiO_2 polymorph for NIBs [26]. The identified parameters of interest were: i) TiO_2 NTs array length; ii) effect of crystallization. The tests on the sodium cells were performed at ambient temperature through constant current at various regimes between 0.1 to 5 mA cm^{-2}. Using a DoE approach, the growth time of TiO_2 NTs (in a range of 1 to 10 min) and the annealing temperature (in a range between 25 to 600 °C which corresponded to non-annealed temperature, *i.e.*, amorphous samples and crystalline samples, respectively) were concurrently varied to study their correlation and weight with the results. Fourteen sodium cells were assembled and tested using a chemometric approach. The chemometric matrix was filled with the data related to the capacity values of the sodium cells at the 85th cycle. This approach consisted in choosing a set of "potential good experiments" included in the experimental domain. After that, a statistical criterion was chosen. In this case G-efficiency (G_{eff}) was used as follows:

$$G_{eff} = \frac{100*p}{n*d}$$

where *p* is the number of terms in the model, *n* the number of experiments in the design and *d* the maximum relative prediction variance over the candidate set. Higher values of G_{eff} mean higher probability to obtain the maximum amount of information from the experimental setup. The parameters of the multiple linear regression were $Q^2 = 0.79$ and $R^2 = 0.95$, which are very close to 1 indicating a high quality of the model fitting. The best result reached was a specific capacity of 90.9 µAh cm^{-2} (***Figure 51***). This result was obtained with the cell assembled with the amorphous TiO_2-am sample, growth time of 10 min and annealing temperature of 25 °C. Moreover, the Student's t-test was applied, and it confirmed the existence of a dependency between variables with a probability of 95%. Successively a progressive decay for the amorphous and anatase was observed. A new test was performed and the data of the 250^{th} cycle were used. It was showed that the anatase phase has a better long-term cycling performance over the amorphous phase and the bad influence of the rutile phase (obtained upon calcination at 600 °C) on the specific capacity output. It was clear that there is a distinction in performance among anatase, rutile and amorphous TiO_2.

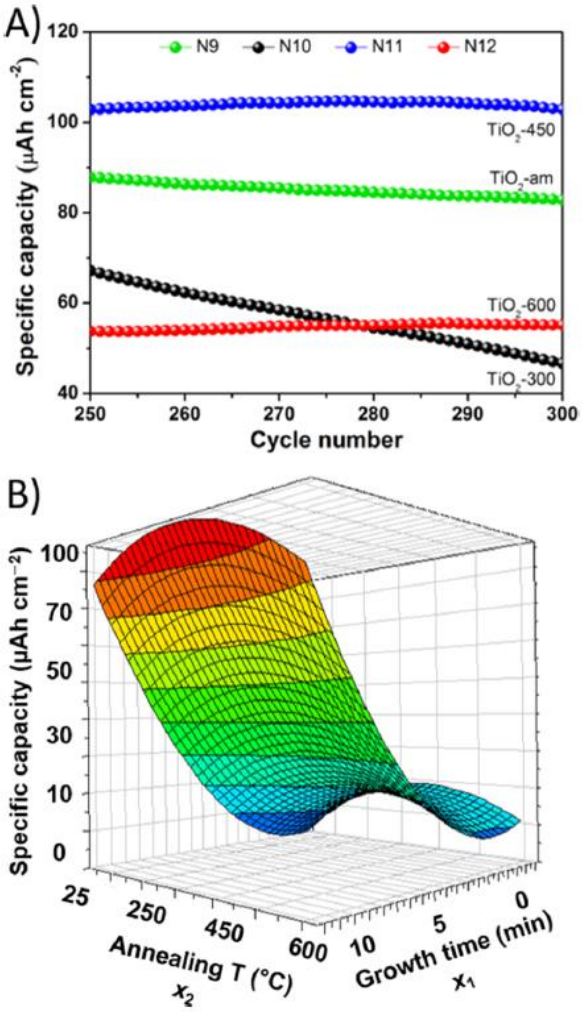

Figure 51 *(A) Specific discharge capacity values under 0.1 mAcm^{-2} for sodium cells assembled with TiO_2 NTs array working electrodes (growth time = 10 min) between the 250th and 300th cycle; (B) response surface showing the effect of annealing temperature and growth time on the specific capacity at the 250th cycle of lab-scale sodium cells. Adapted and reprinted with permission from [26].*

In particular, the single-phase anatase polymorph obtained by calcination at 450 °C reached the highest specific capacity value after 300 discharge/charge cycles. Also, the presence of rutile formed by calcination at 600 °C determined a decrease in the overall specific capacity output.

Design of experiment methodology to improve the energy density of lithiated metal phosphates

Phospho-olivines and in particular $LiFePO_4$ (LFP) are increasingly used as cathode materials for Li-ion batteries due to their thermal stability which is fundamental from a safety point of view. They also suffer from a lower average voltage in discharge in comparison with other lithiated metal oxides used for Li-ion cells. Sebastien Martinet *et al.* investigated the method of substituting iron by other transition metals as manganese (Mn) or cobalt (Co) [27]. DoE was applied for multi-transition metal phosphate optimization. The focus was on manganese "rich" compounds in a specific solid solution domain: 0 - 33% for both iron and Co; 28.4 - 90 % for Mn. Moreover, boron doping was evaluated up to a maximum of 5%. Studied materials followed the formula: $LiFe_{(1-x-y-z)}Mn_xCo_yB_zPO_4$. The fact that the sum of iron, Mn, Co and B has to be always equal to 1 led to a "mixture designs" DoE. MINITAB software was used resulting in a set of 21 trials; all of them performed by a specific experimental protocol: active materials were prepared by a solid-state synthesis based on ball milling and heat treatment at medium temperature. Synthesis conditions were adjusted during preliminary test to lead to a good synthesis of the olivine phase. Testing of the capacities was done in a room temperature with an Arbin tester at C/10 rate. The trials were performed in

random order. Obtained results of specific capacities varied in a range between 14 and 115 mAh g^{-1}. The data were analyzed based on a linear model consisting in 4 linear effects and 6 interactions. The fit of the model with the experimental measured values is shown in ***Figure 52***.

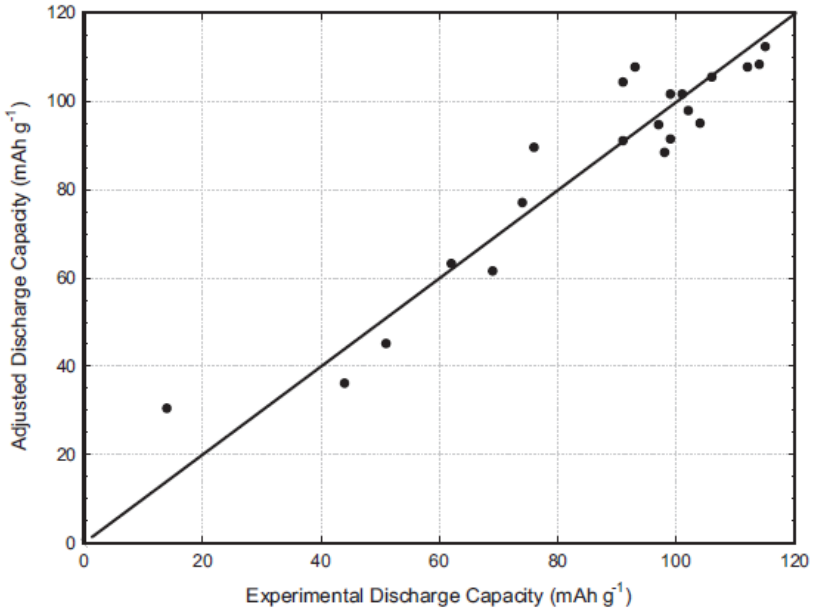

Figure 52 *Adjusted values of the discharge capacity obtained with the model as a function of experimental values. Adapted and reprinted with permission from [27].*

It was noticed that results were very sensitive to boron content, so an optimal value was identified (2.5%). Results are shown on **Figure 53** in the mixture contour diagram with iso-response lines.

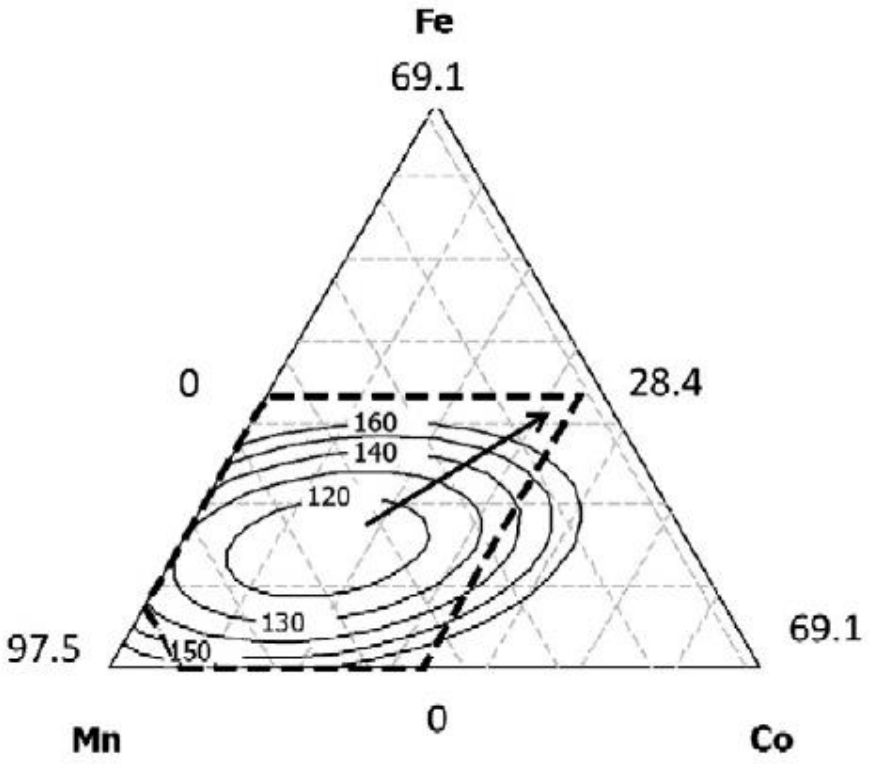

Figure 53 *Mixture contour diagram for the response discharge capacity at first cycle in mAh g^{-1} (boron content fixed at 2.5%). Adapted and reprinted with permission from [27].*

It was notable that high values of discharge capacity were reached at minimum level of Mn. So, it was performed an additional test with a further synthesized compound: $Mn_{0.309}Co_{0.333}B_{0.025}PO_4$ with a result of 123 mAh g^{-1}.

Design-of-experiments-guided optimization of slurry-cast cathodes for solid-state batteries

Solid-state batteries (SSBs) are defined as the next generation of lithium batteries. They are composed of cathode composite, the solid-electrolyte separator layer and the anode composite (or Li metal). There are two groups of solid electrolytes: i) sulfides/oxides; ii) polymers. To be cost competitive with LIBs and scalable, sheet-based design has a fundamental role despite numerous challenges for the production. Within this framework, Teo *et al.* investigated a cathode-composite preparation process for improved electrochemical performance with a DoE approach [28]. Constituent elements (three types of binders and two types of carbon additives) were selected, and a set of various combinations were tested within SSB full cells with a carbon-coated $Li_4Ti_5O_{12}$ (LTO) anode. A schematic overview of the DoE approach is represented in ***Figure 54***.

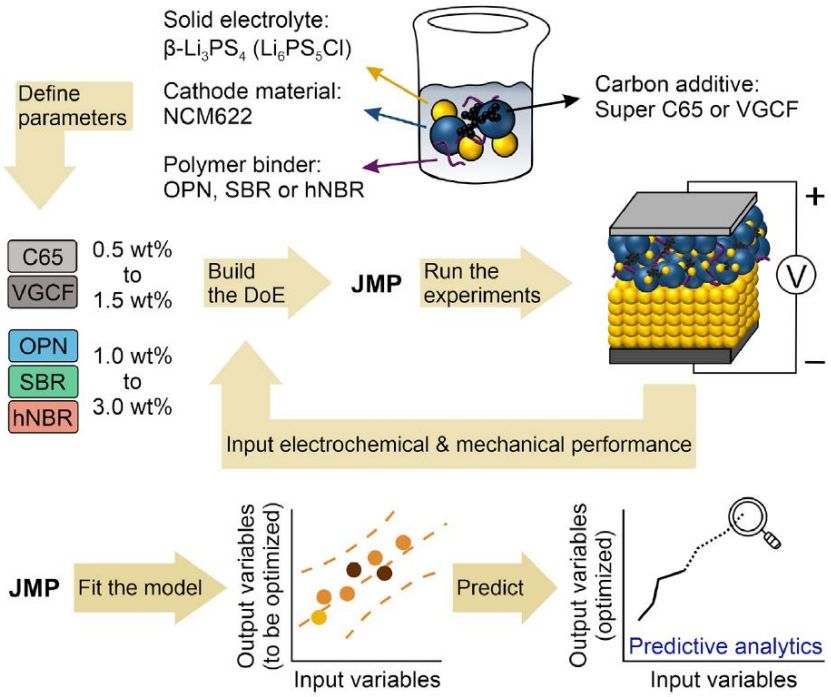

Figure 54 *Schematic overview of the DoE-guided approach for tailoring of slurry-cast cathodes. The data were elaborated by the software to build a linear model to predict and optimize the material's combination. Four material-related parameters were considered: i) carbon type (Super C65 carbon black or vapor-grown carbon fibers [VGCF]) in categorical roles; ii) carbon content (0.5 – 1.5 wt%) in continuous role; iii) binder type (polyisobutene [OPN], poly(styrene-co-butadiene) rubber [SBR], or hydrogenated nitrile butadiene rubber [hNBR]); iv) binder content (1.0 – 3.0 wt%) in continuous role. 23 runs were executed, and the results valuated according to capacity retention and specific discharge capacity after 20 cycles; moreover, mechanical properties were evaluated and used as the second set of input variables. Adapted and reprinted with permission from [28].*

Response surface model (RSM) was used to investigate the interactions among variables. Capacity retention was monitored to establish the cell degradation; the specific discharge capacity was investigated to obtain an indication of the practical energy storage capability of the cell. The specific discharge capacity was chosen to represent the electrochemical performance: a slurry-cast cathode with 1.0 wt% OPN and 0.5 wt% VGCF was found as the optimum. Binding and punching tests were realized to investigate the processability of the slurry-cast cathodes. The optimum was found with a larger fraction of polymer binder (2.7 wt%). The results of the test with the optimized slurry-cast cathode are represented in ***Figure 55***.

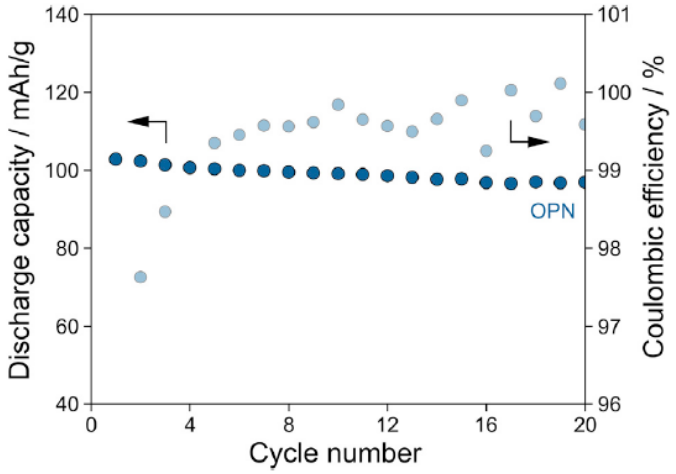

Figure 55 *Discharge capacity over 20 cycles and corresponding Coulombic efficiency of a slurry-cast cathode (NCM622, β-Li_3PS_4) optimized for processability and electrochemical performance. The measured value of ~90 mAh/g_{NCM622} at the 20th cycle, which is in line with the extrapolated value of ~93 mAh/g_{NCM622}, demonstrates the robustness of the model constructed with the DoE approach. Adapted and reprinted with permission from [34].*

Designs of experiments for beginners - a quick start guide for application to electrode formulation

A design of experiments is a strong tool to manage the choice of the responses that describe a system and of the factors to vary considering the time, the cost and the overall complexity of the experiment so as to obtain a statistical relevant empirical equation which models the studied system. This procedure becomes really useful because has the advantage of reducing the number of experiments. Of course, the risk of obtain false positive results has to be taken into account. The biggest advantage of DoE is that it allows to run an optimized set of experiments to identify factor impacts and combined interactions and, based on these results, build an empirical model which describes the investigated process. Among the different types of DoE, Optimal Combined Design (OCD) uses categoric factors such as the material of a binder, and numerical factors such as the temperature. The response is expressed as a function of different factors based on the empirical model. This approach is described in ***Figure 56*** and was applied by Rynne *et al.* to study the effect of electrode formulation on the capacity of Li-ion batteries at high currents [29].

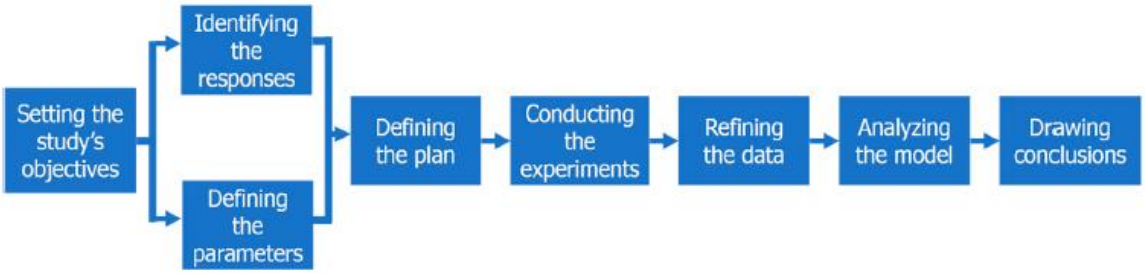

Figure 56 *Flowchart describing the workflow to plan and conduct a DoE. Adapted and reprinted with permission from [47].*

The scope of the study was to identify a new binder material and to understand the importance of conductive additives for high-power applications. After that, electrode's capacity under high currents was defined as response. Defining of the design factors was conducted choosing a maximum of four different constituents as follows: i) lithium iron phosphate ($LiFePO_4$) as active material; ii) polyvinylidene fluoride (PVDF) as binder; iii) carbon black, carbon nanofibers or conductive polymer as conductive additives. Next step consisted in the definition of the boundaries in which each factor could vary. The active material was desirable to be maximized, while binder should be minimized. The additives should be enough to guarantee

sufficient electronic conductivity but their amount should also be kept small because of their inactivity in the energy storage process.

Microscopy imaging based numerical model of Li-ion batteries electrode: a parametric study through a design of experiment approach

Li-ion battery is a complex system in which a series of different phenomena occur. These are ions transportation, charges movements and electrochemical surface reactions and occur within different media inside the electrode. Optimizing the electrode and the microstructures is one of the strategies to overcome performance limitations. To do this the parametrization of physics-based models is fundamental but requires expensive investments in terms of economy and time. DoE can be really useful for this aim. Kerdja *et al.* developed a multi-physics model to simulate electrochemical cycling at the electrode microstructure level [30]. Starting from a 2D scanning electron microscopy (SEM) image of a NMC 111 ($LiNi_{1/3}Mn_{1/3}Co_{1/3}O_2$) they obtained the microstructure used for their model. More specifically, the electrode was made of commercial NMC 111 (92%) active material, black carbon (4%) and Polyvynilidene Fluoride (PVdF) as mechanical binder. ***Figure 57*** shows the SEM image and its elaboration. The focus was on 5 parameters of interest: i) diffusion coefficient in solid phase (D_s); ii) diffusion coefficient in liquid phase (D_l); iii) effective conductivity of carbon-binder domain (σ_{CBD}); iv) ionic conductivity of electrolyte (σ_{ion}); and v) exchange current density (i_{00ref}). Each parameter was varied around its reference medium value to investigate the influence over discharge capacity and active material (AM) lithiation heterogeneities. Then a combined optimization was performed.

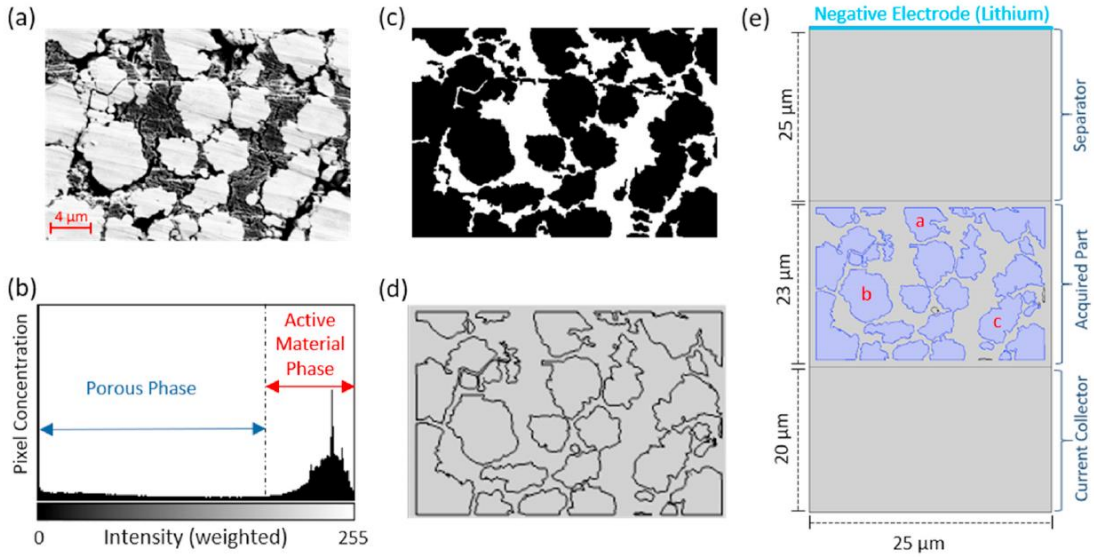

Figure 57 *(a) 2D SEM image of the NMC 111 based electrode. (b) Grey level histogram of image (a), showing that the three phases are not clearly distinguished. (c) Segmented version of image (a). (d) Vectorization version of the image (c) to obtain the reconstructed 2D virtual Li-ion cell (e). Adapted and reprinted with permission from [30].*

Multi-physics numerical model was obtained with the use of general equations for the charge ($\vec{j}$), mass ($\overrightarrow{N_+}$) and heat ($\vec{Q}$) fluxes. The evolution of temperature was assumed negligible, so temperature was a constant. Transport number t_+ was assumed constant and equal to zero within the AM.

$$\vec{j} = -\sigma \vec{\nabla} \tilde{\varphi} + \sigma \frac{(1-t_+)}{F_{z+}} \left(\frac{\partial \mu}{\partial C}\right) \vec{\nabla} C - \beta \sigma \vec{\nabla} T$$

$$\overrightarrow{N_+} = -D \vec{\nabla} C + \frac{t_+}{F_{z+}} \vec{j} - \frac{DCk_T}{T} \vec{\nabla} T$$

$$\vec{Q} = -\gamma \vec{\nabla} T + \beta T \vec{j} + k_T C \left(\frac{\partial \mu}{\partial C}\right) \left(\overrightarrow{N_+} - \frac{t_+}{F_{z+}} \vec{j}\right)$$

Butler-Volmer theory described the intercalation and deintercalation reactions occurred at the AM. Three levels for each parameter were chosen in accordance with the literature (reference, minimal and maximal value). Based on the statistical theory, 3^5 combinations were obtained for a total of 243 potential experiments. DoE methodology enabled to reduce them to 46 sets. Pareto diagram was used to classify the different terms according to their normalized effect and to study their positive or negative effect on the measured values. The analysis was conducted with an imposed 2*C* current of 1.76 mA cm^{-2}. Capacity values for the 46 experiments were classified into three groups: i) inferior to 80 $mAh \cdot g^{-1}$, ii) between 96 and 131 $mAh \cdot g^{-1}$ and iii) superior to 135 $mAh \cdot g^{-1}$. DoE analysis allowed to suppress the non-significant terms. So, the regression equation *Y* for the discharge capacity was obtained. The exchange current density (i_{00ref}) dominated in terms of influence followed by the liquid diffusion (D_l) and solid diffusion (D_s), all contributing with their linear and quadratic effects. Only a single interaction between D_l and i_{00ref} was included in the model according to its value. Moreover, the effects of D_l and D_s were compared focusing on the three groups of capacity values as follows: 1) 129 ± 2 $mAh \cdot g^{-1}$ (D_l and D_s minimal or medium); 2) 117 $mAh \cdot g^{-1}$ ± 4 (D_s minimal and D_l medium or maximal); 3) 98 ± 2 $mAh \cdot g^{-1}$ (D_l minimal and D_s medium or maximal). In the last two groups, discharge capacity was limited. A further analysis was conducted to compare the influence of solid and liquid diffusion limitations mechanisms focusing on the final lithium concentrations maps of the electrolyte and the AM according to the cases ii) and iii) (see ***Figure 58***).

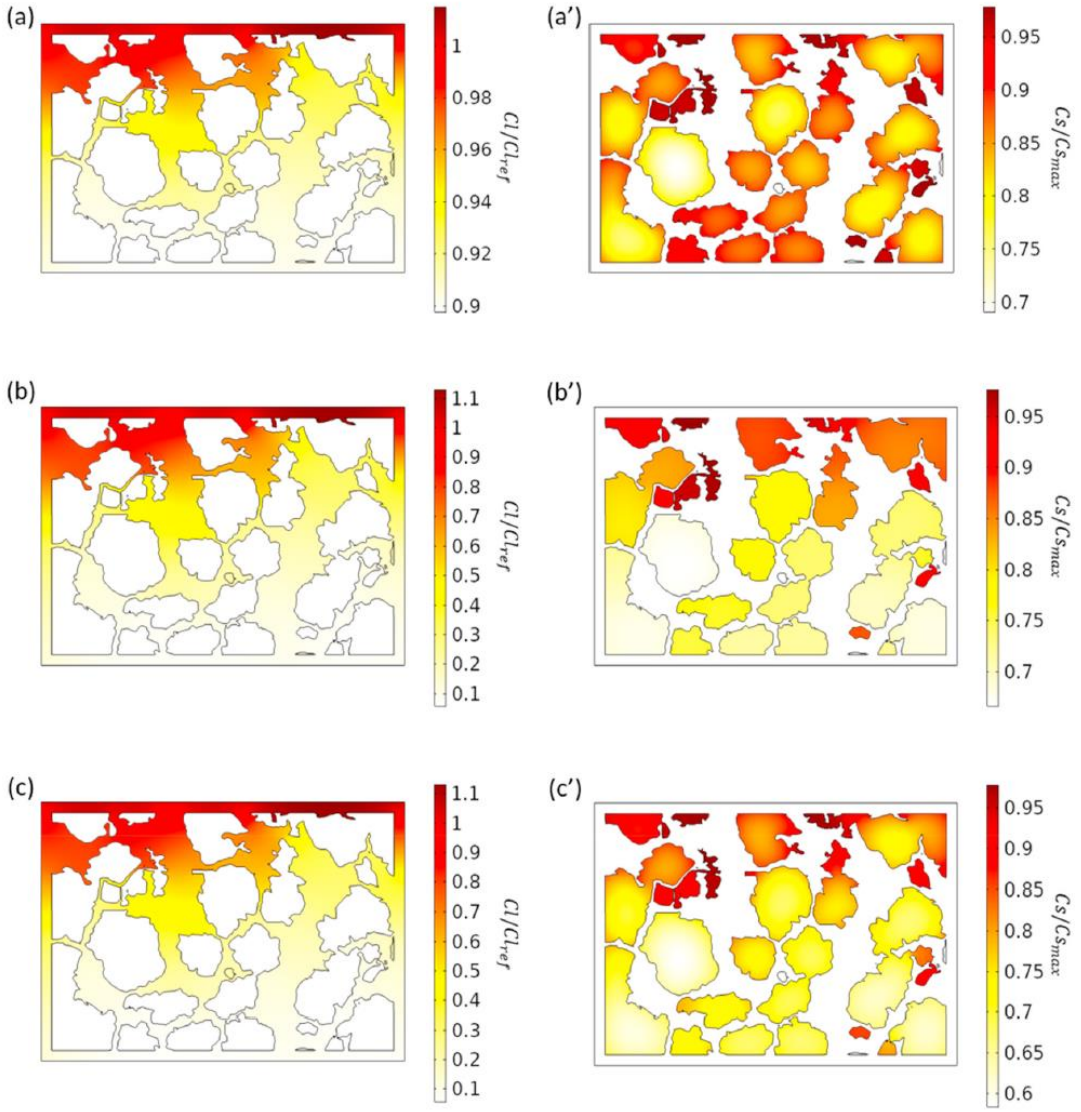

Figure 58 *(a) and (a') Lithium concentration within the electrolyte for the case 2) where the variation observed was < 10% and lithium concentration within AM is considerable in terms of heterogeneities within each individual particle. For the case 3) (b and b'), high heterogeneities of lithium concentration in the electrolyte were evidenced: regions close to separator had ten times Li^+ than those near the current collector caused by the low D_l; about the lithium concentration in AM, it was clear there were not marked heterogeneities in individual particle but it was higher close the separator. (c) and (c') show similar heterogeneous distribution as for the case 2) referring to the Li^+ concentration within the electrolyte; however, active particles showed lithiation levels depending both on the particle's position and its developed surface. Adapted and reprinted with permission from [30].*

It was found that many limitations mechanisms co-exist and that lithiation can be limited by liquid diffusion influenced by particles' position and by solid diffusion influenced by particles' developed surface.

Finally, with the help of DoE, the statistical influence of the five parameters was investigated taking into account two types of heterogeneities: local (within a single particle) and global (the whole AM phase). The study consisted in the quantification through a Normalized Absolute Average Deviation to quantify the deviation of lithium concentration from its average value. Pareto diagrams in ***Figure 59*** according to the regression equation report the most influent parameters.

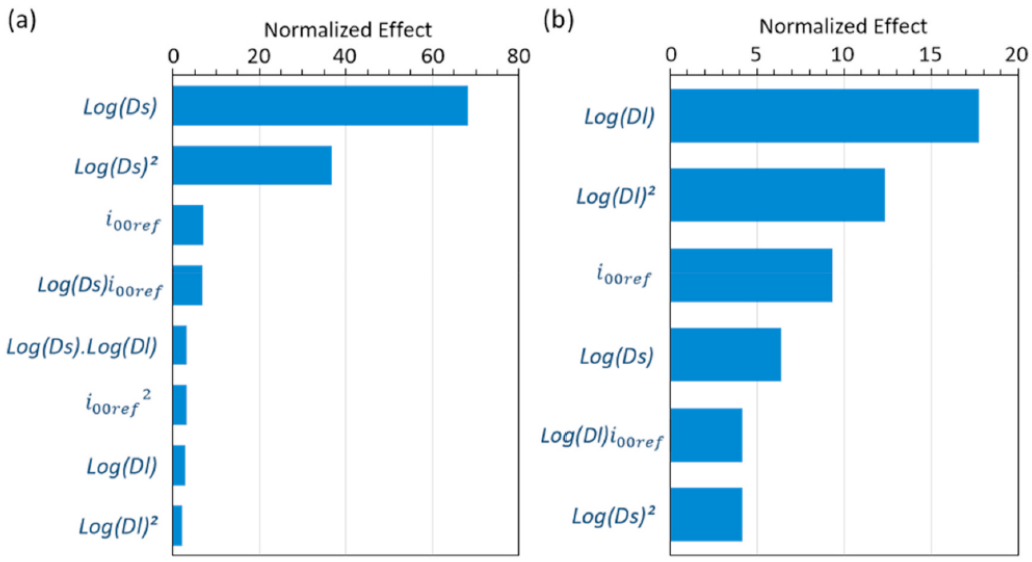

Figure 59 *Pareto diagram of the principal effects over the response in (a) local lithiation heterogeneities and (b) global lithiation heterogeneities. Local heterogeneities were dominated by the solid diffusion followed by its quadratic effect. About global heterogeneities, there was a more balanced influence among the parameters with liquid diffusion and its quadratic term at first and second position, respectively. Adapted and reprinted with permission from [30].*

At the end, with the use of Minitab18 software, the optimization of the discharge capacity with the lowest local lithiation heterogeneities (first case) and global (second case) was obtained. In both cases the predicted ranges of values were really close to the obtained values. The relative error was never larger than 6%, thus reflecting the effectiveness of the model.

Optimization for maximum specific energy density of a lithium-ion battery using progressive quadratic response surface method and design of experiments

The design of Li-ion batteries through experiments is almost difficult because the relationship between design variables and performances is not linear. The use of numerical models is a way to overcome this kind of difficulties. Among them, progressive quadratic response surface method (PQRSM) is one of the sequential approximate optimization (SAO) techniques that does not need gradient-based calculations. The use of a trust region algorithm to guarantee weak global convergence and a relatively low number of calculations needed for optimal results make PQRSM a very effective method. Kim *et al.* conducted a study with the use of DoE to analyze the sensitivity of eight cell design factors: anode, cathode and separator thickness; anode, cathode and separator porosity; anode and cathode particle size [31]. The PQRSM was applied as optimization algorithm to maximize the specific energy density of LIB and then the initial and optimized cells were compared. 4-level orthogonal array was used to define sampling points in the design space. A correlation analysis was performed to investigate the linear relationship between the cell design factors and specific energy and power density with the aim of exclude the factors with an apparent linear relationship. This because the optimal value was at the boundary of the design space. ***Figure 60*** shows the relationships of specific energy density with the thickness and porosity of the anode and cathode for 96 sampling points.

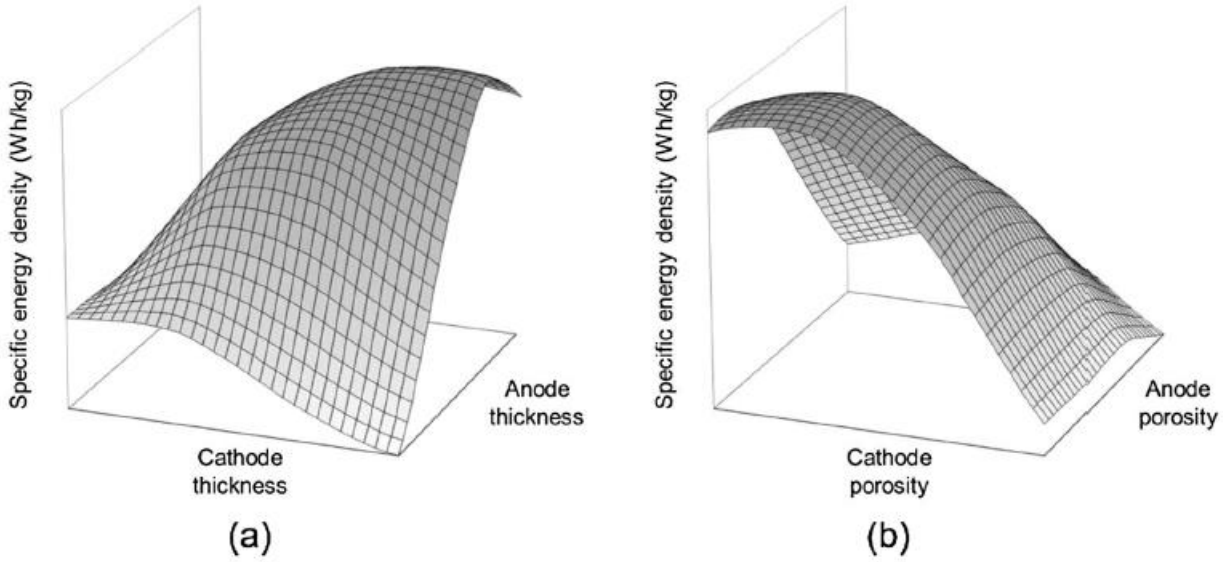

Figure 60 *Cathode and anode thickness and porosity relationships with specific energy density at 96 sampling points derived from the 4-level orthogonal arrays. High specific energy density can be achieved at a certain thickness ratio of the anode and the cathode. As for thickness also porosity is related to the amount of active material inside the cell. Adapted and reprinted with permission from [31].*

ANOVA was conducted to determine the design variables for the optimization. Factors with a P-value less than 0.05 were selected: cathode, anode and separator thicknesses and porosities of cathode and anode.

PQRSM optimization process was applied and generated a full quadratic response surface model. The process is schematized in ***Figure 61***. The battery cell was subjected to a constant current discharge at a rate of 1C with a cutoff voltage of 3.0 V.

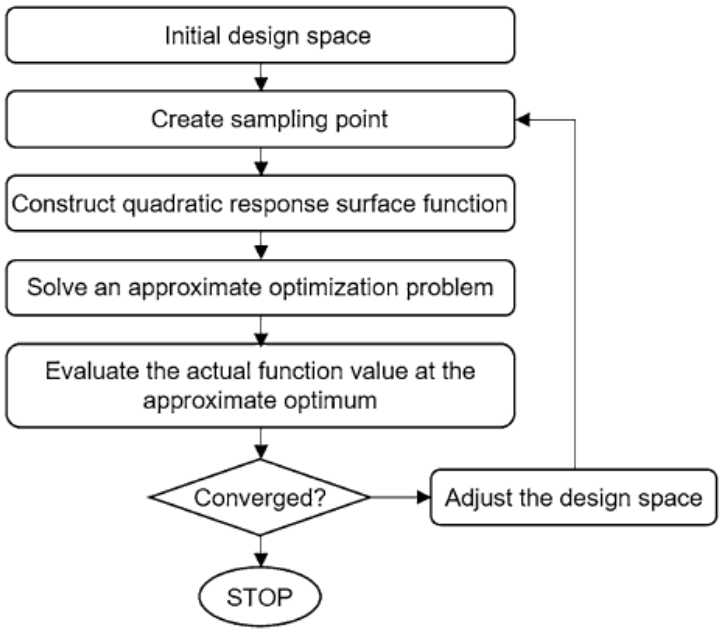

Figure 61 *Flowchart of PQRSM process. The algorithm generated a full quadratic response surface model. Each iteration with 2n+1 sampling points generated the quadratic response surface model, and the approximate optimization was conducted in the initial trust region. Then the actual function value was calculated from the approximate optimum and the convergence criteria were evaluated. The procedure was repeated until the convergence. Adapted and reprinted with permission from [31].*

General results are shown in ***Figure 62***. The DoE analysis proved to be relevant in studying how to optimize the LIB cells in terms of specific energy density. Also, the polarization phenomenon was reduced by 11.5%.

Further analysis should be done to investigate the affections of these configurations on cycling stability and life cycle of LIBs. To do this, degradation models made with the application of DoE would be effective.

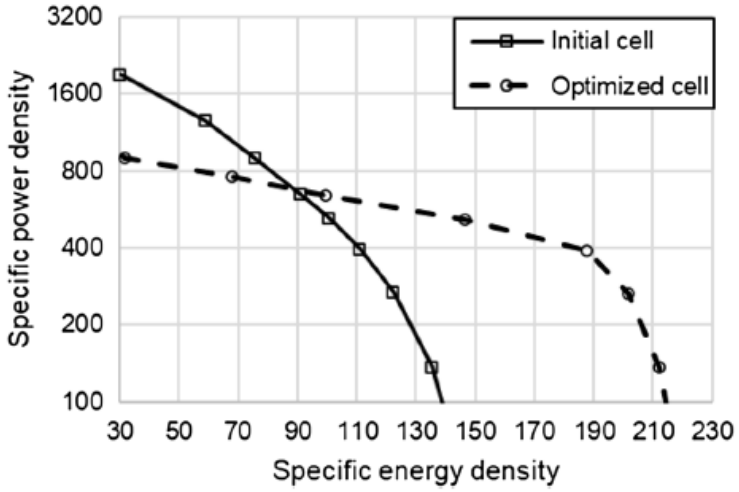

Figure 62 *Specific energy density versus specific power density of initial and optimized cell. At a specific power density of 600 W/kg and below, the optimized cell had a higher specific energy density resulting in an improving of 56% with respect to the initial cell. Adapted and reprinted with permission from [31].*

Parameter optimization and yield prediction of cathode coating separation process for direct recycling of end-of-life lithium-ion batteries

Recycling end-of-life (EOL) Li-ion batteries is necessary because of a series of factors that are: i) the increasing demand of LIBs for EVs; ii) the serious environmental risks of the electrolyte salt (e.g., lithium hexafluorophosphate); iii) the efficiency of the recycling process compared to the extraction one. In the framework of the recycling methods, and specifically of direct recycling one which involves physical and chemical separation phases, Liurui Li *et al.* developed a novel presorting process [32]. It focused on the organic solvent extraction method with the aim of evaluating the cathode material retrieval yield by properly changing the processing parameters. The analysis was done using Taguchi DoE method and regression analysis. During the organic solvent extraction process, the binders (commonly polyvinylidene fluoride, PVDF) are dissolved in organic solvents (dimethylacetamide, DMAC, and dimethylformamide, DMF, were found as the most efficient) through soaking and sonication processes conducted at high temperature. The yield of the cathode retrieved material was estimated as the difference in weight of cathodes before ($W_{initial}$) and after (W_{post}) soaking and sonication as follows:

$$Yield = \frac{W_{initial} - W_{post}}{W_{initial}\, x\, 0.72}$$

considering that weight of cathode electrodes ($W_{initial}$) consists of 28% Al current collector and 72% cathode coating. In order to define the control factors, a 5 factor 2 level Placket-Burman screening experiment was performed. It needed 12 runs instead of 32 required by a complete factorial design. Each run was repeated 5 times with a randomly selected cathode sheet. The records were tested with ANOVA to determine the significance of each factor. The insignificant factors were taken out of the Taguchi experimental design. The most significant resulted to be: i) sonication time; ii) sheet size; iii) solid-liquid weight ratio. Taguchi method was then applied to select subsets of 3 control factors at 4 levels. To verify the performance characteristics of the Taguchi method, a continuous quality loss function was used. The loss function calculates the deviation of a design parameter from the desired value which is called the signal-to-noise (S/N) ratio. In the case of yield which was expected to be the highest possible, the equation was:

$$\mathrm{S/N} = -10\ x\ \log(\sum(1/y_i^2)/n)$$

with y_i the response of the i_{th} run and *n* the total number of runs. Results are shown in ***Figure 63***.

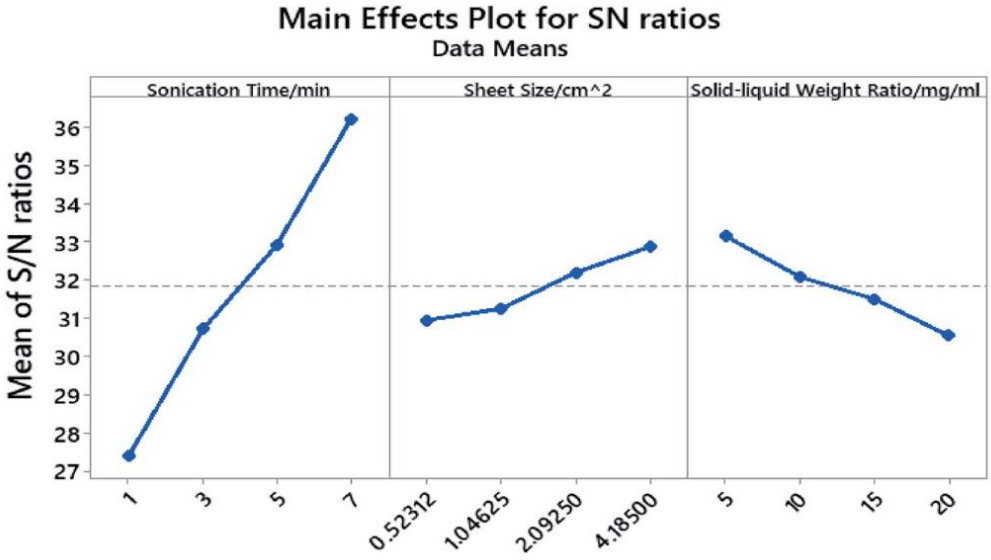

Figure 63 *Main effects plot for S/N ratios in Taguchi experiment. Adapted and reprinted with permission from [32].*

ANOVA was applied to S/N and individual contribution ($P_i\%$) of each factor was calculated as follows:

$$P_i\% = \frac{S_{eq}\,SS_i}{S_{eq}\,SS_{total}}$$

with $S_{eq}\,SS_i$ the sequential sum of squares of i_{th} factor and $S_{eq}\,SS_{total}$ the sequential sum of squares of all factors. Results showed the sonication has the highest contribution of 86.55%, followed by solid-liquid weight ratio at 7.44% and sheet size at 4.90%.

Percolation–tunneling modeling for the study of the electric conductivity in $LiFePO_4$ based Li-ion battery cathodes

$LiFePO_4$ has been recently investigated as positive active material (AM) in substitution of the expensive conventional $LiCoO_2$ due to its high theoretical capacity and stability, and low cost and toxicity. On the other hand, $LiFePO_4$ suffers from low Li ionic diffusivity and electric conductivity that imply high overpotential and limited high-rate vehicle performances. Awarke *et al.* applied DoE methodology to generate a model to capture the effects of AM particle size, carbon black (CB) wt% and carbon nano-coat (CNC) wt% on $LiFePO_4$ conductivity [33]. The use of nanosized particles resulted in shorter diffusion distances; moreover, the addition of conductive particles as carbon black and of a carbon coating on $LiFePO_4$ particles surface favored the improvement of overall conductivity. A tunneling-percolation theory was assumed to model the effective electric conductivity of a $LiFePO_4$ based Li-ion cathode. Below a percolation threshold, the effective electric conductivity was low and equivalent to insulating media, but above the percolation threshold the conductivity became good. The new effective conductivity was yet several orders less than that of carbon black due to the presence of an insulating binding polymer layer, that generally separates the conductive aggregates but at the same time is permeable to electrons through the so-called tunneling effect. Based on tunneling studies for carbon-polymer composites, a representative volume element (RVE) was considered, and the particle scale was used. The model was firstly validated by a series of measurements performed on a PVDF-CB composite at different volume ratios as reported in ***Figure 64***. Then a full factorial DoE was adopted to capture the variation of conductivity with three factors: i) nano-AM particle size; ii) CB particle

wt%; iii) carbon nano-coat (CNC) wt%. Three equidistant levels for the AM particle size (50, 100, and 200 nm) and for the carbon coating wt% (0, 1, 3) were defined. Four levels for CB wt% (0, 5, 10, 15) were identified resulting in 36 runs; the conductivities calculated from the 36 experiments are charted in ***Figure 65***.

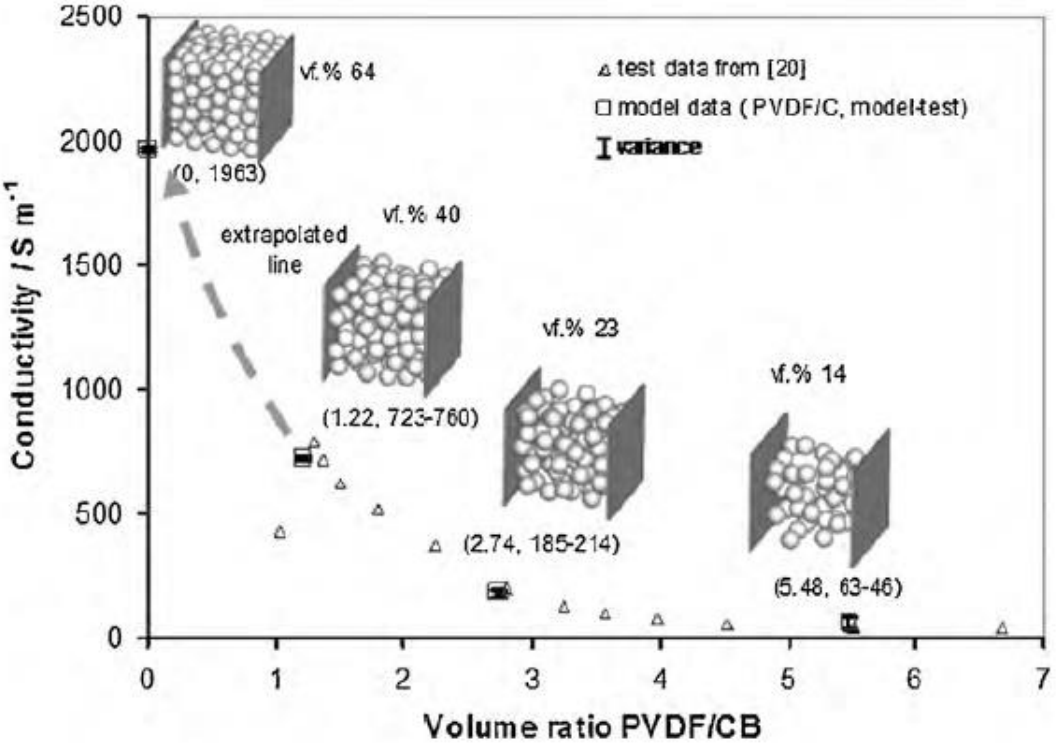

Figure 64 *Test and model conductivity data as a function of PVDF/C volume ratio. Adapted and reprinted with permission from [33].*

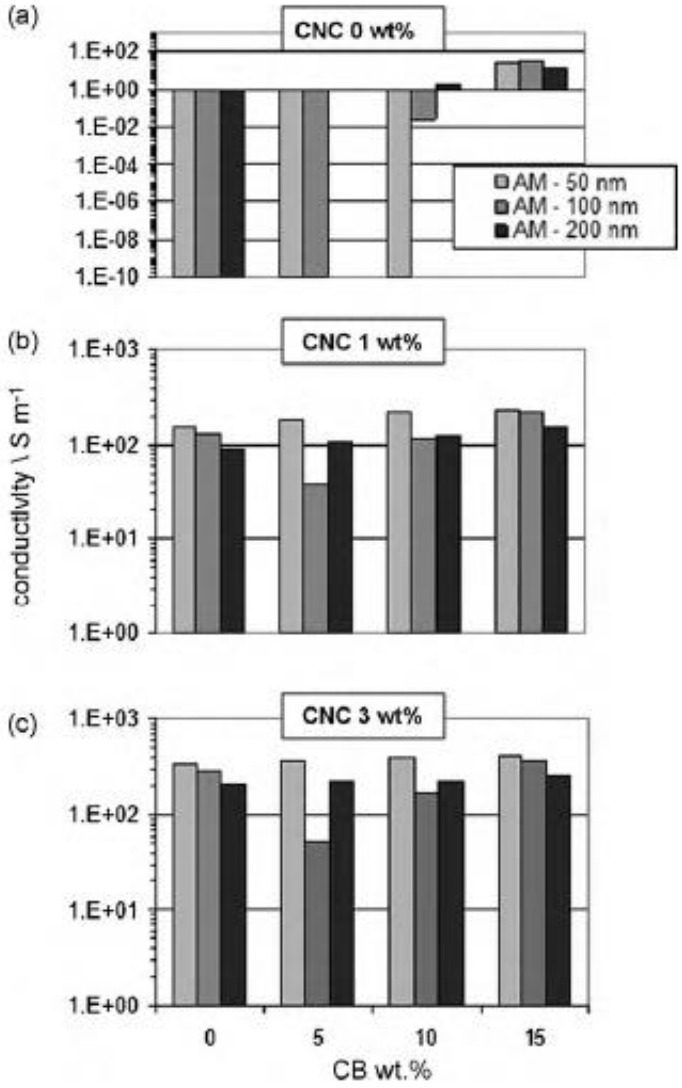

Figure 65 *Bar chart of achieved conductivities. In the case of bare AM, particle size became predominant with percolation of CB reached only with 15 CB wt% for 50 nm AM size. With larger size (100 nm) percolation was achieved already with 10 CB wt%. CB wt% was the only conductivity deciding factor. Adding CNC led to a suitable conductivity already with 1 wt% and in absence of CB addition. This because a conductive phase surrounding the AM formed an interconnected network. Increasing the thickness of the coat did not bring a drastic improvement of the conductivity. Adapted and reprinted with permission from [33].*

Using design of experiments in synthesis of ultra-fine copper particles by electrolysis

Copper powders are widely used in batteries and fuel cells due to their high electrical and thermal conductivities. A way to produce fine and ultra-fine copper of high purity is electrolysis, which is one of the most valuable methods because of its low energy consumption, ease of control and implementation. It is based on 2 steps: i) nucleation; ii) growth. The best way to produce fine copper particles is to control the relative rates of nucleation and crystal growth. Rasoul Khayyam Nekouei *et al.* applied DoE with electrolysis to produce fine copper powders from acid sulfate solutions [34]. Four parameters were studied to optimize the process in terms of purity, current efficiency and morphology of copper powders: i) current density; ii) copper ion concentration [Cu^{2+}]; iii) sulfuric acid concentration [H_2SO_4]; iv) chloride ion concentration [Cl^-]. Nonregular fractional factorial design was applied instead of a full factorial experiment to reduce the number of runs to 15. Three levels for each parameter were properly selected as shown in ***Table 7***:

Table 7 *Selected parameters and their levels.*

Factor	Unit	Low (-)	Center	High (+)
Current density (A)	A/cm^2	0.25	0.30	0.35
$[Cl^-]$ (B)	ppm	0	30	60
$[H_2SO_4]$ (C)	gr/L	140	160	180
$[Cu^2]$ (D)	gr/L	2	5	8

The experiments were realized using two copper plates with a purity greater than 99.5% as anode and cathode immerged in the electrolyte bath at a constant distance of 5 cm in between after being washed with acetone and grinded with sandpaper. Each test was conducted twice for 5 min at a temperature of 50° C. According to the analysis of variance (ANOVA), 4 essential effects and 2 interactions were selected for modelling: i) current density with $[H_2SO_4]$, ii) $[Cl^-]$ with $[H_2SO_4]$. The contribution of other interactions was very low. A first-order linear polynomial model was defined as follows:

$$Y = b_0 + \sum b_i X_i + \sum b_{ij} X_i X_j + \varepsilon$$

with b_0 the mean of responses of all the experiments, b_i the coefficient representing the effect of the variable X_i, b_{ij} the coefficient representing the effect of the interaction of variables $X_i$and X_j, ε the experimental error.

The equation became:

$$\log\left(particle\ size\ (\mu m)\right) = 2.95143 - 12.60384\ x\ A + 0.018204\ x\ B - 0.015187\ x\ C + 0.00799\ x\ D + 0.069114\ x\ A\ x\ C - 0.000104\ x\ B\ x\ C$$

The most influential parameter was the current density: as it increased, the grain size of the deposit decreased. A higher value of $[Cu^2]$ led to adherent deposit and, consequently, to a coarser particle size. Moreover, the presence of the chloride $[Cl^-]$ was ineffective on the particle size. Also, the increase of $[H_2SO_4]$ had a negative effect on the particle size. The effects of single parameter and the main interactions are reported in ***Figure 66*.**

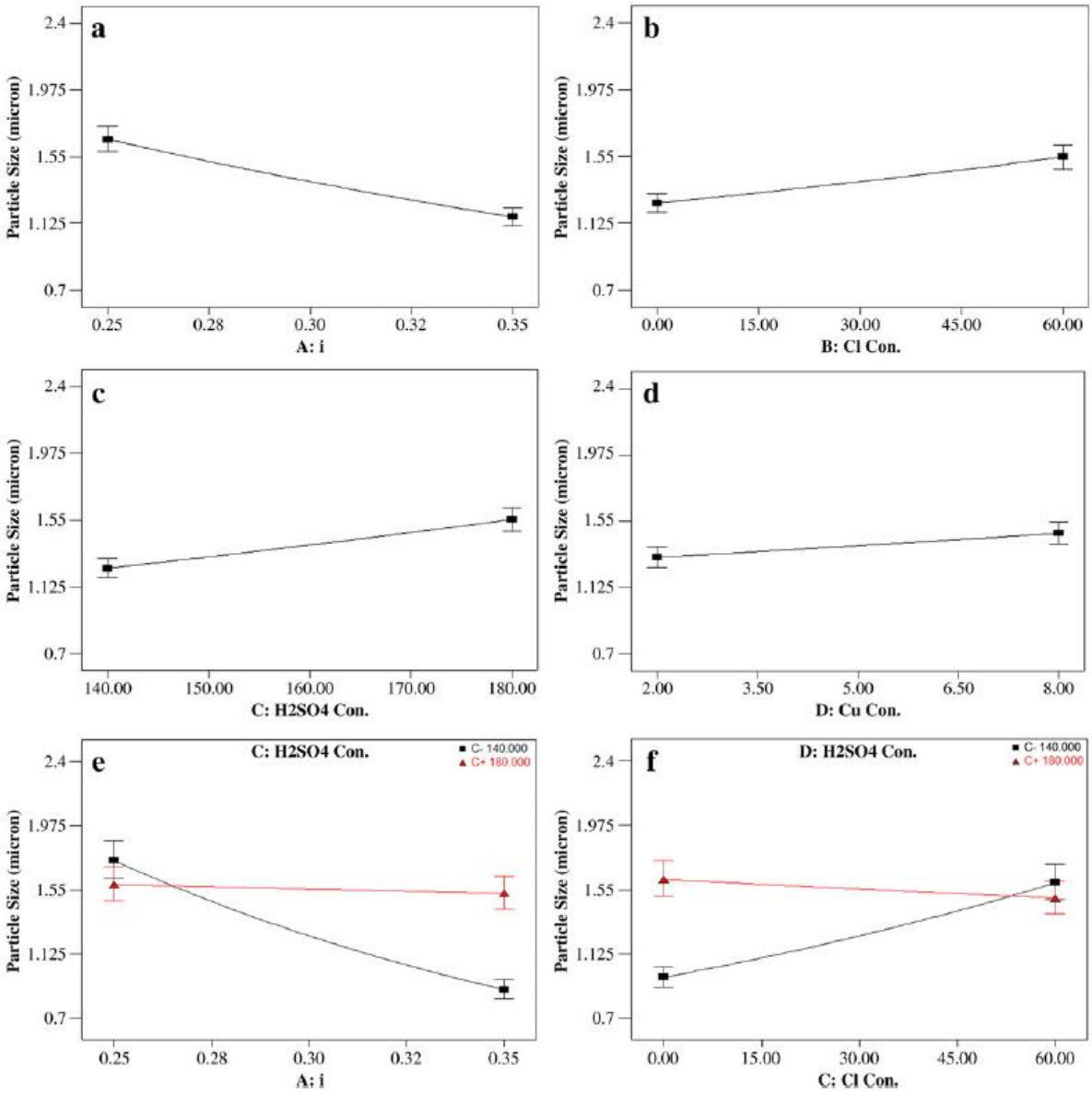

Figure 66 *Interaction of current density with [H_2SO_4]. Adapted and reprinted with permission from [34].*

According to the chemical process and the experiments, overvoltage varied between 1 and 2.2 V. With the increase of the overvoltage also the powder became finer, but the hydrogen evolution occurred diminishing the current efficiency.

Finally, a confirmation test was performed at the optimized parameters according to the model. The particle size predicted was 0.71 µm and the actual experimental result was 0.68 µm. The model was acceptable.

Section 2.4: DoE for Battery Safety and Management

A comprehensive and time efficient characterization of redox flow batteries through Design of Experiments

Energy transition leads toward new challenges. The need to store energy becomes fundamental; in this scenario, batteries and all the systems dealing with the storage of energy resulted to be crucial due to the unpredictability of the renewable energy sources. Li-ion batteries experienced a great spread among this market, but other systems became of great interest. Redox flow batteries (RFBs) are recently emerging as a valid alternative. ***Figure 67*** shows the working principle of the RFBs. They are subjected to a characterization process which is composed of a large number of charge/discharge cycles to measure battery capacity and round trip efficiency (RTE). This procedure requires too much time. The implementation of a method to model the RFP performances with a limited set of factors and through the use of DoE methodology was investigated by Delbeke *et al.* [35].

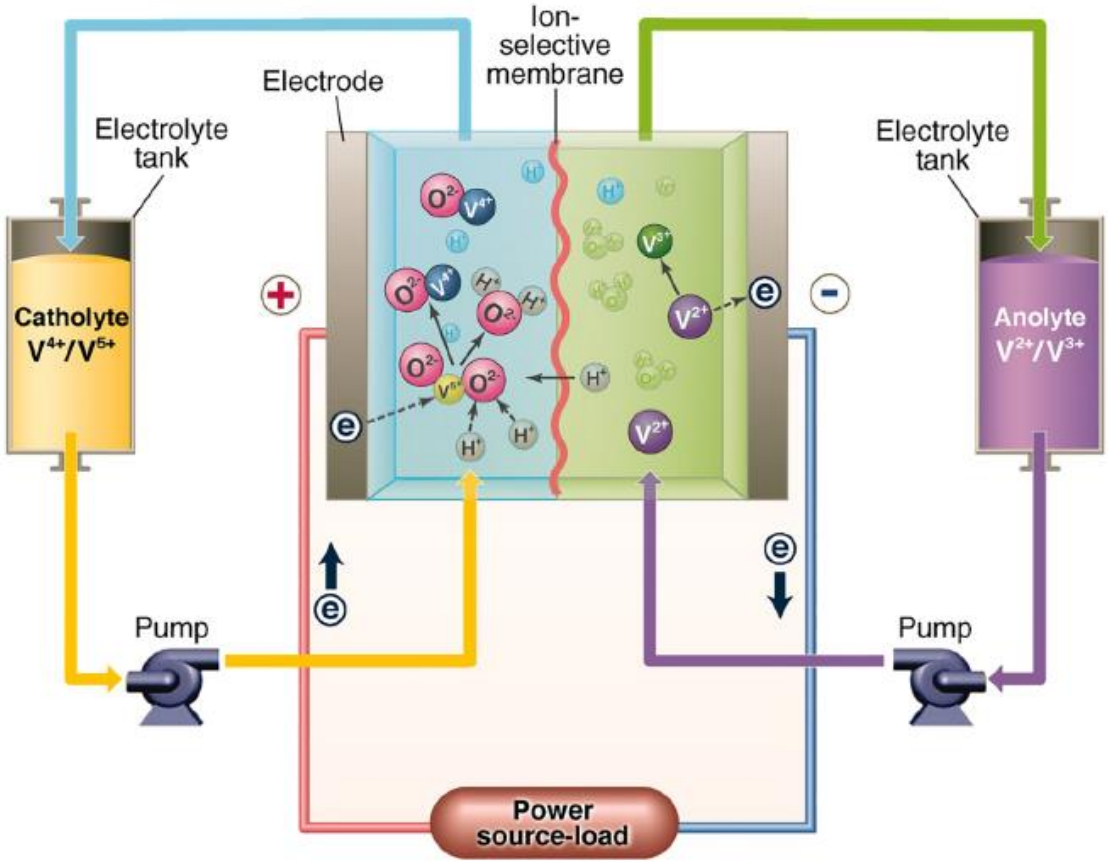

Figure 67 *Redox flow battery working principle. Two half-cells circulate an electrolyte in which the active species are stored. Ions move through an ion-selective membrane from an electrolyte to the other, while electrons move through an external circuit. Adapted and reprinted with permission from [35].*

The study was based on two basic principles: the Pareto principle, which declares that any real process is mostly driven by limited number of important factors, and the Taylor's theorem, which states that any function can be approximated by a polynomial (of first, second or higher order) in a sufficiently small area. Various parameters influenced the battery performance (***Figure 68***), but some of them couldn't be controlled by RFB operators so they were discarded from the DoE. The chosen RFB output parameters were the DC discharge capacity and the DC RTE as follows:

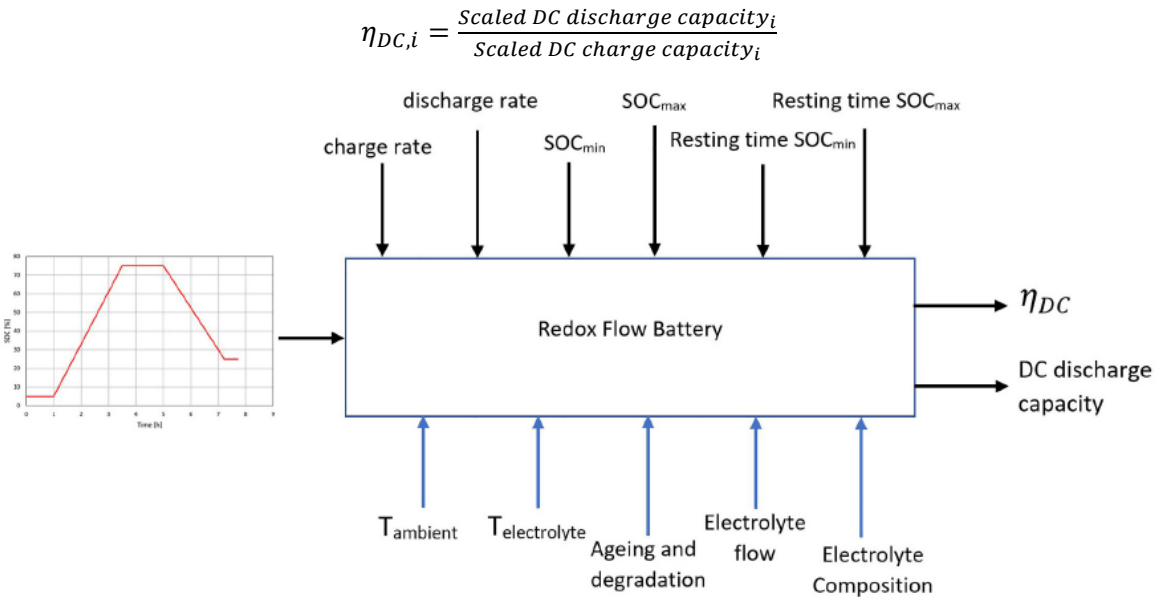

Figure 68 *Redox flow battery system parameters. Inputs, on the left, translate to charge/discharge cycles for the RFB. The effects of a number of controllable parameters (on top of the box) were studied on the system outputs (on the right box), but also other parameters (below the box) which are uncontrollable likely affected the outputs anyway. Adapted and reprinted with permission from [35].*

DoE was applied as follows: first of all, 4 experiments were conducted on the single RFB module using D-optimal design scheme to identify the most influential controllable parameters in the system. This set of experiments included 4 of 6 controllable parameters: i) charge rate; ii) discharge rate; iii) minimum SOC; iv) maximum SOC. Among them, the most dominant turned out to be charge and discharge rate. Electrolyte temperature, which was uncontrollable but easy to measure, had a high influence on the process. A second set of experiments was run with the same controllable parameters of the first set but adding an I-optimal extension to study the potential improvement of the models. The change in R^2 resulted negligible. The third set of experiments was focused on founding a way to properly quantify the influence of the temperature on the battery performance. Resting time was varied to let the electrolyte to cool off. The adopted range was 15 to 720 min. The resting time at maximum SOC was detected as statistically consistent parameter for predicting DC efficiency and DC discharge capacity. Based on the insights of the previous designs, the most influential controllable parameters were identified, and a corresponding orthogonal characterization experiment could be conducted with a reduced time of 6.5 days with respect to nearly 13 days of classical characterization experiments.

A novel disassembly process of end-of-life lithium-ion batteries enhanced by online sensing and machine learning techniques

End-of-life batteries need to be disassembled to recycle and reclaim the materials for both environmental and economical sustainability. Automatic disassembly is important to make the process more precise and faster but also to avoid health effects on workers who would be exposed to toxic substances. Machine learning was an approach that was used to improve the process. It was based on cyber physical system (CPS), which allows to achieve collaborative interaction between computational and physical processes. Optimization of parameters is fundamental to further improve the system. First step of the process was to recognize the battery in terms of brand and dimensions to set the cutting machine. Another necessity was to monitor the temperature to prevent the spike. After cutting, quality verification was assured by the computer vision. The deep learning technique adopted by Lu *et al.* was the Convolutional Neural Network (CNN) for classification and cutting quality control and long short-term memory for temperature spike prediction [36]. To derive the control rules of deep learning tools, DoE was used. Focusing on cutting

process, different parameters influenced the maximum cutting temperature: i) cutting speed; ii) feed rate; ii) blade tooth density. Each factor was considered at low and high values. Main and interaction effects were calculated and then ANOVA was applied. As a result, it was demonstrated that it was necessary to reduce cutting speed and blade tooth density but, at the same time, feed rate had to be controlled through an optimized strategy to compensate the lost in efficiency and safety caused by the minimalization of the other two factors.

Development of cooling strategy for an air-cooled lithium-ion battery pack

Analytical DoE was applied by Hongguang Sun and Regan Dixon to study the effects of cooling strategies on a battery pack [37]. The objective was to identify the optimal configuration and geometry of cooling ducts, plates and control modules to maximize battery pack capacity and durability [37]. To do that, a transient three-dimensional battery pack thermal model was developed by including a three-dimensional battery pack flow sub-model, one-dimensional battery pack network sub-model, and transient three-dimensional battery cell/module thermal sub-model. Consequently, the thermal model was correlated with physical tests and DoE permitted to find the cooling strategy to minimize battery cell lumped temperature, battery cell temperature variation across the pack and total pressure drop. The simulation process is illustrated in ***Figure 69***.

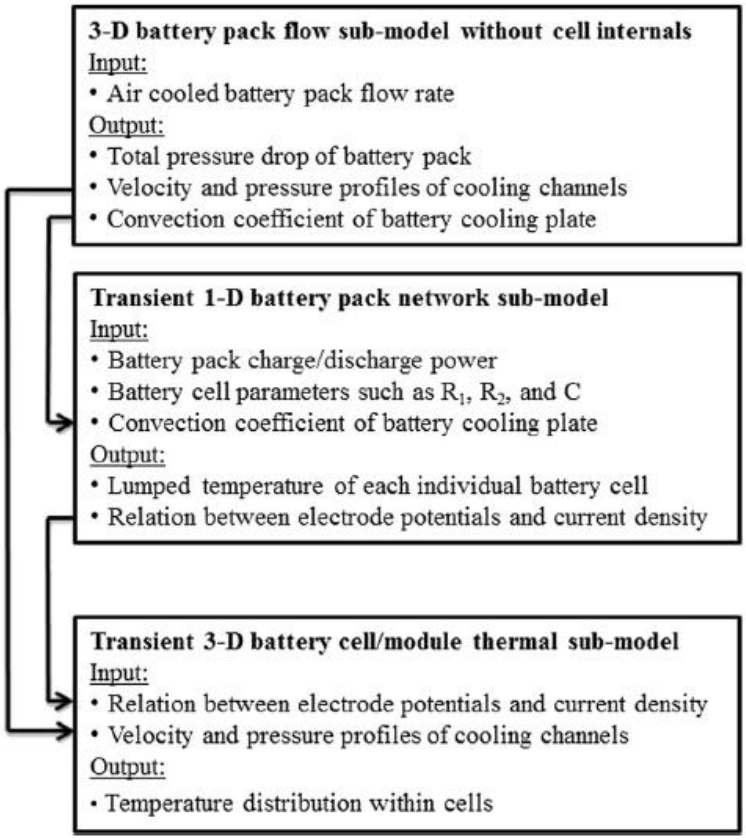

Figure 69 *Simulation process: the total pressure drop of battery pack, the lumped convection heat transfer coefficient of each individual cooling plate and velocity and pressure profiles at the inlet and outlet of individual cooling channels were calculated in the steady state three-dimensional battery pack flow sub-model. The convection coefficient of battery cooling plate was then used as input parameter to calculate the individual battery cell transient lumped temperatures and the variation of lumped cell temperature across the pack under different charge/discharge cycle with one-dimensional battery pack network sub-model. Finally, the three-dimensional battery cell/module thermal sub-model with the input of the transient battery cell heat generation rate based on electrode potentials and the relation between electrode potentials and current density were used to estimate the temperature distribution within battery cells. Adapted and reprinted with permission from [37].*

The design space for each design factor was uniformly divided and combined to generate the first design matrix using Latin-hypercube technique. Then, an optimization process was applied to design an optimal design matrix which uniformly contains the design points. The modified battery pack flow sub-model was run and successively the one-dimensional battery pack network sub-model too. Thus, lumped cell temperature, cell temperature variation across the pack and total pressure drop were memorized into output arrays which were used for the next simulation. Then Response Surface Approximation based on a fourth order polynomial fit was used to approximate thermal behavior of additional design points. The model was then validated by running a series of physical tests on a "U-type cooled" battery pack. Results were in agreement with the model with a maximum deviation of the predicted transient temperature between the simulation and physical test of less than 0.5 °C. Next step was the investigation of cooling duct geometry. "Z-type" cooling duct was investigated with cool air insulated from the upper channel and exited from the opposite side of the bottom channel. This configuration was resulted in a great disparity of flow rate between inlet side and outlet side. To improve this, cross-section of the channels was varied along the battery pack to uniform the pressure drop of inlet and outlet sides. The height of the inlet and outlet and the heights of closed ends of upper and lower ducts were defined as design factors for DoE. By reducing the closed ends of upper and lower ducts and increasing the inlet and outlet ends the lumped temperature variation across the pack was reduced as desirable. ***Figure 70*** shows the schematic of optimal "Z-type" flow battery pack. In this way the lumped cell temperature variation across the modified battery pack was reduced from 10.8 °C (conventional "Z-type" flow battery pack) to 3.6 °C.

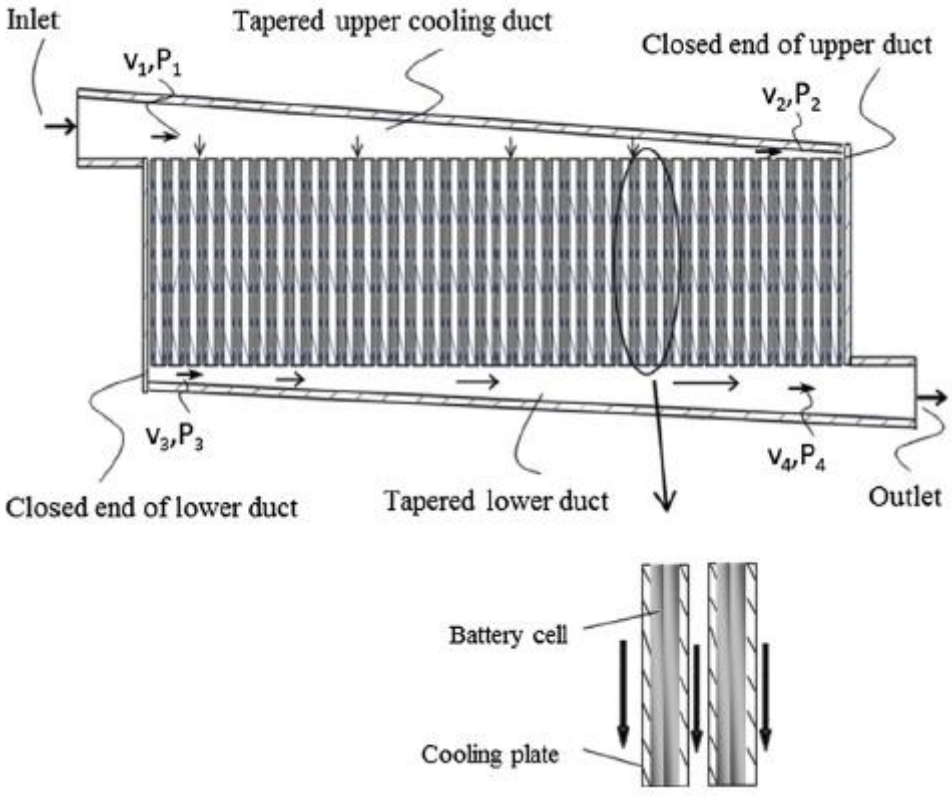

Figure 70 *Optimal "Z-type" flow battery pack with tapered cooling ducts. The pressure drop was drastically reduced and the cooling fluid flow rate was consequently more uniform. Adapted and reprinted with permission from [37].*

Experiment-driven electrochemical modeling and systematic parameterization for a lithium-ion battery cell

Charge/discharge process generates heat due to mainly ohmic losses leading to self-heating phenomenon generated by the movement of the ions into the cell, as described in ***Figure 71***. State of charge, terminal

voltage and temperature must be predicted and monitored for safety and lifetime requirements on electrical energy storage technology. Initially, single-particle (SP) approach was used. A new and easy-to-handle lumped parameter model was investigated by Schmidt *et al.* to better reproduce input/output behavior of a commercially available lithium-ion cell [38].

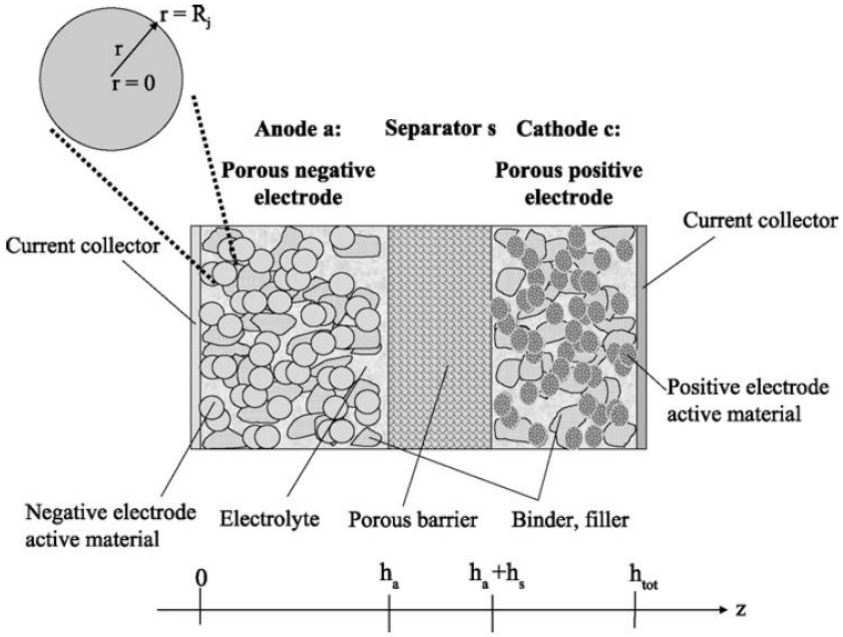

Figure 71 *Schematic drawing of a lithium-ion dual intercalation cell. The two electrically separated porous electrodes (anode and cathode) consist of a structure made of quasi-spheric active particles with typical diameters of µm scale. Lithium ions are collected in vacant sites of the crystal structure of the particles. The terminal voltage is determined by the difference in potential of the two electrodes. Lithium ions are transported by diffusion inside the particles and then through the particle-electrolyte interface and the electrons (which are initially transported by lithium-ions) are transported to the current collectors. Then lithium ions travel via diffusion and migration through the separator, made of porous material, to the backplate electrode. Adapted and reprinted with permission from [38].*

A small set of experiments was chosen which was sufficient to the whole operating range of the device. This was obtained thanks to the application of a DoE. By effectively analyzing and identifying the parameters in the model and by combining different methods such as the Fisher-information matrix technique along with sensitivity analysis, they estimated how each parameter can be identified based on the available measurement data. With this approach, they selected a few key experiments that were enough to fully define the model's parameters.

Improved performance of Li-ion Polymer batteries through improved pulse charging algorithm

Battery charging is an imperative topic of research. Improving battery charging means increased battery charge, energy efficiencies, life cycle and, at the same time, reduced charge time but also the possibility to avoid thermal runway. Li-ion polymer (LiPo) batteries, which are constituted of gel-like polymer electrolytes (instead of Li-ion batteries that uses liquid electrolyte), have stringent charging algorithms. The most known and used is the constant current-constant voltage (CC-CV). Pulse charging algorithm can improve the battery charging phase involving the use of charge current pulses. In ***Figure 72*** CC-CV and pulse charging algorithms are schematized. The use of pulse charging algorithm ensures that the Li ions electrochemically produced during each pulse migrate from the cathode to the anode and successfully intercalate without accumulation on the electrode surface of the ions produced by the successive pulse.

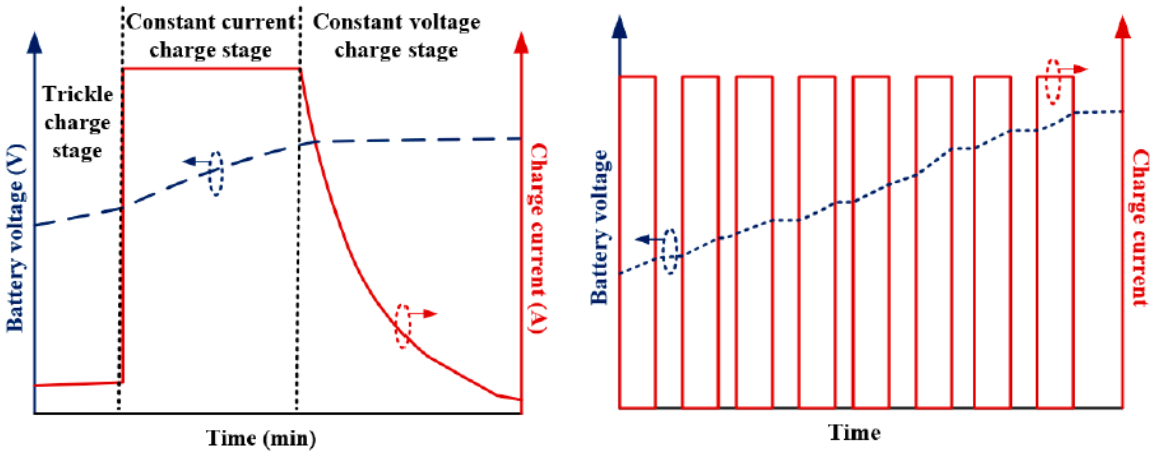

Figure 72 *On the left: constant current-constant voltage (CC-CV) charging algorithm schematic illustration. Three phases are involved: i) trickle charging phase consisting in a small charge current (1 to 10%) when the battery is significantly discharged; ii) constant current charge stage with a current range between 50 to 320% of the full rated charge current; iii) constant voltage charge stage where a decreasing charge current is used to prevent overcharge and overvoltage conditions. On the right: typical schematization of a pulse charging algorithm. This prevents Li^+ accumulation on the surface and contributes to the mitigation of dendrite formation. Adapted and reprinted with permission from [39].*

The significant parameters to control every pulse are specified in the following equation:

$$I_{avg} = I_{peak} * f * T_{on}$$

with f the frequency, I_{peak} the peak charge current amplitude, T_{on} the time the battery is being charged and I_{avg} the average charge current. The investigation of the best combination of these parameters can be performed with orthogonal arrays (OA), which allow at the same time to reduce the number of experiments and to get comparable results to fully factorial design. The chosen parameters were duty cycle of the pulses *D*, frequency, and the ambient temperature at which the battery was charged. The levels are represented in ***Figure 73***. The outputs were defined as charging time, battery charge and energy efficiencies. According to parameters and levels, the OA row size was defined to be 36.

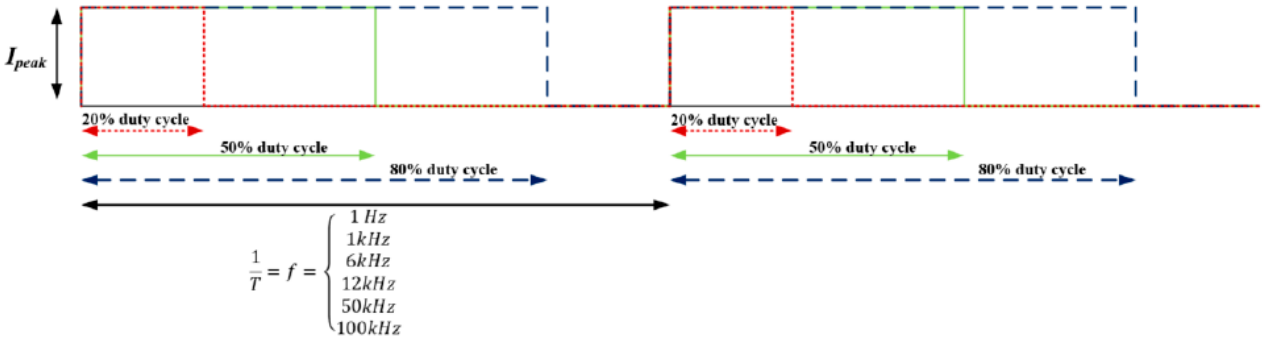

Figure 73 *Key parameters which have to be carefully defined for a successful implementation of the pulse charging are peak charge current amplitude, frequency and duty cycle. Adapted and reprinted with permission from [39].*

The obtained results were analyzed through analysis of variance and analysis of means. Frequency and duty cycle had the most impact on the battery performance. Moreover, a confirmation experiment was performed and compared with the benchmark constant current constant voltage charging algorithm. Pulse charge led to an improvement of 12% in battery energy efficiency, 2% in battery charge efficiency and to a 48% reduction in charging time. The impact of the peak amplitude of pulse charging current was also investigated and, even if the higher the peak, the faster the charging time, the peak charge current

amplitude has to be within the specification of the battery to avoid damages caused by the increase of the surface temperature of the battery. Referring to the life cycle, DoE was applied, more specifically a 36-row orthogonal array was constructed. At 23 °C both CC-CV charged battery and pulse charged battery revealed similar impedance values. Frequency and duty cycle had the greatest impact on life cycle. 12 kHz and 50% duty cycle were the best values leading to the lowest level of impedance which meant the highest conversion of input to stored energy and equal time allocated to anode and cathode reversal. This set associated with pulse charging allowed 100 more cycles with respect to the same set associated with CC-CV charging method. In this context the concept of smart charging becomes prevalent in order to improve the efficiency of the batteries and reduce their progressive decay.

Improving battery thermal behavior and consistency by optimizing structure and working parameter

A coupled electro-thermal model for an air-cooled pack was established by Xie *et al.* to better predict the temperature dynamics of an air-cooled battery back [40]. This is critical for the battery thermal management system (BTMS), which has the function of ensure the safety and efficiency of the battery pack. Previously, various cooling methods were experimented and applied, such as air cooling (the most common), liquid cooling, heat pipe. A current distribution model was defined to calculate the distribution of the branch current due to inhomogeneous cooling, then the model was coupled with the thermal one to improve the prediction of the heat production inside the cell. The battery consistency was integrated in the structure design and determination of operation parameter of the BTMS. Two DoEs were applied to optimize the air channel. Firstly, a full-factorial design was used to make the structure parameters cover the full optimization range and obtain the approximate location of the optimal solution. Secondly, the first DoE results were analyzed to determine the correct direction and the orthogonal DoE was employed to search the exact position of the optimal air channel structure. ***Figure 74*** shows the structure of the electro-thermal model of the air-cooling pack.

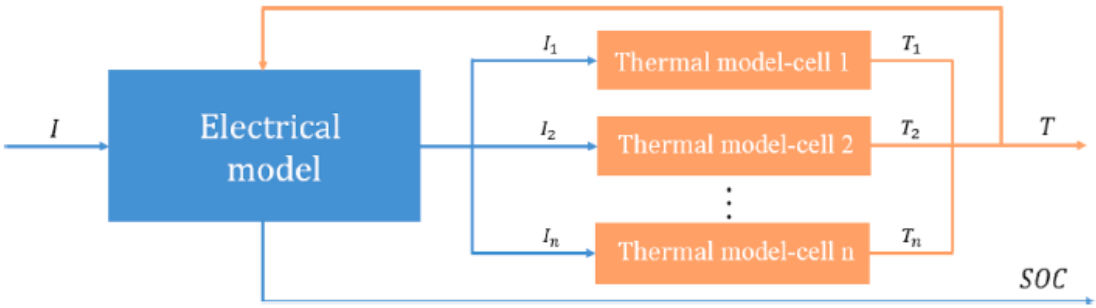

Figure 74 *Scheme of the electro-thermal model for the air-cooled pack. The electrical model calculates the current in the branch of the pack, the thermal model receives the value and calculates the cell temperature. The cell resistance is then updated according to the new temperature. The new cell resistance is sent to the electrical model to update the branch current and the cell SOC. Adapted and reprinted with permission from [40].*

The pack thermal model was solved through computational fluid dynamics (CFD) method: the velocity inlet was used for the air entrance and the pressure outlet for the air exit. The simulated terminal voltage showed similar evolution compared to the tested one. Also for the temperature, simulated one was similar to the tested. DoE was then used to optimize the distance (horizontal S_x and vertical S_y) between two cells to reduce the cell temperature and the temperature difference among cells. The process was divided into two phases. The first phase consisted in the application of a full factorial design to determine which distance (among S_x and S_y) had the most influence: S_x and S_y were defined as the two factors. The design diagram is represented in ***Figure 75***. Three levels were chosen within 21-26 mm due to installation space limitations. The range and variance analyses were performed. S_y was individuated as the most significant impact on cooling performance. The second DoE was applied to S_x, while S_y was fixed to 21 mm according to

the average SOC difference and maximum cell temperature lowest registered values. Three values of S_{x1}, S_{x2} and S_{x3} were chosen as the factors of the second DoE. The orthogonal experiment design was applied to obtain the representative cases and reduce the computation amount. The best case was found with S_{x1} = 21 mm, S_{x2} = 26 mm and S_{x3} = 26mm.

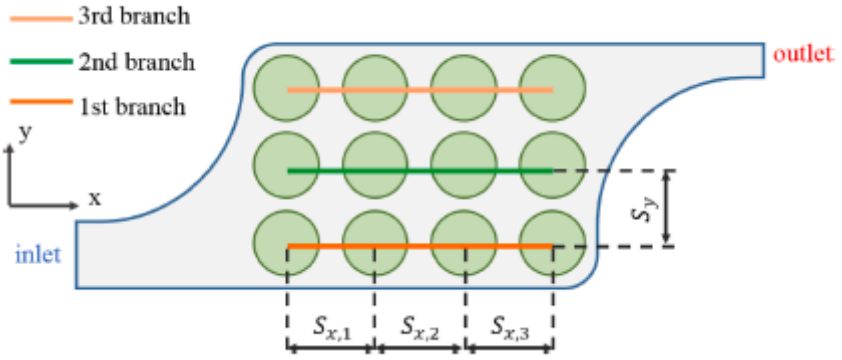

Figure 75 *Structural design diagram of the air-cooled pack. S_x and S_y were defined as factors of the first DoE. S_{x1}, S_{x2} and S_{x3} were defined as factors of the second DoE. Adapted and reprinted with permission from [40].*

The comparison between the cell temperature at the end of discharging of the original structure and of the optimized one is shown in ***Figure 76***.

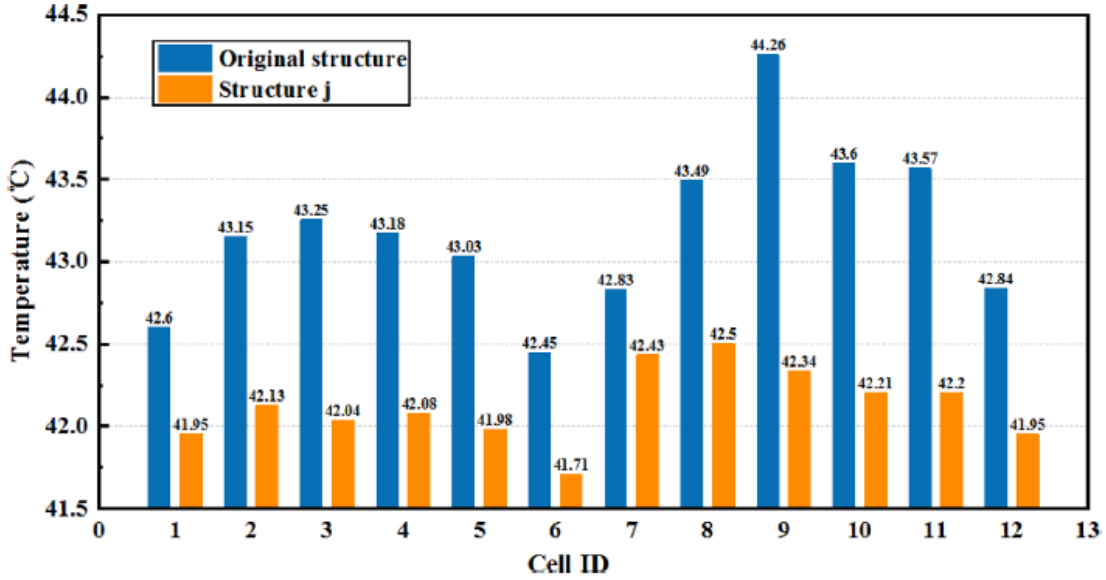

Figure 76 *Cell temperature at the end of discharging of the original and optimized structure of air channel. The maximum temperature resulted reduced for the optimized structure. Moreover, the temperature difference among cells was reduced. This brought to a reduction of the variation of the branch current leading to an improvement of the consistency among cells and to a reduction of the SOC difference of the cells constituting the pack. Adapted and reprinted with permission from [40].*

Modeling of the Lithium Calendering Process for Direct Contact Prelithiation of Lithium-Ion Batteries

LIBs suffer from initial capacity losses caused by the formation of solid electrolyte interphase (SEI). This effect consumes Li ions with the result of reducing the energy density and the life cycle. An approach to compensate this is the prelithiation, which consists in adding lithium to the cell before the first charge and discharge cycle of the formation process. To do this, Stumper *et al.* investigated a roll-to-roll process for direct prelithiation focusing on the compaction properties of the electrodes [41]. The process was realized by calendering of lithium foil until reaching target thicknesses. DoE was applied to analyze the process. As shown in ***Figure 77***, an empirical model first and a semi-analytical model then were used. Input variables were geometry and material characteristics while the output was the thickness and the new geometry of the foil after calendering.

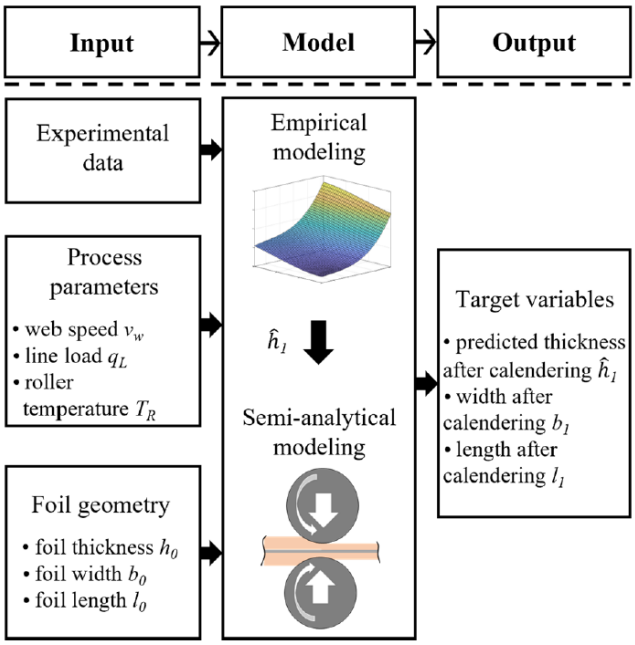

Figure 77 *Schematic structure of the process model for the calendering of Li foil. Adapted and reprinted with permission from [41].*

Experiments were performed using a lithium foil with 99.9% of purity. For the empirical model a full factorial DoE was carried out to define the range of values for each input parameter represented in the form of vectors. Various assumptions were made as follows:

- The lithium is isotropic, so its deformation does not depend on direction;
- Density of lithium does not change before and after calendering, so the volume constancy is valid;
- There is no relative sliding between lithium foil and the carrier foil and between the calenderer roller and the rolled material;
- The temperature distribution is uniform;
- No deformation of the carrier foil (made of copper) occurs due to the line loads applied.

Moreover, the web speed w_b, the input thickness of the Li foil and the temperature of the roller were kept constant and equal to 0.1 m/min, 50 µm and 20 °C, respectively.
A series of values for line loads were experimented, each of them constituting a component of the vector $\overrightarrow{q_L}$. With these conditions, the empirical model of the thickness h_1 according to the experimental data obtained at different line loads was defined as follows:

$$\widehat{h_1} = f(q_L) = k_1 q_L^3 + k_2 q_L^2 + k_3 q_L + k_4$$

To extend the analysis to the chosen parameters, a third-dimension factor space was used by linking the vector of the line loads $\overrightarrow{q_L}$ with the vector of $\overrightarrow{T_R}$. The equation of the empirical model became:

$$\widehat{h_1} = f(q_L, T_R) = k_1 + k_2 q_L + k_3 T_R + k_4 q_L^2 + k_5 q_L T_R + k_6 T_R^2 + k_7 q_L^3 + k_8 q_L^2 T_R + k_9 q_L T_R^2 + k_{10} T_R^3$$

Representations of two-factor and third-factor space for the vectors are reported in ***Figure 78*** and ***Figure 79***, respectively.

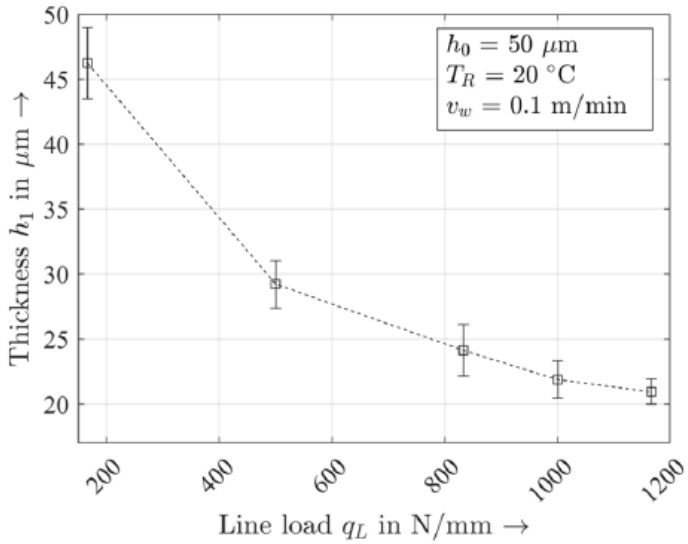

Figure 78 *Representation of two-dimensional factor space of the empirical model. Adapted and reprinted with permission from [41].*

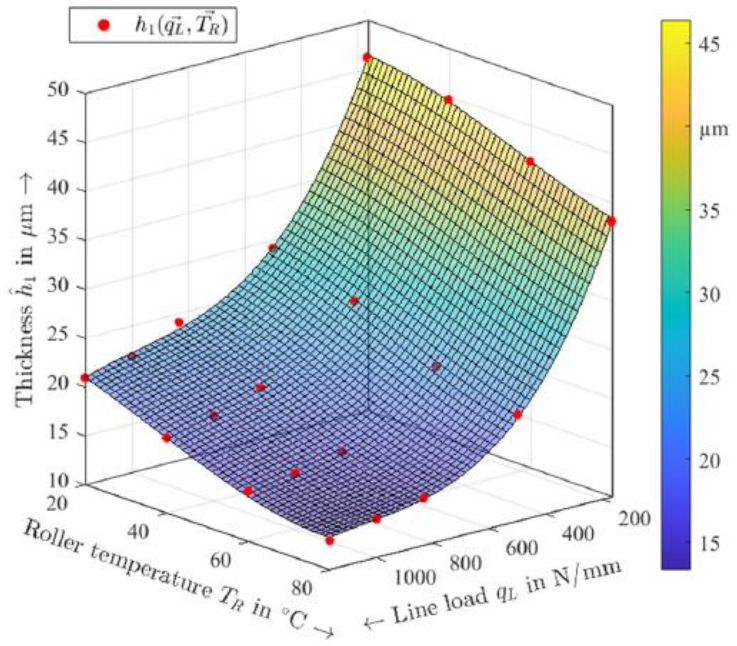

Figure 79 *Representation of three-dimensional factor space of the empirical model. Adapted and reprinted with permission from [41].*

In addition to the empirical model, a semi-analytical modelling was carried out to verify the length and the width of the foil after calendering. In ***Figure 80*** a cross-sectional view of the process is represented. Assuming that the volume remained the same before and after calendering, Roux equation was applied:

$$\Delta b = \frac{\Delta h \cdot \left(\frac{b_0}{h_0}\right)}{(1 + 0.57 \cdot B) \cdot \left[1 - \frac{\Delta h}{h_0} + \frac{3 \cdot A}{\left(2 \cdot \frac{r_r}{h_0}\right)^{\frac{3}{4}}}\right]}$$

with *A* and *B* constants calculated as:

$$A = \left(1 + 5 \cdot \left(0.35 - \frac{\Delta h}{h_0}\right)^2\right) \cdot \sqrt{\frac{h_0}{\Delta h} - 1}$$

and

$$B = \left(\frac{b_0}{h_0} - 1\right) \cdot \left(\frac{b_0}{h_0}\right)^{\frac{2}{3}}$$

The data calculated with the equation above offered a very good approximation of the data measured during the tests.

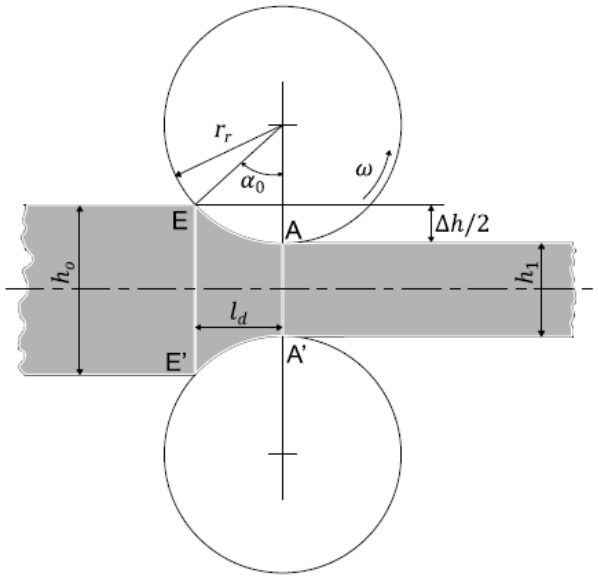

Figure 80 *Cross-sectional view of a schematical roll-to-roll calendering process. Adapted and reprinted with permission from [41].*

A validation of the empirical model was done by considering the residuals r in the three-dimensional space. For the largest residuum, the deviation was about 6.3% referred to the measured value. Regression coefficient was calculated to estimate the quality of the regression as follows:

$$R^2 = \frac{\sum_{i=1}^{20}\left(\hat{h}_{1_i} - \bar{h}_{1_i}\right)^2}{\sum_{i=1}^{20}\left(h_{1_i} - \bar{h}_{1_i}\right)^2}$$

A result of 0.99 was achieved, which confirmed the high quality of the proposed model.

Power Distribution Development and Optimization of Hybrid Energy Storage System

The series hybrid electric bus (SHEB) is an EV in which all the propulsion energy is produced by the electric machine and is characterized by a high power and energy demands. Commonly, the energy storage system (ESS) of EVs is battery due to its portability and low cost. The peak-to-average ratios for a common battery are between 0.5 to 2. An alternative to batteries is the ultra capacitor (UC), which has good life cycle and peak-to-average ratios of 10 to 12. Use of both batteries and UC is defined as hybrid energy storage system (HESS); it was adopted to reduce the current stress in the batteries decreasing size and costs and improving their lifetime. M. Masih-Tehrani *et al.* compared a traditional ESS (based on only batteries) with 2 HESSs: a UC based power distribution control strategy (PDCS) to use UC as prior ESS and a battery based PDCS to use battery as prior ESS. Two different bus driving cycle profiles were defined according to the collected data of two different cities, Tehran and Manhattan, as shown in ***Figure 81*** and ***Figure 82*****.**

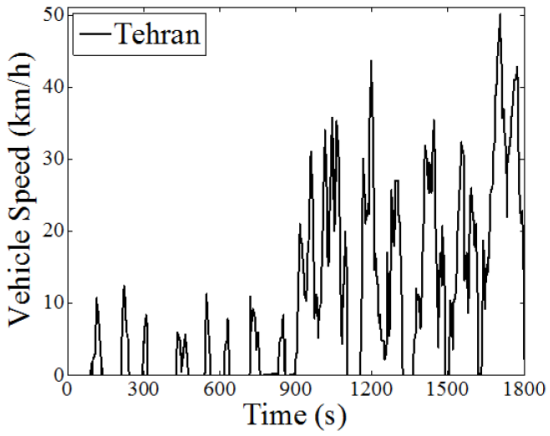

Figure 81 *Tehran city bus cycle. Adapted and reprinted with permission from [42].*

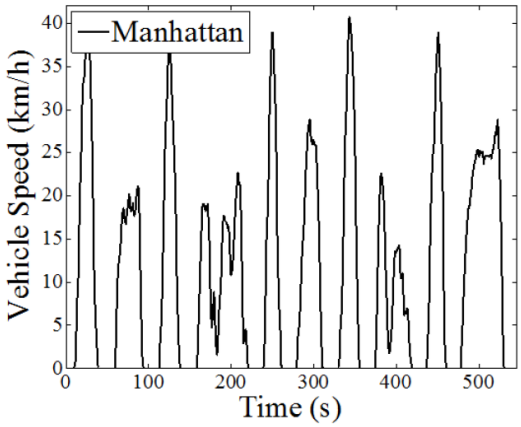

Figure 82 *Manhattan city bus cycle. Adapted and reprinted with permission from [42].*

The principal rule for UC based PDCS of HESS was that the power demand (P_dem) was firstly filled by the power of UC (P_UC) which was limited by the P_UC_min (minimum level of UC power) and P_UC_max (maximum level of UC power). The excess demand power (P_dem – P_UC) was generated by battery (P_bat). With the same idea but giving priority to the battery, the battery based PDCS of HESS was ruled as follows: P_dem was filled by P_bat which was limited by P_bat_min and P_bat_max1 (the maximum continuous of the battery power). The excess demand (P_dem – P_bat) was generated by P_UC. The remaining demand was finally filled by P_bat limited by P_bat_min and P_bat_max2 (instantaneous max power). 4 criteria were chosen to compare the performance of PDCS of ESS and HESSs: i) cycle count; ii) the sum of over-continuous current (Ah); iii) the sum of brake resistor power (kWh); iv) the sum of shortage power (kWh). Cycle count method was utilized to make an estimation of the number of charge/discharge cycles of batteries in real driving cycles. The sum of over-continuous current was an indicator of high current stress of battery which reduces its lifetime. The sum of brake resistor power indicated the energy saving loss. The sum of shortage power was the difference between the ESS power demand and the ESS power provided. A DoE was applied to optimize the parameters of the battery based PDCS. Results indicated that UC based HESS was the best configuration for Tehran driving cycle, while battery based HESS performed better for Manhattan driving cycle.

Battery management system (BMS) is the supervising control unit that processes the actual status of the battery cells sharing the data with the other controllers of the vehicle. To do this, a mathematical model describes the nonlinear dynamic behavior of the cell terminal voltage in dependance of charge/discharge current with the objective to predict the dynamics of the battery in the specific environmental and loads conditions. SoC is not directly measurable, so a series of modelling approaches exists: i) electro-chemical modelling; ii) equivalent circuit models; iii) black/grey box techniques-based modelling. Hametner *et al.* used the third approach to define a nonlinear model structure and automated nonlinear observer design [43]. DoE played a critical role in defining SoC excitation signal of the cell current. The signal was adjusted to the specific prior process model: in this way the model parameters could be estimated from measured data. The optimization was based on a linear dynamic cell model. Then the Fisher information matrix (FIM) was used: a tool to measure the information content of the excitation signal. The definition of the FIM was based on the partial derivative of the model output with respect to the model parameters. The following conditions were adopted to optimize the cell current excitation signal: i) SoC operating range was defined and included in experiment design; ii) Cell current excitation predefined levels were adopted; iii) Hysteresis and relaxation phases were applied which consisted in zero current phases between charge/discharge pulses.

Taguchi method in experimental procedures focused on corrosion process of positive current collector in lithium-ion batteries

The rise in global energy demand (expected to increase by 11–27% until 2050) due to socioeconomic development and climate warming emphasizes the urgency of addressing battery longevity. Corrosion, particularly affecting the aluminum current collector in the positive electrode, is a significant factor influencing the calendar life of batteries. The hydrolysis of lithium hexafluorophosphate ($LiPF_6$) produces compounds that deteriorate battery performance. The Taguchi method (TM) was employed to design experiments targeting the corrosion process in lithium-ion batteries (LIBs), aiming to extend their lifespan.

The scientific challenge involves controlling corrosion at the positive electrode current collector in LIBs to enhance their durability. TM was introduced by identifying process parameters, distinguishing between control and noise factors. Typically, at least two levels of each parameter are selected. Using a full-factorial design, a matrix of 3x3 resulted in 27 experiments, altering one factor at a time. The factors investigated were the type of lithium salt, concentration of ethylene carbonate (EC) in the electrolyte, and operating temperature.

TM involves calculating averages and standard deviations to determine the signal-to-noise ratio (SN ratio) and sensitivity to noise ratio (***Figure 83***). Objective functions are created based on optimization criteria, such as 'the smaller, the better' or 'the bigger, the better.' Analysis of variance (ANOVA) assesses the influence of control and noise parameters on the corrosion process. The study utilized three lithium salts, $LiPF_6$, $LiB(C_2O_4)_2$ (LiBOB), and $LiN(CF_3SO_3)_2$ (LiTFSI), and cyclic voltammetry and electrochemical impedance spectroscopy were performed at various temperatures.

Results indicated that corrosion was more pronounced in electrolytes containing $LiPF_6$, suggesting the composition of the electrolyte had a more significant impact than temperature on aluminum current collector behavior. An equivalent circuit model helped to analyze impedance data, showing variations in resistance with the progress of the experiment. The corrosion current densities were lowest with LiBOB and highest with LiTFSI, exhibiting temperature dependence. TM predictions aligned with experimental findings, suggesting TM's reliability in guiding electrochemical measurements.

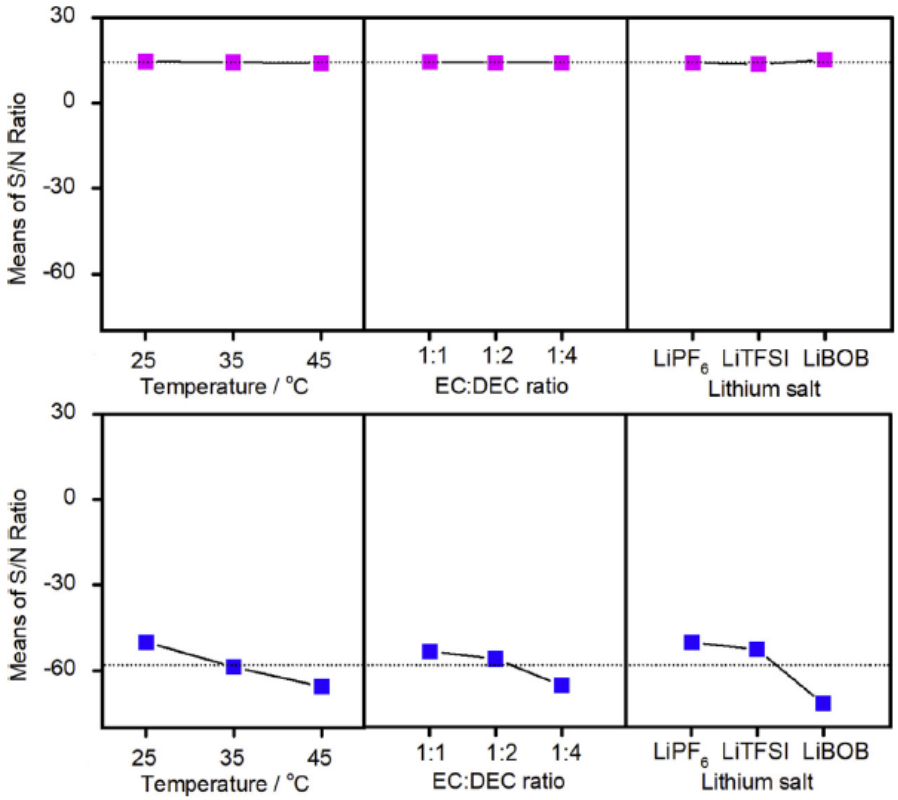

Figure 83 *Signal to noise ratio calculated with the Taguchi method for 'the larger the better' and 'the smaller the better' objective function. Adapted and reprinted with permission from [44].*

TM proved useful in assessing the relative impact of conditions on the corrosion process. The lithium salt type had the most significant influence, followed by temperature and the solvent mixture's composition. The study concludes that TM is valuable for predicting optimum conditions for testing lithium-ion batteries and determining the factors that most affect the corrosion process.

The effect of tab attachment positions and cell aspect ratio on temperature difference in large-format LIBs using design of experiments

Large format LIBs suffer from large temperature difference due to their large dimensions. This causes rapid reduction in cell capacity. Newman's model, which was the most used in last years, had the limitation of predicting the temperature distribution only in the thickness direction of the LIB cell. 3D electrochemical-thermal models were introduced to dimensionally extend the temperature distribution prediction. Lee *et al.* proposed a new approach based on DoE procedure and starting from the Rao and Newman's electrochemical-thermal model to analyze the temperature distribution of a 45-Ah LFP/graphite pouch cell [45]. The negative and positive tab attachment positions and cell aspect ratio were defined as design factors, while maximum and minimum temperatures in LIB cell and the difference between maximum and minimum temperature (T_{diff}) were identified as responses. The electrochemical model allowed for the calculation of the SOC, the potential distribution, the current density distribution, and the heat generation, while the thermal model was able to calculate the temperature distribution. Experimental results from the commercial LIB were compared with the model (***Figure 84***). Tests were performed using different discharge current I_t as follows: i) 1 I_t; ii) 2 I_t; iii) 3 I_t; iv) 4 I_t.

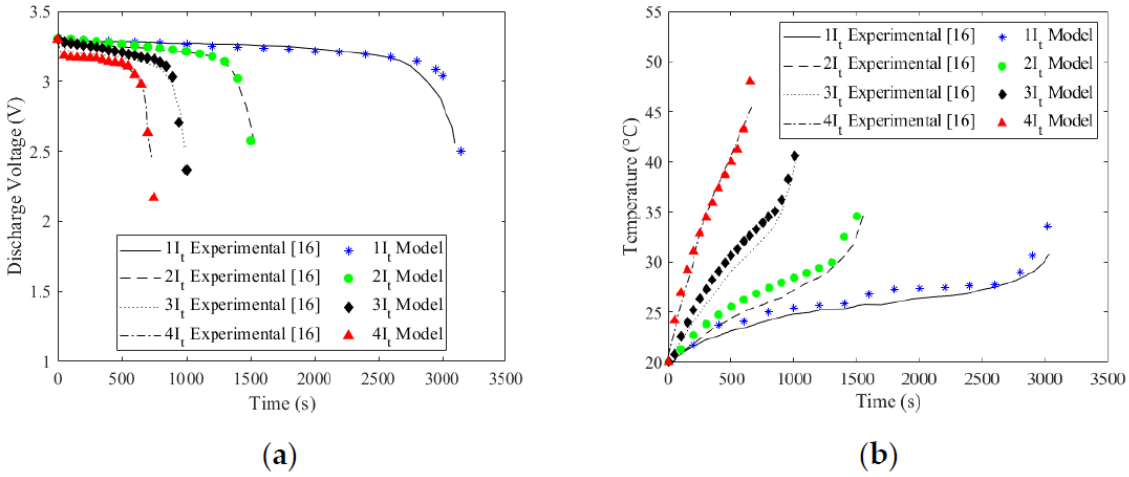

Figure 84 *Comparison of the experimental tests conducted on commercial 45-Ah LIB cell and the electrochemical-thermal model for different discharge current: (a) discharge voltage, (b) maximum temperature. Results demonstrated the reliability of the model in predicting the experimental results. Adapted and reprinted with permission from [45].*

The cell aspect ratio was defined as the ratio (*W*/*L*) of the width (*W*) to the length (*L*), while the tab attachment positions were defined as the ratio of the attached position to the attachable range (DR_n, DR_p) according to the following equations:

$$DR_t = \frac{Attached\ position}{Attachable\ range} \times 100, (t = n, p)$$

$$Attached\ position = d_t - 0.5W_t, (t = n, p)$$

$$Attachable\ range = 0.5W - W_t, (t = n, p)$$

A schematical description of the tab attachment positions is reported in ***Figure 85***.

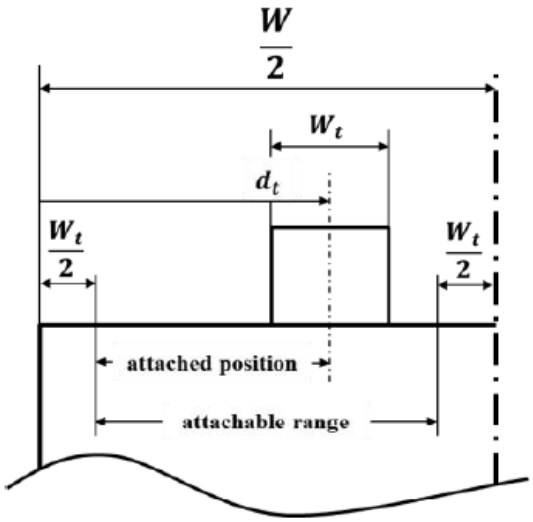

Figure 85 *Attached positions and attachable range for negative and positive tab attachments. Adapted and reprinted with permission from [45].*

The sampling points were defined performing a full factorial design (FFD) on three factors with five levels. The number of sampling points was obtained by applying the equation:

$$Total\ case = n^m, (n = number\ of\ levels, m = number\ of\ factors)$$

Consequently, cell aspect ratio levels were: i) 1/3; ii) 1/2; iii) 1; iv) 2; and v) 3, while tab attachment positions defined levels were: i) 0%; ii) 25%; iii) 50%; iv) 75%; and v) 100%.

ANOVA analysis was performed to determine if the design factors were statistically significant. The cell aspect ratio was assumed as the most effective followed by the positive tab attachment position.

The effects of cell aspect ratio and tab attachment positions (setting the other to 0%) on maximum temperature are reported in ***Figure 86***.

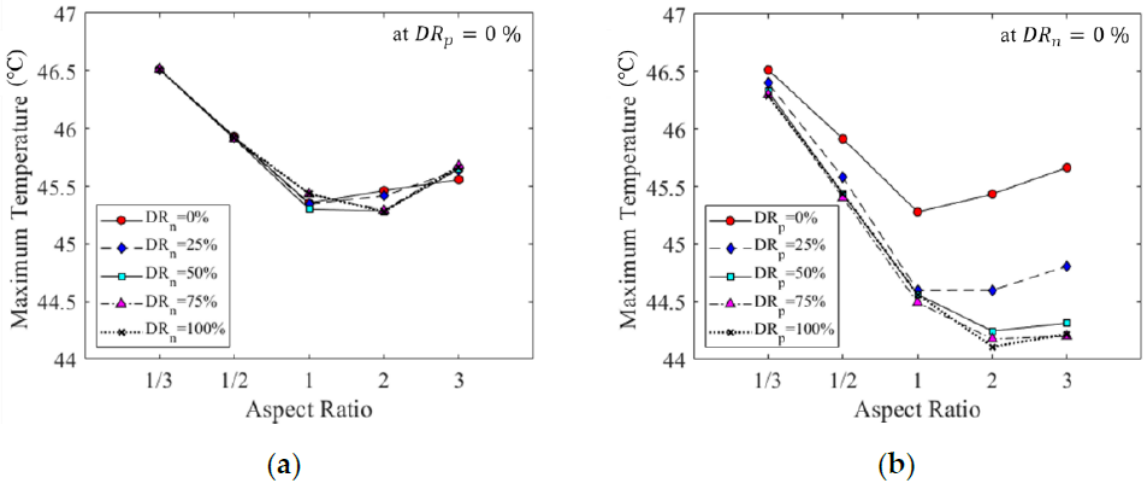

Figure 86 *Maximum temperature variation according to (a) aspect ratio and DR_n variation and (b) aspect ratio and DR_p variation. Longest current pathway set on the negative tab attachment which meant increased heat generation due to Joule effect generated by the increased internal resistance led to a variation of only 0.2 °C. This because the negative electrode tab was made of copper which has high electrical conductivity and heat capacity that mitigated the effect. In the opposite case, the variation of the positive tab attachment position led to a temperature variation over 1.9°C. Adapted and reprinted with permission from [45].*

The T_{diff} was strongly influenced by the cell aspect ratio. Moreover, the fact that the positive tab was made of aluminum led to an increase of its effect on T_{diff}.

Understanding the effect of coating-drying operating variables on electrode physical and electrochemical properties of lithium-ion batteries

Electrode manufacturing plays an important role in final LiBs' performance. There are many steps involved in this process, as described in ***Figure 87***, each stage is critical to the final result. Studies to understand and improve the techniques to carry out the electrode manufacturing involved theoretical analysis, production system simulations, uncertainty quantification and machine learning and of course, experimentations. The goal was to understand the causality between the electrode performance and the process variables. Romàm-Ramìrez *et al.* applied DoE methodology to a pilot scale manufacturing of NMC622 cathodes to study the main influencing process variables of the coating-drying step [46]. Process variables were identified as: i) comma bar gap; ii) web speed; iii) coating ratio; iv) drying temperature; v) air speed. Physical and chemical electrode properties were thickness, mass loading, porosity, gravimetric capacity, volumetric capacity and rate performance.

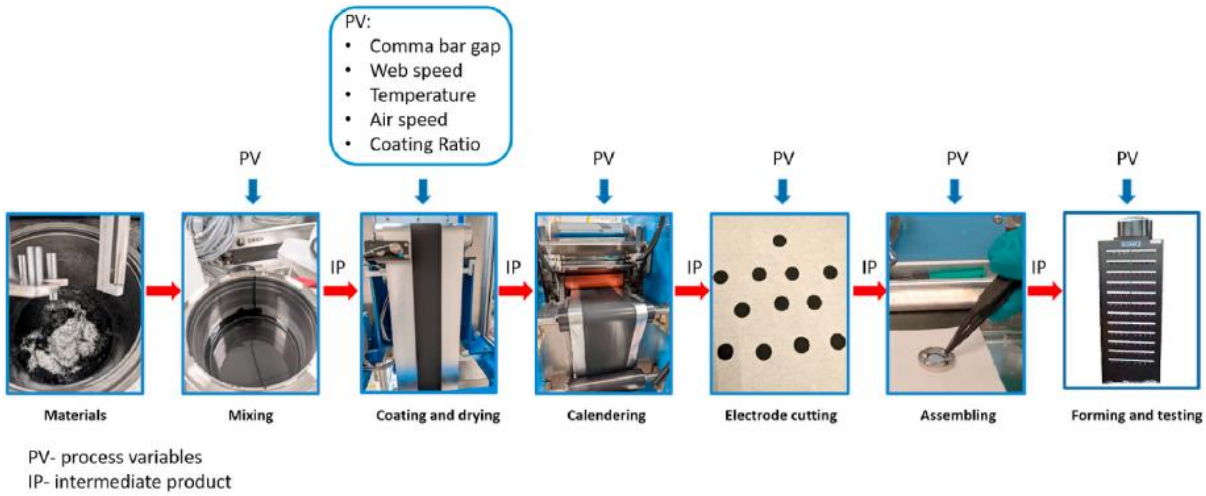

Figure 87 *Steps involved in the electrode manufacturing: mixing, coating, drying, calendering, cutting and final drying. Adapted and reprinted with permission from [46].*

Multiple linear regression analysis was performed using a Plackett-Burman (PB) experimental design. It consists in two-level fractional factorial design used for screening (study main effects). Dependent variables were measured at three different steps: before calendering, after final drying and on the coin cells produced from the strips. In ***Figure 88*** the main steps are represented. From ANOVA, coefficient of determination (R^2) and predicted R^2 (R^2_{pred}) were obtained to establish the predictive capabilities of the model.

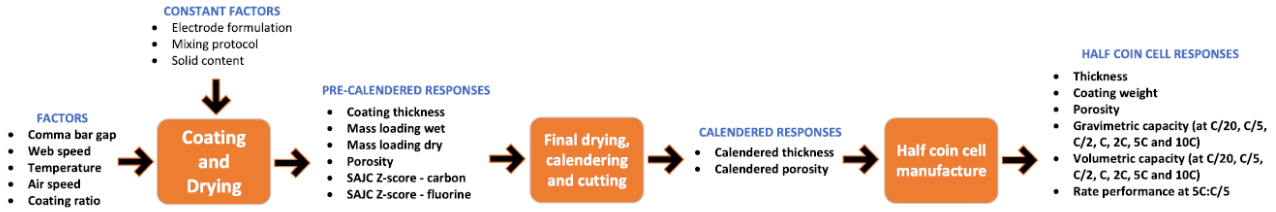

Figure 88 *Parameters diagram for the coating-drying process. 3-steps with a total of 26 responses were collected. Adapted and reprinted with permission from [46].*

The analysis comprised 12 experimental runs and it was divided into two parts: in the first one the study was focused on the influence of the main process variables on each response (main effects model). The second part was intended to determine the relationship between the electrochemical performance of the half coin cells and the physical characteristics. Bar gap and coating ratio were classified as the most influencing factors for the thickness, mass loadings and cell coating weight showing a closely link to battery performance. A regression analysis was also performed to determine possible relationship between electrochemical properties on half of coin cells and physical characteristics by taking into account coating weight and porosity as input variables. The results are reported in ***Figure 89***.

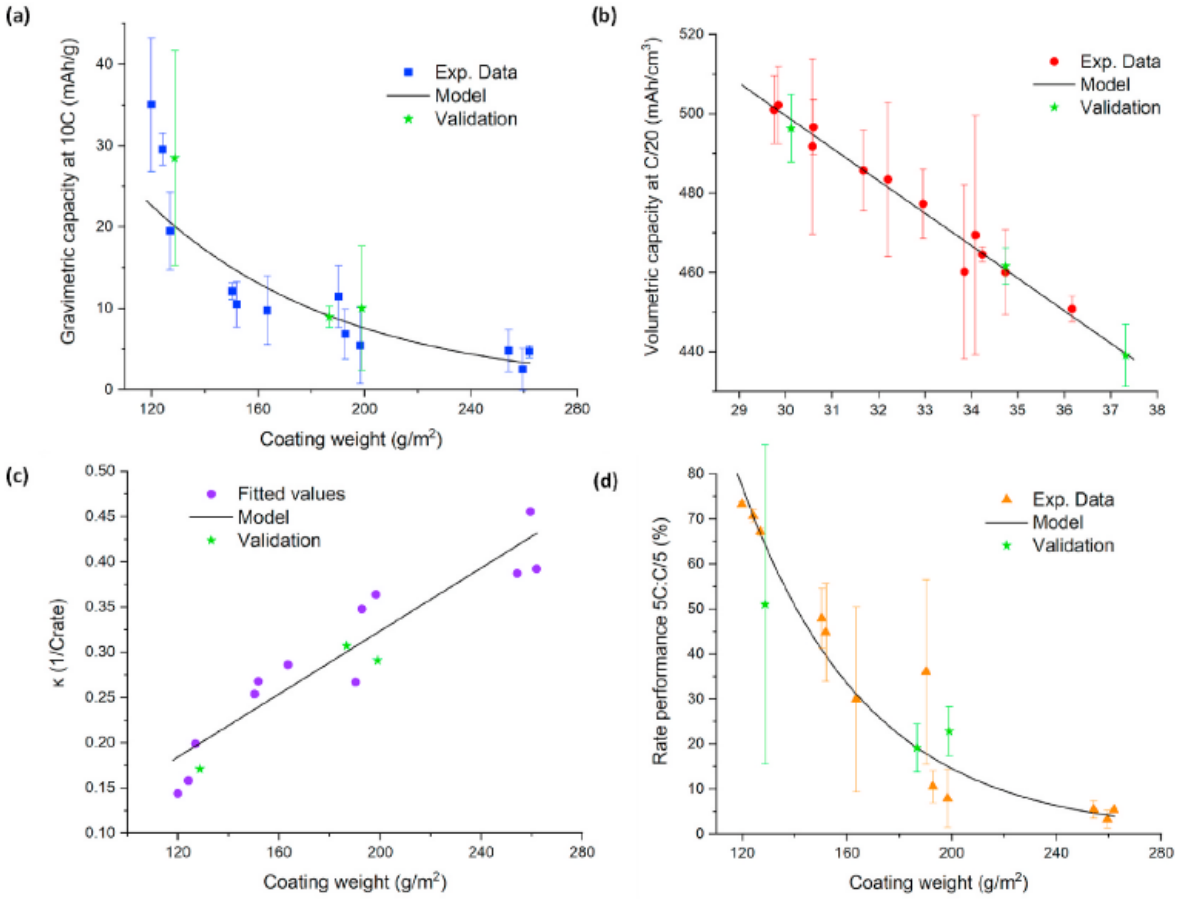

Figure 89 *Performance vs cell physical properties. (a) gravimetric capacity at 5C, (b) volumetric capacity at C/20, (c) rate capacity coefficient and (d) rate performance at 5C:C/5. Mass loading had the highest impact on volumetric energy density. Lower coating weights performed better thanks to improved electronic and ion transport. Adapted and reprinted with permission from [46].*

Coating weight was identified as the most important property. With thinner electrodes, superior performances were obtained. Porosity was critical only at the lower C-rates.

Unification of intensive and extensive properties of the passive cooling system under a single envelope for the thermal management of Li-ion batteries

The broad working temperature range for Li-ion batteries is -20 to 60 °C, while the optimum range is limited from 15 to 35 °C. Above the high limit the cells are subjected to capacity degradation, while at lower temperatures they are affected by an increase of the internal resistance. Active and passive cooling techniques were studied in this regard. In the case of electric vehicles, the use of a passive cooling system is considered to reduce power consumption. Phase change materials (PCMs) were used in this system since they can absorb the excess heat generated during charge/discharge cycles. From another point of view PCMs are limited by their low thermal conductivity. So, additional dissipation media as fins and heat pipes are coupled as secondary heat sinks. Verma *et al.* developed a model where PCM layers were inserted in between the cells of a battery module coupled with an array of longitudinal fins. First of all, a CFD study was conducted to estimate the combined effects of PCM and fins. Then, a DoE was carried out with the use of non-dimensional retrofit characteristics as follows:

Mass ratio $MR = \frac{mass_{PCM} + mass_{Fin}}{mass_{battery\ pack}}$: ratio of the mass of retrofit to the mass of battery pack;

Length ratio $LR = \frac{Length\ of\ Fin}{Thickness\ of\ PCM}$: ratio of the fin length (mm) and PCM thickness (mm);

Thermal diffusivity $DR = \frac{\alpha_{Fin}}{\alpha_{PCM-modified}}$: ratio of the fin diffusivity and the modified PCM diffusivity according to the following formulas:

$\alpha_{PCM-modified} = \frac{k_{PCM}}{\rho\frac{L}{\Delta T}}$ and

$\alpha_{Fin} = \frac{k_{Fin}}{\rho C_p}$;

with k the thermal conductivity (W/mK), ρ the density (kg/m^3), L the latent heat (J/kg) and ΔT the temperature range of the PCM ($T_{liquidus}$-$T_{solidus}$). DoE development is represented in ***Figure 90***. The thermal performance was defined by evaluating five parameters: i) volume average temperature of the four cells constituting the battery pack after 1200 s; ii) active time as the time after which the PCM has to be solidified for the next discharge cycle; iii) temperature uniformity as variation between the maximum and minimum temperature; iv) heat duty as the ratio of heat flux to a body's surface and the body's mass that absorbs the incoming heat; v) non-dimensional temperature drop as the ratio of actual and maximum temperature difference in the battery pack as follows:

$non - dimensional\ temperature\ drop = \frac{\Delta T_{actual}}{\Delta T_{max}}$

with:

$\Delta T_{actual} = T_{max,without\ BTMS} - T_{volume-average}$

$\Delta T_{max} = T_{max,without\ BTMS} - T_{ambient}$

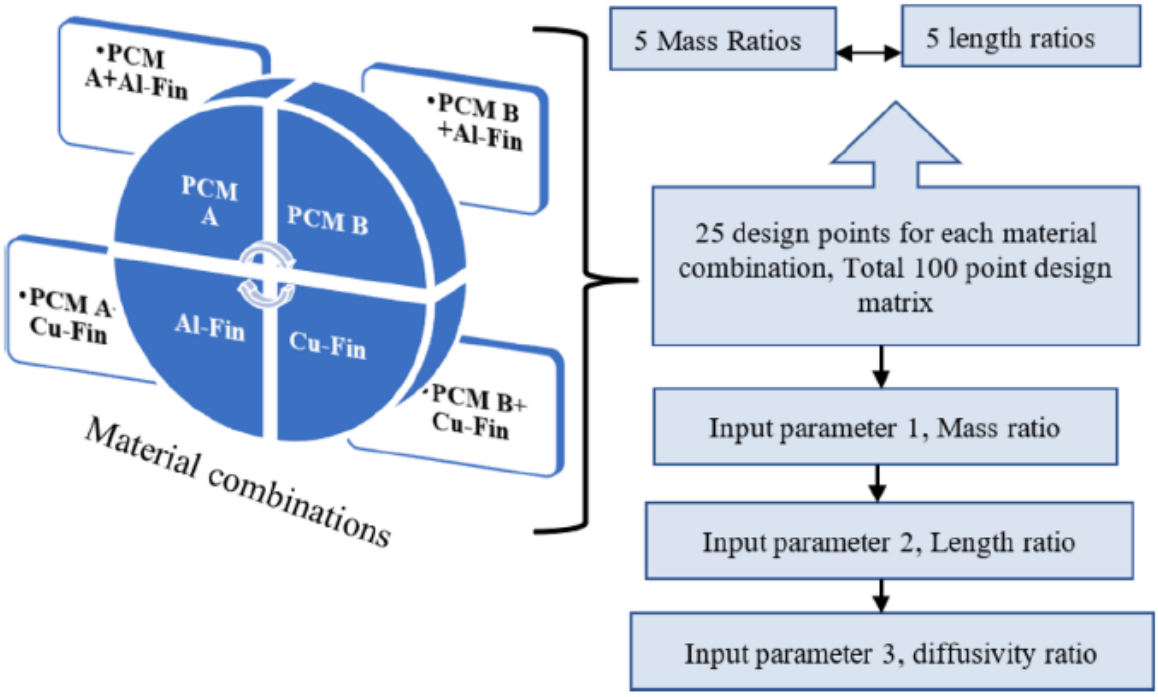

Figure 90 *DoE development. Different materials for PCM and fins were considered for a total of four combinations. For each combination, 25 design points were identified. Adapted and reprinted with permission from [47].*

In order to make more intelligible the results of the study, which was based on three non-dimensional inputs, a composite index was defined as follows to condense all the inputs into one:

$$VSR = \frac{0.95\left(\frac{1}{LR} + MR\right)^{0.55} - 1.08\{\log_{10}(DR) - 4\}^{1.74}}{1.1MR + \frac{1.12}{LR}e^{\{\log_{10}(DR)-4\}^{1.74}}}$$

From the analysis of the obtained results, it was found that not only the best combination of MR and LR but also the combined choice of the optimized material with optimized MR and LR led to a holistic thermal management system.

Chapter 3: Discussion

Section 3.1: Syntesis of findings

The comprehensive literature review presented in Chapter 2 has highlighted the multifaceted applications of Design of Experiments (DoE) in the development and improvement of electrical batteries. By systematically categorizing the reviewed articles into four main sections—Recycling and Recovery of Battery Materials, Battery Performance and Aging, Synthesis and Material Optimization, and Battery Safety and Management—we can draw several key insights.

3.1.1 Recycling and Recovery of Battery Materials

DoE is instrumental in optimizing processes for the recycling and recovery of battery materials. Several studies (e.g., the work on zinc and brass recovery through corona-electrostatic technology) have demonstrated how DoE can enhance the efficiency of material separation and recovery. These findings are significant as they suggest that DoE can contribute to more sustainable battery lifecycle management by improving the recovery rates of critical materials from spent batteries. Additionally, bioleaching methods optimized through DoE have shown potential in reducing the environmental impact of battery disposal.

3.1.2 Battery Performance and Aging

Research in this area underscores the effectiveness of DoE in investigating and mitigating factors that influence battery performance and aging. Studies utilizing DoE to assess the impact of variables such as charge/discharge rates, temperature, and electrode composition have provided valuable data that can lead to the development of longer-lasting batteries. For instance, experiments designed to optimize pulse charging algorithms have yielded improved battery performance, demonstrating that DoE can significantly enhance the operational efficiency of lithium-ion batteries. Furthermore, the aging models calibrated using DoE techniques have been crucial in predicting battery lifespan and performance degradation, offering pathways to more durable battery designs.

3.1.3 Synthesis and Material Optimization

In the context of synthesis and material optimization, DoE has been pivotal in fine-tuning the properties of battery components. Studies on the synthesis of ultra-fine copper particles and the optimization of lithiated metal phosphates have shown that DoE can lead to materials with superior energy densities and better overall performance. The ability of DoE to systematically explore and identify optimal synthesis conditions ensures that battery materials can be produced with the desired properties, thereby improving the efficiency and capacity of batteries. This section of the literature highlights the potential of DoE to accelerate the development of advanced materials that meet the stringent requirements of modern battery applications.

3.1.4 Battery Safety and Management

Safety and thermal management are critical concerns in battery technology, and the reviewed literature suggests that DoE is a valuable tool in addressing these issues. Experiments designed to optimize cooling strategies and investigate the thermal behavior of batteries have provided insights into preventing thermal runaway and other safety hazards. For example, studies on battery pack temperature estimation and the optimization of cell attachment positions have shown how DoE can be used to enhance the safety and reliability of battery systems. These findings are particularly relevant for applications in electric vehicles, where battery safety is paramount.

3.2: Future Research Directions

The synthesis of findings highlights the substantial advancements that DoE has contributed to various aspects of electrical battery research. Despite these advancements, there are several promising avenues for future research that can further enhance the development, optimization, and safety of battery technologies. Future research should aim at developing more advanced and sustainable recycling techniques for battery materials. While current DoE methodologies have optimized processes such as bioleaching and corona-electrostatic separation, there is a need to explore more eco-friendly and cost-effective methods. Integrating machine learning with DoE can lead to the discovery of new, optimized parameters for recycling processes that minimize environmental impact and maximize material recovery efficiency. Ongoing research should continue to explore how DoE can be applied to improve battery performance and extend lifespan. There is increasing interest in examining the effects of nano-materials and advanced electrode designs on battery efficiency. DoE can systematically test and optimize these new materials and designs, providing a clearer understanding of the factors that most significantly impact performance and longevity. Additionally, real-time monitoring and adaptive control systems, guided by DoE principles, can be developed to dynamically adjust operating conditions for optimal performance. Future studies should broaden the scope of material optimization through DoE by investigating a wider range of materials and synthesis techniques. The development of high-capacity and high-stability materials, such as silicon-based anodes or solid-state electrolytes, can benefit from DoE to identify optimal synthesis conditions. Moreover, combining DoE with high-throughput experimentation can accelerate the discovery of novel materials with superior properties. Ensuring the safety and reliability of batteries remains a critical area of research. Future efforts should focus on enhancing thermal management strategies and developing safer battery chemistries. DoE can play a crucial role in optimizing cooling systems and thermal interface materials to prevent overheating and thermal runaway. Additionally, research should explore the use of non-flammable electrolytes and the integration of smart sensors for early detection of safety issues. By leveraging DoE, these studies can systematically identify the most effective safety measures and design parameters. As the field of electrical batteries evolves, there is a significant opportunity to integrate DoE with emerging technologies such as artificial intelligence (AI) and the Internet of Things (IoT). AI-driven DoE can facilitate more sophisticated and efficient optimization processes by predicting outcomes and suggesting optimal experimental designs. IoT-enabled batteries can provide continuous data streams that inform DoE-based adjustments in real-time, enhancing performance and reliability.

Chapter 4: Conclusion

4.1: Final thoughts

This thesis has explored the multifaceted applications of Design of Experiments (DoE) in the field of electrical batteries, drawing insights from a comprehensive literature review. By enabling systematic and efficient experimentation, DoE has addressed numerous challenges in battery technology, from material recovery and performance optimization to safety and reliability. In conclusion, the application of DoE has not only provided significant insights and improvements in current battery technologies but also laid a strong foundation for future innovations. As the demand for efficient, sustainable, and safe energy storage solutions continues to grow, the methodologies and findings presented in this thesis will be instrumental in guiding ongoing and future research in the field of electrical batteries.

List of figures

Riferimenti

[1] L. Romàn-Ramírez e J. Marco, «Design of experiments applied to lithium-ion batteries: A literature review,» *Applied energy,* vol. 320, n. 119305, 2022.

[2] L. Calin, A. Catinean,, M. Bilici and A. Samuila, "A corona-electrostatic technology for zinc and brass recovery from the coarse fraction of the recycling process of spent alkaline and zinc-carbon batteries," *Journal of Cleaner Production,* no. 278, 2021.

[3] L. W. Juang, P. J. Kollmeyer, A. E. Anders, T. M. Jahns, R. D. Lorenz and D. Gao, "Investigation of the influence of superimposed AC current on lithium-ion battery aging using statistical design of experiments," *Journal of Energy Storage,* no. 11, p. 93–103, 2017.

[4] M. I. Bajestani, S. Mousavi and S. Shojaosadati, "Bioleaching of heavy metals from spent household batteries using Acidithiobacillus ferrooxidans: Statistical evaluation and optimization," *Separation and Purification Technology,* no. 132, 2014.

[5] A. Wolf, A. Flegler, J. Prieschl, T. Stuebinger, W. Witt, F. Seiser, T. Vinnay, T. Sinn, G. Marco, H. Nirschl e K. Mandel, «Centrifugation based separation of lithium iron phosphate (LFP) and carbon black for lithium-ion battery recycling,» *Chemical Engineering & Processing: Process Intensification,* vol. 160, 2021.

[6] Y. J. Jung, B. Y. Yoo, S. C. Park e S. H. Son, «Design optimization of selective lithium leaching of cathodic active materials from spent lithium-ion batteries based on the Taguchi method,» *Metals,* vol. 108, p. 11, 2021.

[7] A. Porvali, A. Chernyaev, S. Shukla e M. Lundström, «Lithium ion battery active material dissolution kinetics in Fe(II)/Fe(III) catalyzed Cu-H2SO4 leaching system,» *Separation and Purification Technology,* vol. 236, n. 116305, 2020.

[8] M. Kahl, S. Pavón e M. Bertau, «Recycling of Primary Lithium Batteries Production Residues,» *ChemPhysChem,* n. 22, p. 577 –584, 2021.

[9] S. Pavón, D. Kaiser, R. Mende e M. Bertau, «The COOL-Process—A Selective Approach for Recycling Lithium Batteries,» *Metals,* vol. 11, n. 2, p. 259, 2021.

[10] K. Chabhadiya, R. R. Srivastava e P. Pathak, «Two-step leaching process and kinetics for an eco-friendly recycling of critical metals from spent Li-ion batteries,» *Journal of Environmental Chemical Engineering,* vol. 9, n. 3, 2021.

[11] X. Liu, X. Deng, Y. He, X. Zheng e G. Zeng, «A Dynamic State-of-Charge Estimation Method for Electric Vehicle Lithium-Ion Batteries,» *enegies,* vol. 121, p. 13, 2020.

[12] J. Unger, C. Hametner, S. Jakubek e M. Quasthoff, «A novel methodology for non-linear system identification of battery cells used in non-road hybrid electric vehicles,» *Journal of Power Sources,* vol. 269, pp. 883-897, 2014.

[13] A. Cordoba-Arenas, S. Onori, Y. Guezennec e G. Rizzoni, «Capacity and power fade cycle-life model for plug-in hybrid electric vehicle lithium-ion battery cells containing blended spinel and layered-oxide positive electrodes,» *Journal of Power Sources,* vol. 278, pp. 473 - 483, 2015.

[14] W. Prochazka, G. Pregartner e M. Cifrain, «Design-of-Experiment and Statistical Modeling of a Large Scale Aging Experiment for Two Popular Lithium Ion Cell Chemistries,» *Journal of The Electrochemical Society,* vol. 160, p. 12, 2013.

[15] R. Mathieu, I. Baghdadi, O. Briat e P. Gyan, «D-optimal design of experiments applied to lithium battery for ageing model calibration,» *Energy,* vol. 141, pp. 2108-2119, 2017.

[16] P. Gyan, P. Aubret, J. Hafsaoui, F. Sellier e S. Bourlot, «Experimental Assessment of Battery Cycle Life Within the SIMSTOCK Research Program,» *Oil and Gas Science and Technology, Institut Francais du Petrole,* vol. 68, pp. 137-147, 2013.

[17] S. Nahidi, M. Salari, I. J. Gavzan e S. Saedodin, «Experimental investigation of the effect of C-rate, electrode gaps, and electrode surface roughness on the performance characterization of lead-acid batteries,» *International Journal of Energy Research,* pp. 1-12, 2020.

[18] J. Stadler, C. Krupp, M. Ecker, J. Bandlow, B. Spier e A. Latz, «Investigation and modeling of cyclic aging using a design of experiment with automotive grade lithium-ion cells,» *Journal of Power Sources,* vol. 521, p. 230952, 2022.

[19] I. Baghdadi, R. Mathieu, O. Briat, P. Gyan e J.-M. Vinassa, «Lithium-ion battery ageing assessment based on a reduced design of experiments,» Univ. Bordeaux, CNRS, Bordeaux INP; Renault, Technocentre de Guyancourt.

[20] A. Singh, A. Izadian e S. Anwar, «Model based condition monitoring in lithium-ion batteries,» *Journal of Power Sources,* vol. 268, pp. 459 - 468, 2014.

[21] J. Guo, Z. Li, T. Keyser e Y. Deng, «Modeling Li-Ion Battery Capacity Fade Using Designed Experiments,» in *Industrial and Systems Engineering Research Conference*, 2014.

[22] T. T. Vo, X. Chen, W. Shen e A. Kapoor, «New charging strategy for lithium-ion batteries based on the integration of Taguchi method and state of charge estimation,» *Journal of Power Sources,* vol. 273, p. 413e422, 2015.

[23] J. Remmlinger, M. Buchholz, M. Meiler, P. Bernreuter e K. Dietmayer, «State-of-health monitoring of lithium-ion batteries in electric vehicles by on-board internal resistance estimation,» *Journal of Power Sources,* vol. 196, p. 5357–5363, 2011.

[24] T. J. Kim, B. D. Youn e H. J. Kim, «Battery Pack Temperature Estimation Model for EVs and,» *CHEMICAL ENGINEERING TRANSACTIONS,* n. 33, 2013.

[25] S. Martinet, C. Bourbon, M. Amuntencei, D. Peralta, L. Simonin, M. Rey-Chapuis e S. Patoux, «Application of the methodology of Design Of Experiments to the development of Li-Ion battery active materials,» *224th ECS Meeting, © 2013 The Electrochemical Society,* n. 899, 2013.

[26] F. Bella, A. B. Muñoz-García, F. Colò, G. Meligrana, A. Lamberti, M. Destro, M. Pavone e C. Gerbaldi, «Combined structural, chemometric, and electrochemical investigation of vertically aligned TiO2 nanotubes for Na-ion batteries,» *ACS Omega,* vol. 3, pp. 8440-8450, 2018.

[27] S. Martinet, C. Bourbon, M. Amuntencei, C. Chabrol, D. Tomasi, M. Rey e S. Patoux, «Design of experiment methodology to improve the energy density of lithiated metal phosphates,» *Solid State Ionics,* vol. 268, pp. 247-251, 2014.

[28] J. H. Teo, F. Strauss, Đ. Tripković, S. Schweidler, Y. Ma, M. Bianchini, J. Janek e T. Brezesinski,, «Design-of-experiments-guided optimization of slurry-cast cathodes for solid-state batteries,» *Cell Reports Physical Science,* vol. 2, n. 6, 2021.

[29] O. Rynne, M. Dubarry, C. Molson, D. Lepage, A. Prébé, D. Aymé-Perrot, D. Rochefort e M. Dollé, «Designs of Experiments for Beginners—A Quick Start Guide for Application to Electrode Formulation,» *batteries,* vol. 72, 2019.

[30] Y. Kerdja, M. Chandesris e S. Martinet, «Microscopy imaging based numerical model of Li-ion batteries electrode: a parametric study through a design of experiment approach,» *Journal of Power Sources,* vol. 507, 2021.

[31] J. Kim, D. Lee, J. Lee e C. Kim, «Optimization for maximum specific energy density of a lithium-ion battery using progressive quadratic response surface method and design of experiments,» *Scientific Reports,* vol. 10, n. 15586, 2020.

[32] L. Li, T. Yang e Z. Li, «Parameter optimization and yield prediction of cathode coating separation process for direct recycling of end-of-life lithium-ion batteries,» *RSC Adv.,* n. 11, 2021.

[33] A. Awarke, S. Lauer, S. Pischinger e M. Wittler, «Percolation–tunneling modeling for the study of the electric conductivity in LiFePO4 based Li-ion battery cathodes,» *Journal of Power Sources,* vol. 196, pp. 405-411, 2011.

[34] R. K. Nekouei, F. Rashchi e A. A. Amadeh, «Using design of experiments in synthesis of ultra-fine copper particles by electrolysis,» *Powder Technology,* n. 237, p. 165–171, 2013.

[35] O. Delbeke, H. Laget, S. Hollevoet, L. Vandevelde e J. Mertens, «A comprehensive and time efficient characterization of redox flow batteries through Design of Experiments,» *Journal of Energy Storage,* vol. 50, 2022.

[36] Y. Lu, M. Maftouni, T. Yang, P. Zheng, D. Young, Z. J. Kong e Z. Li, «A novel disassembly process of end-of-life lithium-ion batteries enhanced by online sensing and machine learning techniques,» *Journal of Intelligent Manufacturing,* vol. 34, p. 2463–2475, 2023.

[37] H. Sun e R. Dixon, «Development of cooling strategy for an air cooled lithium-ion batterypack,» *Journal of Power Sources,* vol. 272, pp. 404-414, 2014.

[38] A. P. Schmidt, M. Bitzer, Á. W. Imre e L. Guzzella, «Experiment-driven electrochemical modeling and

systematic parameterization for a lithium-ion battery cell,» *Journal of Power Sources,* vol. 195, p. 5071–5080, 2010.

[39] J. M. Amanor-Boadu e A. Guiseppi-Elie, «Improved performance of Li-ion Polymer batteries through improved pulse charging algorithm,» *applied sciences,* p. 10, 2020.

[40] Y. Xie, H. Guo, W. Li, Y. Zhang, B. Chen e K. , «Improving battery thermal behavior and consistency by optimizing structure and working parameter,» *Applied Thermal Engineering,* vol. 196, 2021.

[41] B. Stumper, J. Dhom, L. Schlosser, D. Schreiner, A. Mayr e R. Daub, «Modeling of the Lithium Calendering Process for Direct Contact Prelithiation of Lithium-Ion Batteries,» *Procedia CIRP,* vol. 107, p. 984–990, 2022.

[42] M. M. Tehrani, M. Hairi-Yazdi e V. Esfahanian, «Power Distribution Development and Optimization of Hybrid Energy Storage System,» *International Journal of Automotive Engineering,* vol. 4, n. 2, pp. 675 - 684, 2014.

[43] C. Hametner e S. Jakubek, «State of charge estimation for Lithium Ion cells: Design of experiments, nonlinear identification and fuzzy observer design,» *Journal of Power Sources,* vol. 238, pp. 413 - 421, 2013.

[44] A. Gabryelczyk, S. Ivanov, A. Bund e G. Lota, «Taguchi method in experimental procedures focused on corrosion process of positive current collector in lithium-ion batteries,» *Electrochimica Acta,* vol. 360, 2020.

[45] J.-J. Lee, J.-S. Kim, H.-K. Chang, D.-C. Lee e C.-W. Kim, «The effect of tab attachment positions and cell aspect ratio on temperature difference in large-format LIBs using Design of Experiments,» *Energies,* vol. 14, n. 116, 2021.

[46] L. Rom´an-Ramírez, G. Apachitei, M. Faraji-Niri, M. Lain, W. Widanage e J. Marco, «Understanding the effect of coating-drying operating variables on electrode physical and electrochemical properties of lithium-ion batteries,» *Journal of Power Sources,* vol. 516, 2021.

[47] A. Verma, P. Saikia e D. Rakshit, «Unification of intensive and extensive properties of the passive cooling system under a single envelope for the thermal management of Li-ion batteries,» *Journal of Energy Storage,* vol. 50, p. 23, 2022.